DOKUZ EYLÜL UNIVERSITY

GRADUATE SCHOOL OF NATURAL AND APPLIED SCIENCES

MODELING AND PASSIVE VIBRATION CONTROL OF SINGLE-LINK FLEXIBLE MANIPULATORS WITH SYSTEM IDENTIFICATION METHODS

by

Şefika İpek LÖK

July, 2023

İZMİR

MODELING AND PASSIVE VIBRATION CONTROL OF SINGLE-LINK FLEXIBLE MANIPULATORS WITH SYSTEM IDENTIFICATION METHODS

A Thesis Submitted to the
Graduate School of Natural And Applied Sciences of Dokuz Eylül University
In Partial Fulfillment of the Requirements for the Degree of Doctor of Philosophy in Department of Mechatronic Engineering

by

Şefika İpek LÖK

July, 2023
İZMİR

Ph.D. THESIS EXAMINATION RESULT FORM

We have read the thesis entitled "**MODELING AND PASSIVE VIBRATION CONTROL OF SINGLE-LINK FLEXIBLE MANIPULATORS WITH SYSTEM IDENTIFICATION METHODS**" completed by **ŞEFİKA İPEK LÖK** under supervision of **PROF. DR. LEVENT MALGACA** and we certify that in our opinion it is fully adequate, in scope and in quality, as a thesis for the degree of Doctor of Philosophy.

.....

Prof. Dr. Levent MALGACA

Supervisor

.....	.....
Prof. Dr. Levent ÇETİN	Assoc. Prof. Dr. Hatice DOĞAN
Thesis Committee Member	Thesis Committee Member
.....	.....
Prof. Dr. İsa YEŞİLYURT	Assoc. Prof. Dr. S. Murat BAĞDATLI
Examining Committee Member	Examining Committee Member

Prof. Dr. Okan FISTIKOĞLU
Director
Graduate School of Natural and Applied Sciences

ACKNOWLEDGEMENTS

I would like to thank my supervisor Prof. Dr. Levent MALGACA for his very valuable support, and critical suggestions throughout the Ph.D. thesis. It was a great privilege and honor to study under his guidance. I would like to thank Prof. Dr. Saide SARIGÜL, Prof. Dr. Levent ÇETİN, Assoc. Prof. Dr. Hatice DOĞAN for their valuable comments throughout the thesis progress meetings.

This thesis was supported by Dokuz Eylül University Scientific Research Projects (DEUBAP) with the project number 2019.KB.FEN.023.

I would like to thank Prof. Dr. Carmine Maria PAPPALARDO from University of Salerno in Italy, for his valuable contributions and guidance during this thesis.

This thesis was supported by the Research Foundation of The Scientific and Technological Research Council of Türkiye (TUBITAK) 2214-A program with the project number 1059B141900658. I would like to thank my project directors Prof. Dr. Zi-Qiang LANG and Prof. Dr. Lyudmila MIHAYLOVA from the University of Sheffield in the UK for their valuable guidance, and critical suggestions.

I would like to thank Dr. Özge CANLI USTA, Seda VATAN CAN, Gizem KALENDER, Kübra KARADAĞ, Dr. Salih DEMİRTAŞ, Dr. Mehmet UYAR whose support as part of my Ph.D. I would like to thank my parents Mesut ŞAMLI and Yasemin ŞAMLI, my brother Ziya ŞAMLI, and my daughter Defne Ela LÖK for their love, encouragement, and support of my decisions.

Finally, I would like to thank my dear husband, Ömer LÖK for his understanding, patience, endless love, and encouragement throughout my Ph.D. thesis. I am grateful to have him in my life.

Şefika İpek LÖK

MODELING AND PASSIVE VIBRATION CONTROL OF SINGLE-LINK FLEXIBLE MANIPULATORS WITH SYSTEM IDENTIFICATION METHODS

ABSTRACT

In this thesis, the identification and passive vibration control of single-link manipulators are studied using System Identification (SI) approaches. SI method is utilized for the modeling of manipulators made of steel and composite materials using numerical and experimental signals. Firstly, modeling of a four-degree-of-freedom (dof) mechanical system is studied using the SI method. Then, to model the manipulators, the finite element (FE) model of the steel manipulator (SM) is created in ANSYS/APDL, and an experimental system is set up to synchronously drive the manipulator and measure the acceleration, displacement, and strain signals of the manipulator. The transfer functions of the SM are identified with AutoRegressive eXogenous (ARX), Continuous-Time System Identification (CTSI), the State-Space ESTimation (SSEST), and Numerical Algorithms for Subspace State-Space System Identification (N4SID) methods using simulation and experimental signals. The effect of the SI methods on modeling is investigated for various payloads and output types. Also, the modeling of the composite manipulators is studied with experimental signals. S-curve motion input and optimization with Genetic Algorithm (GA) are studied to reduce the unwanted residual vibration of the manipulators. A five-segment S-curve motion input is designed excluding linear acceleration and deceleration segments of an ideal S-curve with seven-segments. Time parameters of the S-curve are selected based on the first natural frequency of the manipulator. Also, time parameters of a velocity profile are optimized with the GA using the identified transfer functions of the manipulator. A comparative analysis of modeling and passive vibration control of the manipulators is presented.

Keywords: Flexible manipulator, system identification, passive vibration control, S-curve motion input, Genetic Algorithm

SİSTEM TANIMLAMA YÖNTEMLERİ İLE TEK EKSENLİ ESNEK MANİPÜLATÖRLERİN MODELLENMESİ VE PASİF TİTREŞİM KONTROLÜ

ÖZ

Bu tezde, tek eksenli manipülatörlerin modellemesi ve pasif titreşim kontrolü sistem tanımlama (SI) yaklaşımları kullanarak çalışılmıştır. Çelik ve kompozit materyallerden yapılan manipülatörlerin nümerik ve deneysel sinyallerini kullanarak modellenmesi için SI yöntemi kullanılmıştır. İlk olarak dört serbestlik dereceli (dof) mekanik bir sisteminin modellenmesi SI yöntemi kullanarak kullanılmıştır. Sonrasında manipülatörleri modellemek için, çelik manipülatörün (SM) sonlu elemanlar modeli ANSYS/APDL'de oluşturulmuş ve senkron olarak manipülatörü sürmek ve manipülatörün ivme, yer değişimi ve gerinim sinyallerini ölçmek için deneysel bir sistem kurulmuştur. SM'nin transfer fonksiyonları simülasyon ve deneysel sinyaller kullanılarak AutoRegressive eXogenous (ARX), Continuous-Time System Identification (CTSI), the State-Space ESTimation (SSEST) ve Numerical Algorithms for Subspace State-Space System Identification (N4SID) yöntemleri ile tanımlanmıştır. SI yöntemlerinin modelleme üzerindeki etkisi farklı yükler ve çıktı tipleri için araştırılmıştır. Ayrıca deneysel sinyaller ile kompozit manipülatörlerin modellemesi çalışılmıştır. Manipülatörlerin istenmeyen artık titreşimlerini azaltmak için S-curve hareket girdisi ve Genetik Algoritma (GA) ile optimizasyon çalışılmıştır. İdeal bir 7 bölümlü S-curve hareket girdisinin lineer hızlanma ve yavaşlama bölümleri hariç tutarak beş bölümlü bir S-curve hareket girdisi dizayn edilmiştir. S-curve'ün zaman parametreleri manipülatörün ilk doğal frekansına göre seçilmiştir. Ayrıca, manipülatörün tanımlanmış transfer fonksiyonları kullanarak bir hız profilinin zaman parametreleri optimize edilmiştir. Manipülatörün modellenmesi ve pasif titreşim kontrolünün karşılaştırmalı bir analizi sunulmuştur.

Anahtar kelimeler: Esnek manipülatör, sistem tanımlama, pasif titreşim kontrolü, S-curve hareket girdisi, Genetik Algoritma

CONTENTS

Page

Ph.D. THESIS EXAMINATION RESULT FORM ii
ACKNOWLEDGEMENTS iii
ABSTRACT iv
ÖZ v
LIST OF FIGURES xi
LIST OF TABLES xii
LIST OF SYMBOLS xiii
ABBREVIATIONS xiv

CHAPTER ONE – INTRODUCTION 1

1.1 Introduction 1
1.1.1 Literature Review on Modeling with System Identification Method 1
1.1.2 Literature Review on Vibration Control 5
1.2 Scope, Contributions and Orginality of the Thesis 7
1.3 Organization of the Thesis 8

CHAPTER TWO – SYSTEM IDENTIFICATION METHODS 11

2.1 Introduction to System Identification Methods 11
2.2 ARX Method 13
2.3 CTSI Method 16
2.4 SSEST Method 18
2.5 N4SID Method 20

CHAPTER THREE – ANALYSIS OF LUMPED PARAMETER MECHANICAL SYSTEM 31

3.1 Introduction 31
3.2 Analytical Solution 31

3.3 Finite Element Model 35
3.4 Identification of the Mechanical System 36

CHAPTER FOUR – VIBRATION ANALYSIS OF FLEXIBLE MANIPULATORS 43

4.1 Introduction 43
4.2 Experimental System 43
4.2.1 Experimental Modal Analysis 48
4.3 Finite Element Model 50

CHAPTER FIVE – IDENTIFICATION OF FLEXIBLE MANIPULATORS ..54

5.1 Introduction 54
5.2 Description of Cases 54
5.3 Definition of Inputs and Outputs 55
5.4 Identification Results of Steel Manipulator 58
5.4.1 Analysis of Identification Using the Finite Element Model 58
5.4.2 Analysis of Identification Using the Experimental Signals 63
5.5 Identification Results of Composite Manipulators 71

CHAPTER SIX – PASSIVE VIBRATION CONTROL OF FLEXIBLE MANIPULATORS 77

6.1 Introduction 77
6.2 S-Curve Motion Input 77
6.2.1 Design of S-curve Motion Input 77
6.2.2 Vibration Responses for S-curve Motion Input 82
6.3 Optimization of Motion Input with Genetic Algorithm 86
6.3.1 Flowchart of Genetic Algorithm 87
6.3.2 Vibration Responses for the Optimization 92

CHAPTER SEVEN – CONCLUSIONS 94

REFERENCES **96**

APPENDICES **105**

Appendix A List of Publications 105
Appendix B LabVIEW Codes for Experimental System 105
Appendix C Numerical Results of all the System Identification Methods 105
Appendix D Experimental Results of all the System Identification Methods 105

LIST OF FIGURES

Page

Figure 2.1 System identification flowchart 12

Figure 2.2 Model structure of ARX model 14

Figure 3.1 Four-dof mass-damper-spring system 31

Figure 3.2 Four-dof mechanical system 35

Figure 3.3 Vibration responses of fourth mass (a) identification (b) validation 36

Figure 3.4 Comparison of the vibration responses (a) $G_{11}(s)$, (b) $G_{21}(s)$, (c) $G_{31}(s)$ and (d) $G_{41}(s)$ for the identification dataset 38

Figure 3.5 Comparison of the vibration responses (a) $G_{11}(s)$, (b) $G_{21}(s)$, (c) $G_{31}(s)$ and (d) $G_{41}(s)$ for the validation dataset 39

Figure 3.6 Frequency responses of (a) $G_{11}(s)$, (b) $G_{21}(s)$, (c) $G_{31}(s)$ and (d) $G_{41}(s)$ transfer functions 42

Figure 4.1 Experimental system 44

Figure 4.2 Experimental system of the flexible manipulator with electric apparatus 44

Figure 4.3 Experimental system with the SM 47

Figure 4.4 Experimental system with the EGM-a and EGM-b 47

Figure 4.5 Experimental system with the ECM 48

Figure 4.6 Free vibration response of the flexible manipulator (a) time-domain acceleration response (b) frequency-domain acceleration response 49

Figure 4.7 (a) Dimensions and (b) finite element model of the curved manipulator 51

Figure 4.8 First mode shape of the flexible manipulator 52

Figure 4.9 The local and global axis of the manipulator 53

Figure 5.1 Trapezoidal motion profile 55

Figure 5.2 Input signal 57

Figure 5.3 Comparison of acceleration output signals.....57

Figure 5.4 Comparison of displacement output signals.....57

Figure 5.5 Comparison of the vibration responses obtained from (a) ARX (b) CTSI (c) SSEST (d) N4SID for identification dataset.....59

Figure 5.6 Comparison of the vibration responses obtained from (a) ARX (b) CTSI (c) SSEST (d) N4SID for validation dataset.....60

Figure 5.7 Comparison of the frequency responses obtained from (a) ARX (b) CTSI (c) SSEST (d) N4SID for SM-1.....62

Figure 5.8 Comparison of the vibration responses obtained from (a) ARX (b) CTSI (c) SSEST (d) N4SID for SM-1.....63

Figure 5.9 Comparison of the frequency responses obtained from (a) ARX (b) CTSI (c) SSEST (d) N4SID for SM-1.....64

Figure 5.10 Comparison of the vibration responses obtained from (a) ARX (b) CTSI (c) SSEST (d) N4SID for SM-3.....65

Figure 5.11 Comparison of the frequency responses obtained from (a) ARX (b) CTSI (c) SSEST (d) N4SID for SM-3.....66

Figure 5.12 Comparison of the vibration responses obtained from (a) ARX (b) CTSI (c) SSEST (d) N4SID for SM-5.....67

Figure 5.13 Comparison of identification results for (a) acceleration (b) displacement (c) strain signals.....70

Figure 5.14 Vibration responses of the EGM-a for (a) the CTSI method and (b) N4SID method.....72

Figure 5.15 Vibration responses of the EGM-b for (a) the CTSI method and (b) N4SID method.....72

Figure 5.16 Vibration responses of the ECM for (a) the CTSI method and (b) N4SID method.....72

Figure 5.17 Comparison of identification results for (a) EGM-a (b) EGM-b (c) ECM75

Figure 6.1 S-curve motion input.....78

Figure 6.2 Vibration responses: (a) SM-M1a t_{dec}=0.1 s (b) SM-M1a t_{dec}=2t_{1h} s (c) SM-M1b t_{dec}=0.1 s (d) SM-M1b t_{dec}=2t_{1h} s 82

Figure 6.3 Vibration responses: (a) SM-M3a t_{dec}=0.1 s (b) SM-M3a t_{dec}=2t_{1h} s (c) SM-M3b t_{dec} =0.1 s (d) SM-M3b t_{dec}=2t_{1h} s 83

Figure 6.4 Flowchart of the proposed control method..... 86

Figure 6.5 Genetic algorithm flowchart..... 87

Figure 6.6 Crossover (a) single-point (b) double-point 88

Figure 6.7 An example for mutation operator..... 88

Figure 6.8 The best and mean of population of (a) EGM-a (b) EGM-b 90

Figure 6.9 Vibration responses for (a) and (b) EGMa-M1 (c) and (d) EGMb-M1 .. 92

LIST OF TABLES

Page

Table 3.1 Identification results of (a) $G_{11}(s)$ and $G_{21}(s)$ (b) $G_{31}(s)$ and $G_{41}(s)$..... 37

Table 3.2 Identified natural frequencies 41

Table 4.1 Types of flexible manipulators..... 46

Table 4.2 Natural frequencies and damping ratios of the flexible manipulators 50

Table 5.1 Cases 55

Table 5.2 Identification results for the numerical analysis 61

Table 5.3 Identification results of (a) SM-1 and SM-2 (b) SM-3 and SM-4 68

Table 5.4 Identification results of SM-5 69

Table 5.5 Identification results of composite manipulators (a) $m_p = 0.62$ kg (b) $m_p = 1.24$ kg 74

Table 6.1 Time parameters of S-curve motion input for the SM 81

Table 6.2 RMS and reduction ratios for S-curve velocity profile 84

Table 6.3 Time parameters of motion inputs for the EGM-a and EGM-b 91

Table 6.4 RMS and reduction ratios for the EGM-a and EGM-b 93

LIST OF SYMBOLS

f_s	:Sampling frequency in Hz
Δt	:Time step
f_n	:Natural frequency in Hz
ω_n	:Natural frewuency in rad/sec
ξ	:Damping ratio
n	:Denominator coefficients of the CTSI method
m	:Numerator coefficients of the CTSI method
n_a	:Denominator coefficients of the ARX model
n_b	:Numerator coefficients of the ARX model
δ	:Logaritmic decrement
E	:Young modulus
ρ	:Density
ν	:Poisson ratio
α	:Rayleigh mass proportional damping coefficient
β	:Rayleigh stiffness proportional damping coefficient

ABBREVIATIONS

ARMAX	:Auto-Regressive Moving Average with Exogenous
ARX	:AutoRegressive eXogenous
SSEST	:State-Space ESTimation
N4SID	:Numerical Algorithms for Subspace State-Space System Identification
CTSI	:Continuous-Time System Identification
SM	:Steel Manipulator
GA	:Genetic Algorithm
SI	:System Identification
FPE	:Final Prediction Error
AIC	:Akaike information Criteria
MOESP	:Multivariable Output-Error State sPace
CVA	:Canonical Variate Anaysis
SSARX	:State Space Auto-Regressive eXogenous
MLE	:Maximum Likelihood Estimate
EGM-a	:Epoxy-Glass Manipulator with [0/90] lay up
EGM-b	:Epoxy-Glass Manipulator with [45/-45] lay up
ECM	:Epoxy-Carbon Manipulator with [0/90] lay up
FFT	:Fast Fourier Transform
CAD	:Computer-Aided Design
ERA	:Eigensystem Realization Algorithm
OKID	:Observer Kalman filter IDentification
MIMO	:Multi-Input Multi-Output

dof	:degree-of-freedom
PID	:Proportional Integral Derivative
FIR	:Finite Impulse Response
PEM	:Prediction Error Method
RMS	:Root Mean Square
SM-M1	:S-curve motion input for steel manipulator
EGMa-M1	:Motion input for Epoxy-Glass Manipulator with [0/90] lay up
EGMb-M2	:Motion input for Epoxy-Glass Manipulator with [45/-45] lay up
FE	:Finite Element

CHAPTER ONE
INTRODUCTION

1.1 Introduction

Lightweight manipulators are preferred in engineering applications such as manufacturing, machining, painting, and assembly because of lower production costs and energy consumption. However, they have some disadvantages because of flexibility. One of these disadvantages is especially residual vibrations that occur after the motion of a flexible manipulator stops. These vibrations affect the repeatability and performance of flexible manipulators. It is interesting for researchers to reduce residual vibrations and achieve higher repeatability and performance (Gao et al., 2012; Tokhi and Azad, 2017).

The modeling phase plays a crucial role in the successful dynamic analysis of flexible structures. Different methods can be used for modeling and vibration analysis. The complexity of flexible structures requires more effort to take into account their flexibility due to motor, joint, structure, and payload. The SI method enables to modeling of dynamic systems faster and more efficiently.

1.1.1 Literature Review on Modeling with System Identification Method

The SI methods are widely used to identify mathematical models of mechanical systems, beams, structures, and manipulators. In the literature, traditional identification methods, such as the ARX, ARMAX, Output Error methods, and subspace system identification methods are commonly employed to identify models of mechanical systems. A detailed literature survey on the modeling of mechanical systems and manipulators with the SI methods is reported.

Bu et al. (2003) studied experimental modeling and active vibration control of a flexible smart beam with the use of the ARX and ARMAX models for identification.

Saad et al. (2015) used the ARX method to identify a mathematical model of a flexible beam and studied the vibration control with a conventional PID controller tuned by differential evolution and genetic algorithms. Zardian et al. (2015) performed the vibration control of a mathematical model of a flexible manipulator obtained with the ARX model with a PID controller optimized with genetic algorithm and particle swarm optimization. Ziaei & Wang (2006) worked on modeling flexible manipulators with generalized orthonormal basis functions, ARX, ARMAX, and FIR methods via simulation and experiment. Łuczak & Nowopolski (2014) worked on the parameter identification of two-mass and multi-mass mechanical systems in electrical drives using the ARX and Output Error models. Nguyen et al. (2022) proposed a novel approach using a Kalman filter with the time series ARX model to identify a cantilever beam and a manipulator via simulations and experiments. Malgaca et al. (2019) studied modeling of a five-dof half vehicle system with the ARX model and vibration control with the PID controller via dynamical simulations. Song et al. (2017) studied identification of a multi-source excitations floating raft active vibration isolation system with the ARX model and obtained four discrete-time transfer functions of the system.

Garnier et al. (2003) proposed a new identification approach to obtain continuous-time transfer function models from discrete-time data and the proposed method was evaluated with Monte Carlo simulations. Ozdemir & Gumussoy (2017) studied the black-box and grey-box CTSI method from frequency response measurements, the algorithm performance was evaluated with the randomly generated models. Malgaca et al. (2020) identified a continuous-time transfer function of a planar manipulator via experimental dataset with the CTSI approach. Malgaca & Lök (2022) studied modeling and passive vibration control of a single-link curved manipulator using the CTSI method via experimental signals. Malgaca & Lök (2017) investigated vibration analysis of the L-frame with the CTSI method using a simulation dataset obtained from the finite element model of the system.

Gumussoy et al. (2018) studied modeling with simulation and real data using subspace identification approaches, such as SSEST and N4SID. Kim (2013) compared the subspace-based system identification techniques, such as the N4SID, SSEST, and PEM techniques, for various systems such as a CD player arm, the processing system of the glass furnace, robots, the fetal electrocardiogram, and heating systems. Benyamin et al. (2017) studied black-box modeling with the N4SID estimation approach and grey-box modeling with the SSEST estimation approach of a flapping wings micro aerial vehicle.

Dong et al. (2006) used the OKID method to estimate a mathematical model of an aluminum cantilever plate with numerical and experimental datasets Valasek & Chen (2003) studied how to identify a locally linear dynamic model of a nonlinear AV-SB Harrier with six degrees of freedom. In (Tiano et al., 2007), linear and nonlinear yaw dynamics of an autonomous underwater vehicle were modeled with the OKID method via simulation and experiment. Sensor fault detection of an unmanned aerial vehicle was studied in (Heredia & Ollero, 2011). In (Yang et al., 2006), identification of a five-story shear-beam type building was studied using vibration signals. In (Abreu et al., 2012a), a state-space model of an aluminum beam was estimated with the ERA/OKID method, and the estimated state-space model was used for vibration control of the beam. In (Gagg F et al., 2014), a mathematical model of a cantilever beam was estimated by the ERA/OKID method, and the Hankel norm model was used to reduce the model degree of the estimated mathematical model. In (Ni et al., 2020), the payload parameters such as mass and moment of inertia of a flexible space manipulator were determined by the OKID algorithm and the estimated parameters were compared with those obtained using the classical recursive least squares method. In (Favoreel et al., 2000a), the prediction error and subspace identification methods such as N4SID, IV-4SID, the Canonical Variate Analysis (CVA), and Multivariable Output-Error State sPace (MOESP), were compared using real-life datasets. Pappalardo & Guida (2018) studied the modeling of a full-car vehicle model with the ERA-OKID method and identified modal parameters of the system.

The mathematical modeling of a two-dof parallel robot and its vibration suppression were studied in (Douat et al., 2013). In (Junior et al., 2016), a mathematical model of a five-dof robot manipulator was estimated by the subspace description method. In (Costa et al., 2017), a mathematical model of a prototype of a jaw crusher was modeled using the N4SID method with the MOESP weighting matrix. In (Pappalardo et al., 2021), the N4SID algorithm was used for modeling an aircraft hatch door, and the results of the MOESP and CVA weight matrices were compared. In (Pappalardo et al., 2023a,b), a comparative analysis is presented for the modeling of a three-story frame lumped parameter model with N4SID and OKID via numerical and experimental datasets.

Subramanian et al. (2021) identified a full-tank system with the prediction error method and the N4SID method, then demonstrated the superiority of the N4SID method with different input signals. Borjas & Garcia (2011) investigated and compared four subspace identification techniques, namely, the N4SID, IV-4SID, MOESP, and CVA methodologies, for ten industrial processes. Juricek et al. (2001) compared various identification techniques for modeling a MIMO system and observed that the MOESP and CVA approaches had the most successful results. In (Tronci et al., 2017), the authors worked on vibration analysis of a civic tower at Rieti with the use of the OKID method for identifying the first five mode shapes of the tower. Favoreel et al. (1999) compared the most used subspace identification approaches, which are the N4SID, CVA, and MOESP methods, using 15 publicly available experimental data sets. Heredia & Ollero (2009) applied the ERA/OKID identification algorithm to real helicopter flight data for sensor failure detection of a small autonomous helicopter. Guida et al. (2009) used the ERA/OKID identification method to identify the parameters of a linear mechanical system on a lightly-damped mechanical apparatus.

Chang & Pakzad (2014) worked on the development of the OKID subspace identification technique and its comparison with the ARX and N4SID techniques. In (Qin, 2006), the author presented substantial identification techniques for open-loop

and closed-loop systems. Wang & Hsu (2008) proposed a novel identification algorithm based on the OKID technique to estimate unknown dynamic systems. Skolnik et al. (2006) studied to estimate structural frequencies, damping rates, and mode shapes of the first nine modes for a fifteen-story steel structure with a real earthquake dataset and used an FE model of the building to improve the data correlation. Qidwai & Bettayeb (2003) investigated a substantial identification technique for defect detection in metals and tested it with real ultrasonic vibrations. In (Bathelt & Jelali, 2014), subspace identification methods such as the MOESP, N4SID, and ORT methods, and their variations were compared using chemical process datasets. Tuhta et al. (2019) used the N4SID method to estimate the state-space model of an industrial building. The authors used the same method for the identification of an RC building (Tuhta & Günday, 2019). Gautier et al. (2013) presented a new subspace fitting method that obtains the rigidity of an experimental rotating machine by minimizing the correlation between the theoretical observability matrix and the experimental observability matrix estimated using the MOESP method.

The large number of research papers briefly discussed in this survey concerning the numerical procedures of applied SI shows the engineering importance of the problem analyzed in this thesis.

1.1.2 Literature Review on Vibration Control

In this subsection, a detailed literature survey on passive and active vibration control methods for mechanical structures and flexible manipulators is reported. Residual vibrations of mechanical systems and flexible manipulators can be suppressed by active (Abreu et al., 2012b; Bu et al., 2003; Chen et al., 2018; Saad et al., 2015; Takahashi et al., 2002) and passive (Mimmi & Pennacchi, 2001; Pereira et al., 2012; Shan et al., 2005) control methods. Active vibration control methods require a closed-loop system with a controller, an actuator, and a sensor. In contrast, passive vibration control methods do not require any external energy input or actuator deployment. Passive vibration control is achieved through an open-loop system

without additional hardware and energy. Different motion inputs such as triangle, trapezoidal, and S-curve are used for passive vibration control of the flexible manipulators (Ankaralı et al., 2012; Fang et al., 2019).

Passive vibration control of single-link flexible planar and curved manipulators was studied with triangle and trapezoidal motion inputs. The motion parameters of inputs were determined based on the fundamental frequency of the manipulator in (Malgaca et al., 2016). Residual vibrations of single-link epoxy-glass manipulators with [0/90] and [45/-45] lay-ups were reduced with the triangle and trapezoidal motion inputs for various stopping positions in (Yavuz et al., 2016b). A new method was proposed to reduce residual vibrations of a single-link glass fabric-reinforced epoxy-glass composite manipulator by adding an exponential-harmonic velocity profile to the end of the trapezoidal motion input in (Yavuz, 2019). Then, the proposed method was implemented in a flexible non-uniform shaped manipulator to suppress residual vibrations of the manipulator in (Yavuz, 2021).

A novel S-curve trajectory planning is presented for highspeed and ultra-precision operation of a 3-DOF robot manipulator in (Fang et al., 2019). To improve the performance of conventional S-curve, motion profile generation methods are proposed in (Li et al., 2009) and (Nguyen et al., 2008). A new method that combines continuous input shaping and the S-curve motion is proposed to reduce settling time and increase productivity in (Liu & Chen, 2018). In addition to the conventional S-curve motion, asymmetric profiles are studied and the effect of asymmetricity on vibration suppression was investigated to reduce vibrations of X-Y stages in (Ha et al., 2012) and (Rew et al., 2009). Time of S-curve command is minimized for vibration-free transfer process with two approaches such as embedding and shaping method in (Tho et al., 2020). A five-segment S-curve motion input was designed by excluding linear deceleration segments, motion parameters of the input were selected based on the first frequency of the manipulator in (Malgaca & Lök, 2022).

The GA method is an optimized method generally used in literature for active vibration control and trajectory control of mechanical structures and manipulators. A literature survey is summarized below. A new PID tuning method by the Gain-Phase Margin and the GA methods is improved and implemented in CNC Lathe, CNC milling machine, and an industrial PUMA robot to evaluate the effectiveness of the proposed approach in (Jaen-Cuellar et al., 2013). Optimization of the PD controller parameters with the GA method is studied to reduce residual vibrations of single-link smart and composite manipulators with different orientation lay-ups in (Uyar & Malgaca, 2023).

In (Choubey & Ohri, 2021), the linear quadratic regulator-PID controller parameters were optimized with the GA, particle swarm optimizer, and grey wolf optimizer for trajectory tracking control of a three-degree-of-freedom Maryland parallel manipulator. Kankashvar et al. (2015) studied the PID tuning of a five-bar linkage robot manipulator with a novel biogeography-based optimization, GA and particle swarm optimization methods.

1.2 Scope, Contributions and Orginality of the Thesis

This thesis presents significant contributions in the field of modeling and passive vibration control of steel and composite manipulators using the SI methods. The primary focus is on the modeling of single-link manipulators using identification methods that involve both simulation and experimental signals. The modeling phase is important for the success of dynamic analysis and vibration control of flexible structures and manipulators. The mathematical models of the manipulators are identified through the implementation of the ARX, CTSI, SSEST, and N4SID methods. To evaluate the performance of the identification methods, flexible manipulators are modeled with various output types, including acceleration, displacement, and strain, along with different payloads. Moreover, to investigate the impact of different materials on the modeling process, four distinct manipulators as

steel, epoxy-carbon, and epoxy-glass with two different orientation lay-ups are considered.

Another important contribution of this thesis is the design of an S-curve motion input aimed to eliminate residual vibrations of the single-link curved manipulator. While the ideal S-curve motion input consists of seven segments, the designed S-curve motion input in this thesis consists of five segments. The designed five-segment S-curve motion input is based on the modal parameters of the manipulator, excluding linear acceleration and deceleration segments. The designed S-curve motion inputs, with different stopping positions and motion times, are utilized for vibration control of the manipulator with various payloads.

Furthermore, a novel passive control approach is proposed in this thesis to reduce the vibrations of the single-link composite manipulators. Due to the higher flexibility of composite manipulators compared to steel manipulators, the trapezoidal and S-curve motion inputs commonly used in the literature are insufficient to suppress the residual vibration of composite manipulators. In the proposed approach, mathematical models of the composite manipulators are identified using the SI method. Subsequently, the time parameters that minimize the Root Mean Square (RMS) values of vibrations are obtained using the GA method based on the identified mathematical models. The effectiveness of the proposed method is evaluated by comparing the experimental vibration responses with the optimized time parameters.

1.3 Organization of the Thesis

This thesis is organized considering the following structure. Chapter One presents an introduction, literature review, scope, contributions and originality of the thesis. A literature survey about modeling of mechanical structure and flexible manipulators with the SI methods and passive vibration control of the manipulators is presented in Chapter 1.

In Chapter 2, a comprehensive description of the SI method and implementation steps of the method are presented. Moreover, mathematical backgrounds of the ARX, CTSI, SSEST, and N4SID approaches used for modeling a four-degrees-of-freedom system and flexible manipulators are given. The ARX and CTSI methods are utilized to obtain discrete-time and continuous-time transfer functions of the system, respectively. Similarly, the N4SID and SSEST methods are employed to obtain discrete-time and continuous-time state-space models of the system, respectively.

Chapter 3 presents the analytic solution and FE model of a four-degrees-of-freedom mass-damper-spring system. The continuous-time transfer functions of the system are identified using a simulation dataset obtained from the FE model of the system with the CTSI method. The selection of model orders and model parameters for the CTSI method is described in detail.

Chapter 4 provided a detail description of the FE model and experimental system of flexible manipulators. The FE model of the SM is created in ANSYS/APDL software to obtain the simulation dataset. The experimental system is built to synchronously drive the servo motor and measure sensor signals to obtain the experimental dataset. First natural frequencies and damping ratios of the steel and composite manipulators are obtained with experimental modal analysis.

In Chapter 5, modeling of the steel and composite manipulators is studied with the SI methods. The mathematical models of the SM identified with the ARX, CTSI, SSEST and N4SID methods, considering with various output types and different payloads. Similarly, the CTSI and N4SID methods are employed to model the epoxy-carbon and epoxy-glass manipulators, utilizing the knowledge obtained from the modeling of the SM. A comparative analysis of numerical and experimental identification results is presented.

Chapter 6 presented passive vibration control results of steel and composite manipulators with S-curve motion input and Trapezoidal motion input optimized with the GA approach. The vibration response obtained from the experimental system and the identified model are compared for the designed S-curve motion input considering different stopping positions and motion times along with different payloads. The performance of the designed S-curve motion input is evaluated based on the reduction ratios provided in the table. Moreover, a detailed description of the proposed vibration control approach with the GA is presented. The proposed approach is utilized to suppress the vibration response of the composite manipulators.

In Chapter 7, the main contributions of the thesis are reported and future works are discussed briefly.

Appendix A presents journal and conference papers derived from the research conducted in this thesis. Appendix B presents LabVIEW code examples prepared for the experimental systems. In Appendix C and D, numerical and experimental results obtained from the application of the SI methods are provided for the SM, respectively.

CHAPTER TWO
SYSTEM IDENTIFICATION METHODS

2.1 Introduction to System Identification Methods

SI is a method that is used to estimate mathematical models of a dynamic system by using the input and output signals of the system. The SI method is separated into three modeling approaches; the white-box model, the gray-box model, and the black-box model. In the white-box model, the mathematical model of the dynamic system is found using physical laws. This type of modeling is generally used for modeling simple systems. In the gray-box model, both the physical laws and the experimental data obtained are used for modeling. The mathematical model of the system is obtained by using solely the experimental data of the system in the black-box model (Ljung, 1999; Keesman, 2011; Juang & Phan, 2001; Garnier & Liuping, 2008).

The SI method consists of five steps. Flowchart of the identification method is shown in Figure 2.1.

The first step is to create the data set to be used in the SI method. The data set can be obtained experimentally or using simulation. The second step is the preprocessing step. The data set obtained in this step is subjected to various pre-processes such as filtering and normalization in order to make it suitable for system modeling. The third step is the most important step of the SI method. In this step, the most suitable model is determined from the identification methods.

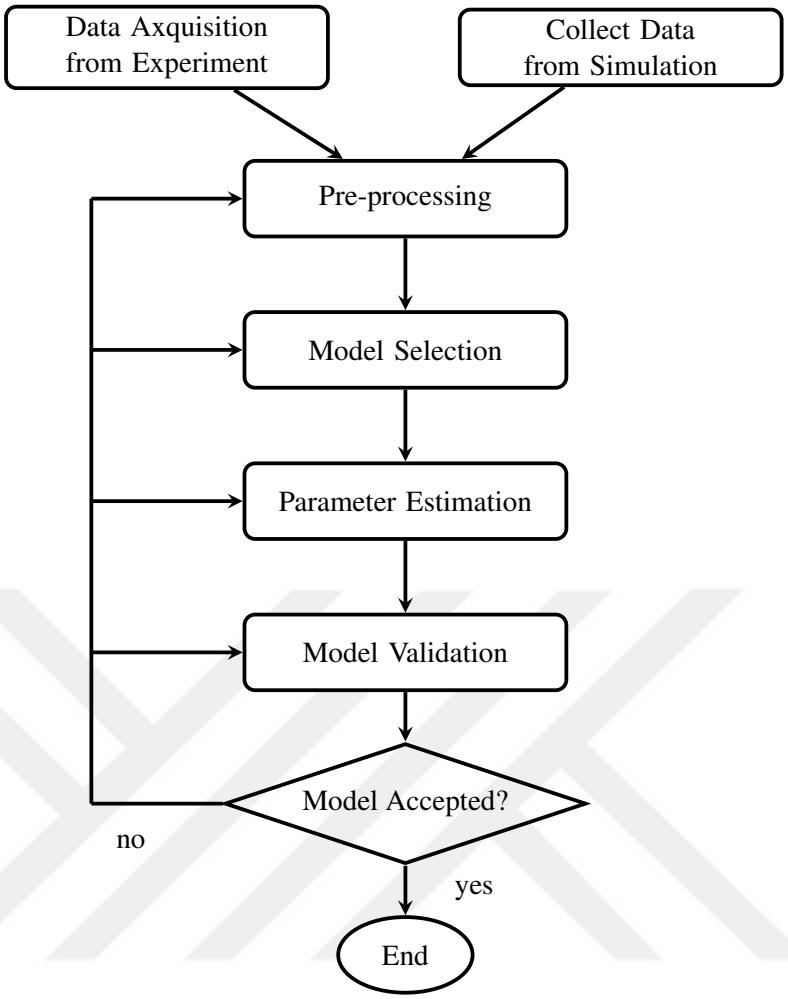


Figure 2.1 System identification flowchart

In the fourth step, the mathematical model coefficients are chosen using criteria such as the Akaike information criterion (AIC) and the Final Prediction Error criterion (FPE), which optimize model complexity and the success of fit (Ljung, 1999; Keesman, 2011). The FPE is calculated using the formula given as follows:

$$FPE = \left(\frac{1 + d/N}{1 - d/N}\right) \frac{1}{N} \sum_{t=1}^{N} \varepsilon(t, \hat{\vartheta})(\varepsilon(t, \hat{\vartheta}))^T \tag{2.1}$$

where ε is the error of the estimation, d is the number of parameters, and N is the number of samples. For the evaluation and choosing of the model coefficients, fit values are calculated for each identified model. The fit values between experimental signals and identified signals are computed as follows:

$$fit = 100\left(1 - \frac{||y - \hat{y}||}{||y - mean(y)||}\right) \tag{2.2}$$

where y is real experimental data and $\hat{y}$ is estimated data. The fit value is obtained as a percentage.

In the last step, model validation is performed. In the SI method, two datasets are used, such as the identification and validation datasets. The identification dataset is utilized to estimate the model of the system, while the validation dataset is used to test the accuracy and reliability of the identified model. Subsequently, If the identified model is not suitable, the required identification step is returned in accordance with the dynamical behaviour of the system (Ljung, 1999; Keesman, 2011).

In this thesis, the ARX, the CTSI, the SSEST, and the N4SID methods are utilized to identify a four-dof mechanical system and single-link flexible manipulators. The SI methods used in the thesis are described below.

2.2 ARX Method

The ARX model is a traditional identification approach widely employed in the literature. The model structure of the ARX model is shown in Figure 2.2.

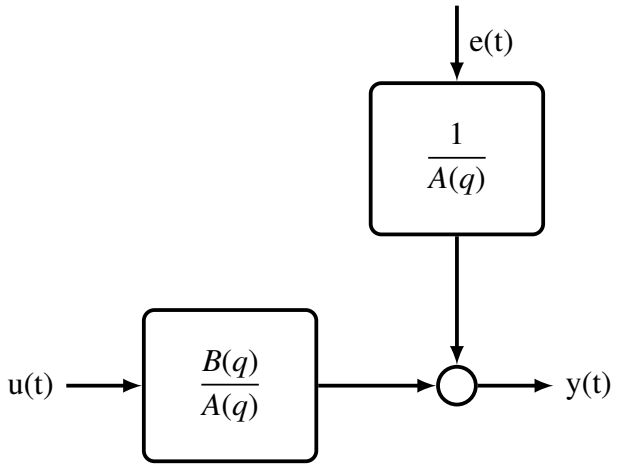


Figure 2.2 Model structure of ARX model

In Figure 2.2, $u(t)$, $y(t)$ and $e(t)$ represent input, output signals and error term of a system, respectively. In general, an ARX model has an AutoRegressive part denoted with $A(q)\mathbf{y}(t)$ and an eXogenous part denoted with $B(q)\mathbf{u}(t)$, which can be represented in explicit form as follows:

$$\mathbf{y}(t) = \frac{B(q)}{A(q)}\mathbf{u}(t) + \frac{1}{A(q)}\mathbf{e}(t) \tag{2.3}$$

where q is the delay operator, t is the continuous-time variable, whereas $\mathbf{u}(t)$, $\mathbf{y}(t)$, and $\mathbf{e}(t)$ respectively define the input vector with dimensions $n_u \times 1$, the output vector with dimensions $n_y \times 1$, and the white noise error term with dimensions $n_e \times 1$, being $n_u = n_y = n_e = N$. On the other hand, $A(q)$ and $B(q)$ are two different polynomials, expressed in terms of the variable q and constructed with unknown real coefficients, which can be defined as follows:

$$A(q) = \sum_{i=1}^{n_a} a_i q^{-i} = 1 + a_1 q^{-1} + a_2 q^{-2} + \ldots + a_{n_a} q^{-n_a} \tag{2.4}$$

and

$$B(q) = \sum_{j=1}^{n_b} b_j q^{-j} = b_1 q^{-1} + b_2 q^{-2} + \ldots + b_{n_b} q^{-n_b} \tag{2.5}$$

where coefficients $a_i, i = 1, 2, \ldots, n_a$ and $b_j, j = 1, 2, \ldots, n_b$ are the real coefficients associated with each term of the ARX polynomials denoted with $A(q)$ and $B(q)$, while n_a and n_b are their orders, respectively. The unknown coefficients of the polynomials that appear in the ARX model can be grouped into the following parameter vector:

$$\boldsymbol{\vartheta} = [a_1, a_2, \ldots, a_{n_a}, b_1, b_2, \ldots, b_{n_b}]^T \tag{2.6}$$

where $\boldsymbol{\vartheta}$ represent a vector of unknown parameters containing the real coefficients of the polynomials $A(q)$ and $B(q)$ having dimensions $(n_a + n_b) \times 1$. The set of unknown coefficients of the ARX polynomials can be readily estimated with an ordinary least-square estimation method. To this end, one needs first to assemble the following coefficient matrix formed by the input and output measurements actually available for the dynamical system to be identified:

$$\boldsymbol{\Phi} = \begin{bmatrix} \mathbf{Y} & \mathbf{U} \end{bmatrix} \tag{2.7}$$

where:

$$\mathbf{Y} = \begin{bmatrix} -\mathbf{y}(n_a - 1) & -\mathbf{y}(n_a - 2) & \ldots & -\mathbf{y}(0) \\ -\mathbf{y}(n_a) & -\mathbf{y}(n_a - 1) & \ldots & -\mathbf{y}(1) \\ -\mathbf{y}(n_a + 1) & -\mathbf{y}(n_a) & \ldots & -\mathbf{y}(2) \\ \vdots & \vdots & \ddots & \vdots \\ -\mathbf{y}(N - 1) & -\mathbf{y}(N - 2) & \ldots & -\mathbf{y}(N - n_a) \end{bmatrix} \tag{2.8}$$

and

$$\mathbf{U} = \begin{bmatrix} \mathbf{u}(n_a - 1) & \mathbf{u}(n_a - 2) & \ldots & \mathbf{u}(n_a - n_b) \\ \mathbf{u}(n_a) & \mathbf{u}(n_a - 1) & \ldots & \mathbf{u}(n_a - n_b + 1) \\ \mathbf{u}(n_a + 1) & \mathbf{u}(n_a) & \ldots & \mathbf{u}(n_a - n_b + 2) \\ \vdots & \vdots & \ddots & \vdots \\ \mathbf{u}(N - 1) & \mathbf{u}(N - 2) & \ldots & \mathbf{u}(N - n_b) \end{bmatrix} \tag{2.9}$$

where it is assumed that $n_u = n_y = N$, as mentioned before, and $\mathbf{\Phi}$ represents the regressor matrix having dimensions $n_y \times (n_a + n_b)$, while $\mathbf{Y}$ and $\mathbf{U}$ are two submatrices of dimensions $n_y \times n_a$ and $n_u \times n_b$ that form the main regressor matrix $\mathbf{\Phi}$ containing output and input measurements, respectively. Therefore, the least-square estimation process arises from the rearrangement of Equation (2.3) in matrix form and leads to the following result:

$$\hat{\boldsymbol{\vartheta}} = \mathbf{\Phi}^{+}\mathbf{y} = (\mathbf{\Phi}^{T}\mathbf{\Phi})^{-1}\mathbf{\Phi}\mathbf{y} \tag{2.10}$$

where $\hat{\boldsymbol{\vartheta}}$ represents an estimation of the unknown parameter vector of dimensions $(n_a + n_b) \times 1$ and $\mathbf{\Phi}^{+}$ is the Moore-Penrose pseudo-inverse matrix of dimensions $(n_a + n_b) \times n_y$ associated with the regressor matrix $\mathbf{\Phi}$.

2.3 CTSI Method

In the literature, there are two basic approaches to the CTSI method. These are the direct approach and the indirect approach. The indirect approach consists of two parts. Firstly, the model of the system is identified with the discrete-time identification methods. Subsequently, the identified discrete-time model is translated to the continuous-time model. In the direct approach, the mathematical model of the system is directly identified with the CTSI method (Garnier & Liuping, 2008; Garnier et al., 2003).

$$y(t) = G(p)u(t) \tag{2.11}$$

where

$$G(p) = \frac{b_0 + b_1 p + \ldots b_m p^m}{a_0 + a_1 p + \ldots a_n p^n}, \quad a_0 = 1 \tag{2.12}$$

where p is the differential operator, the vectors $u(t)$ and $y(t)$ are respectively input and output of the system, $G(p)$ represents the identified model of the system, a and b coefficients are respectively numerator and denominator coefficients of the identified model, while p, m and n denote derivative operator, order of numerator and order of denominator, respectively.

$$a_0 y_u(t) + a_1 y_u^{(1)}(t) + \ldots + y_u^{(n)}(t) = b_0 u(t) + b_1 u^{(1)}(t) + \ldots + b_m u^{(m)}(t) \tag{2.13}$$

$$A(s)Y_u(s) = B(s)U(s) + C(s) \tag{2.14}$$

where

$$A(s) = \sum_{i=0}^{n-1} a_i s^i + s^n, \quad B(s) = \sum_{i=0}^{m} b_i s^i, \quad C(s) = \sum_{i=0}^{n-1} c_i s^i \tag{2.15}$$

where s denotes the Laplace variable, whereas $Y_u(s)$ and U(s) represent the Laplace transform of $y_u(t)$ and $u(t)$.

$$A(s)F(s)Y_u(s) = B(s)F(s)U(s) + F(s)C(s) \tag{2.16}$$

2.4 SSEST Method

The acronym SSEST stands for the State-Space ESTimation method (Ljung et al., 2015; Banazadeh et al., 2019). In this subsection, the main features of the SSEST approach are described. The SSEST approach is employed to obtain the state-space model of a dynamic system using time-domain data or frequency-domain data. The SSEST method is based on initializing the model parameters using a subspace approach, such as the one based on the numerical methods for subspace state-space system identification, followed by the use of an iterative method that employs a prediction error and a minimization algorithm to improve the quality of the identified model. As discussed below, the initialization of the SSEST method is based on the use of the N4SID method. Therefore, the MOESP, CVA, and SSARX weighting matrices are analyzed when using the SSEST method, and the best result is typically obtained considering the CVA set of weighting matrices. On the other hand, the improvement of the estimation of the continuous-time state-space matrices indicated as **A**, **B**, **C**, and **D** with the use of the iterative method based on the SSEST technique is synthetically explained below.

The discretization of a continuous-time state-space model of a dynamical system leads to an approximate discrete-time state-space model given as follows:

$$\begin{cases} \mathbf{z}(k+1) = \mathbf{A}_d\mathbf{z}(k) + \mathbf{B}_d\mathbf{u}(k) \\ \mathbf{y}(k) = \mathbf{C}\mathbf{z}(k) + \mathbf{D}\mathbf{u}(k) + \mathbf{e}(k) \end{cases} \tag{2.17}$$

where $\mathbf{u}(k)$, $\mathbf{y}(k)$, $\mathbf{z}(k)$, and $\mathbf{e}(k)$ respectively represent the input vector having dimensions $n_u \times 1$, the output vector having dimensions $n_y \times 1$, the state vector having dimensions $n_z \times 1$, and the error vector having dimensions $n_y \times 1$, while $\mathbf{A}_d$, $\mathbf{B}_d$, $\mathbf{C}$, and $\mathbf{D}$ denote the discrete-time matrices of the state-space model having dimensions $n_z \times n_z$, $n_z \times n_u$, $n_y \times n_z$, and $n_y \times n_u$, respectively. The use of the Maximum Likelihood Estimate (MLE) of the discrete-time matrices forming the state-space model leads to the following set of equations:

$$\min(e), \quad e = e(\mathbf{y}, \mathbf{z}, \mathbf{u}, \mathbf{C}, \mathbf{D}) \tag{2.18}$$

where

$$e = \sum_{i=1}^{N} \|\mathbf{y}(k) - \mathbf{C}\hat{\mathbf{z}}(k) - \mathbf{D}\mathbf{u}(k)\|^2 \tag{2.19}$$

and

$$\hat{\mathbf{z}}(k+1) = \mathbf{A}_d\hat{\mathbf{z}}(k) + \mathbf{B}_d\mathbf{u}(k) \tag{2.20}$$

where e represents the prediction error and the vector $\hat{\mathbf{z}}(k)$ represents the estimation of the vector $\mathbf{z}(k)$. Considering the MLE approach, Equation (2.18), which represents the fundamental equation for the definition of the SSEST method, can be mathematically reformulated as follows:

$$\min(V), \quad V = V(\mathbf{y}, \mathbf{u}, \mathbf{A}_d, \mathbf{B}_d, \mathbf{C}, \mathbf{D}) \tag{2.21}$$

where

$$V = \sum_{i=1}^{N} \|\mathbf{y}(k) - \hat{\mathbf{y}}(k|\mathbf{A}_d, \mathbf{B}_d, \mathbf{C}, \mathbf{D})\|^2 \tag{2.22}$$

and

$$\hat{\mathbf{y}}(k|\mathbf{A}_d, \mathbf{B}_d, \mathbf{C}, \mathbf{D}) = \mathbf{D}\mathbf{u}(k) + \mathbf{C}\sum_{j=1}^{k}\left(\mathbf{A}_d^{k-j}\mathbf{B}_d\mathbf{u}(j)\right) \tag{2.23}$$

where V represents the performance index of the identification algorithm to be

minimized and $\hat{\mathbf{y}}(k)$ is the identified output vector associated with the vector $\mathbf{y}(k)$. It is worth noticing that, for a fixed couple of the $\mathbf{A}_d$ and $\mathbf{C}$ matrices, the vector $\hat{\mathbf{y}}(k)$ is a linear function of the matrices $\mathbf{B}_d$ and $\mathbf{D}$, and, for a fixed couple of the $\mathbf{A}_d$ and $\mathbf{B}_d$ matrices, the vector $\hat{\mathbf{y}}(k)$ is a linear function of the matrices $\mathbf{C}$ and $\mathbf{D}$. Therefore, the matrices $\mathbf{B}_d$ and $\mathbf{D}$ can be re-estimated through a simple linear least-squares estimation method for given iterative values of the matrices $\mathbf{A}_d$ and $\mathbf{C}$. Then, the matrices $\mathbf{C}$ and $\mathbf{D}$ can be re-estimated again through a least-square estimation method for given iterative values of the matrices $\mathbf{A}_d$ and $\mathbf{B}_d$. After the matrices $\mathbf{B}_d$, $\mathbf{C}$, and $\mathbf{D}$ are re-estimated, the matrix $\mathbf{A}_d$ can be re-estimated using Equation (2.21), and the re-estimated $\mathbf{B}_d$, $\mathbf{C}$, and $\mathbf{D}$ matrices can be obtained as well. The iterative identification process that characterize the SSEST method ends when a prescribed tolerance for the error given by Equation (2.18) is met or when an assigned maximum number of finite iteration is reached.

2.5 N4SID Method

The acronym N4SID stands for Numerical Algorithms for Subspace State-Space System Identification method (Van Overschee & De Moor, 2012; Favoreel et al., 2000b). In this subsection, the fundamental steps of the N4SID approach are described in detail. To this end, consider the following state-space model of a general structural system:

$$\begin{aligned} \mathbf{z}(k+1) &= \mathbf{A}_d\mathbf{z}(k) + \mathbf{B}_d\mathbf{u}(k) \\ \mathbf{y}(k) &= \mathbf{C}\mathbf{z}(k) + \mathbf{D}\mathbf{u}(k) \end{aligned} \tag{2.24}$$

where k denotes the discrete-time variable, $\mathbf{z}(k)$, $\mathbf{y}(k)$, and $\mathbf{u}(k)$ respectively represent the discrete-time state vector with dimensions $n_z \times 1$, the discrete-time output vector with dimensions $n_y \times 1$, and the discrete-time input vector with dimensions $n_u \times 1$, while the matrices $\mathbf{A}_d$, $\mathbf{B}_d$, $\mathbf{C}$, and $\mathbf{D}$ denote the discrete-time state matrix having dimensions $n_z \times n_z$, the discrete-time input influence matrix having dimensions $n_z \times n_u$, the output influence matrix having dimensions $n_y \times n_z$, and the direct

transmission matrix having dimensions $n_y \times n_u$, respectively.

The discrete-time state-space model of a generic mechanical system can be rewritten with the use of the past and future inputs and outputs as follows:

$$\begin{cases} \mathbf{Y}_p = \mathbf{\Gamma}_i \mathbf{Z}_p + \mathbf{H}_i \mathbf{U}_p \\ \mathbf{Y}_f = \mathbf{\Gamma}_i \mathbf{Z}_f + \mathbf{H}_i \mathbf{U}_f \\ \mathbf{Z}_f = \mathbf{A}_d^i \mathbf{Z}_\mathbf{p} + \mathbf{\Delta}_i \mathbf{U}_p \end{cases} \tag{2.25}$$

where l represents the length of the data record, whereas i and j are two integer numbers. The matrices denoted with $\mathbf{\Gamma}_i$, $\mathbf{\Delta}_i$, and $\mathbf{H}_i$ represent the observability matrix of dimensions $n_y i \times n_z$, the controllability matrix of dimensions $n_z \times n_u i$, and the discrete-time state-space Toeplitz matrix of dimensions $n_y i \times n_u i$, respectively. The matrices expressed with $\mathbf{U}_p$, $\mathbf{U}_f$, $\mathbf{Y}_p$, and $\mathbf{Y}_f$ are rectangular matrices that identify the Hankel matrix of the past inputs with dimensions $in_u \times j$, the Hankel matrix of future inputs with dimensions $in_u \times j$, the Hankel matrix of past outputs with dimensions $in_y \times j$, and the Hankel matrix of future outputs with dimensions $in_y \times j$, respectively. The matrices $\mathbf{U}_p$, $\mathbf{U}_f$, $\mathbf{Y}_p$, and $\mathbf{Y}_f$ can be respectively written as follows:

$$\mathbf{U}_p = \begin{bmatrix} \mathbf{u}(0) & \mathbf{u}(1) & \cdots & \mathbf{u}(j-1) \\ \mathbf{u}(1) & \mathbf{u}(2) & \cdots & \mathbf{u}(j) \\ \vdots & \vdots & \ddots & \vdots \\ \mathbf{u}(i-1) & \mathbf{u}(i) & \cdots & \mathbf{u}(i+j-2) \end{bmatrix} \tag{2.26}$$

$$\mathbf{U}_f = \begin{bmatrix} \mathbf{u}(i) & \mathbf{u}(i+1) & \cdots & \mathbf{u}(i+j-1) \\ \mathbf{u}(i+1) & \mathbf{u}(i+2) & \cdots & \mathbf{u}(i+j) \\ \vdots & \vdots & \ddots & \vdots \\ \mathbf{u}(2i-1) & \mathbf{u}(2i) & \cdots & \mathbf{u}(2i+j-2) \end{bmatrix} \tag{2.27}$$

$$\mathbf{Y}_p = \begin{bmatrix} \mathbf{y}(0) & \mathbf{y}(1) & \cdots & \mathbf{y}(j-1) \\ \mathbf{y}(1) & \mathbf{y}(2) & \cdots & \mathbf{y}(j) \\ \vdots & \vdots & \ddots & \vdots \\ \mathbf{y}(i-1) & \mathbf{y}(i) & \cdots & \mathbf{y}(i+j-2) \end{bmatrix} \tag{2.28}$$

$$\mathbf{Y}_f = \begin{bmatrix} \mathbf{y}(i) & \mathbf{y}(i+1) & \cdots & \mathbf{y}(i+j-1) \\ \mathbf{y}(i+1) & \mathbf{y}(i+2) & \cdots & \mathbf{y}(i+j) \\ \vdots & \vdots & \ddots & \vdots \\ \mathbf{y}(2i-1) & \mathbf{y}(2i) & \cdots & \mathbf{y}(2i+j-2) \end{bmatrix} \tag{2.29}$$

Theoretically, the parameter i and j can be chosen arbitrarily. However, as the length of the data record l and the dimension of the parameters i and j increase, the prediction success of the state-space model increases. The past state matrix denoted with $\mathbf{Z}_p$ having dimension $n_z \times j$ and the future state matrix denoted with $\mathbf{Z}_f$ having dimension $n_z \times j$ can be written as follows:

$$\mathbf{Z}_p = \begin{bmatrix} \mathbf{z}(0) & \mathbf{z}(2) & \ldots & \mathbf{z}(j-1) \end{bmatrix} \tag{2.30}$$

and

$$\mathbf{Z}_f = \begin{bmatrix} \mathbf{z}(i) & \mathbf{z}(i+1) & \ldots & \mathbf{z}(i+j-1) \end{bmatrix} \tag{2.31}$$

The observability matrix denoted by $\mathbf{\Gamma}_i$ and the controllability matrix denoted by $\mathbf{\Delta}_i$ are explicitly given by the following matrix equations:

$$\mathbf{\Gamma}_i = \begin{bmatrix} \mathbf{C} \\ \mathbf{C}\mathbf{A}_d \\ \mathbf{C}\mathbf{A}_d^2 \\ \vdots \\ \mathbf{C}\mathbf{A}_d^{i-1} \end{bmatrix} \tag{2.32}$$

and

$$\mathbf{\Delta}_i = \begin{bmatrix} \mathbf{A}_d^{i-1}\mathbf{B}_d & \mathbf{A}_d^{i-2}\mathbf{B}_d & \cdots & \mathbf{A}_d\mathbf{B}_d & \mathbf{B}_d \end{bmatrix} \tag{2.33}$$

The triangular Toeplitz matrix $\mathbf{H}_i$ can be assembled as follows:

$$\mathbf{H}_i = \begin{bmatrix} \mathbf{D} & \mathbf{O} & \mathbf{O} & \dots & \mathbf{O} \\ \mathbf{C}\mathbf{B}_d & \mathbf{D} & \mathbf{O} & \dots & \mathbf{O} \\ \mathbf{C}\mathbf{A}_d\mathbf{B}_d & \mathbf{C}\mathbf{B}_d & \mathbf{D} & \dots & \mathbf{O} \\ \vdots & \vdots & \vdots & \ddots & \vdots \\ \mathbf{C}\mathbf{A}_d^{i-2}\mathbf{B}_d & \mathbf{C}\mathbf{A}_d^{i-3}\mathbf{B}_d & \mathbf{C}\mathbf{A}_d^{i-4}\mathbf{B}_d & \dots & \mathbf{D} \end{bmatrix} \tag{2.34}$$

where $\mathbf{O}$ represents a zero matrix with proper dimensions. The matrix of future states denoted with $\mathbf{Z}_f$ can be rewritten with the matrix of past inputs denoted by $\mathbf{U}_p$ and the matrix of past outputs denoted by $\mathbf{Y}_p$. For this purpose, one can write:

$$\begin{aligned} \mathbf{Z}_f &= \mathbf{A}_d^i\mathbf{Z}_p + \mathbf{\Delta}_i\mathbf{U}_p \\ &= \mathbf{A}_d^i\left(\mathbf{\Gamma}_i^+\mathbf{Y}_p - \mathbf{\Gamma}_i^+\mathbf{H}_i\mathbf{U}_p\right) + \mathbf{\Delta}_i\mathbf{U}_p \\ &= \left(\mathbf{\Delta}_i - \mathbf{A}_d^i\mathbf{\Gamma}_i^+\mathbf{H}_i\right)\mathbf{U}_p + \mathbf{A}_d^i\mathbf{\Gamma}_i^+\mathbf{Y}_p \\ &= \mathbf{L}_p\mathbf{W}_p \end{aligned} \tag{2.35}$$

where the matrix $\mathbf{\Gamma}_i^+$ denotes the Moore-Penrose pseudo-inverse matrix of $\mathbf{\Gamma}_i$. The matrix $\mathbf{L}_p$ with dimensions $n_z \times i(n_u + n_y)$ and the matrix $\mathbf{W}_p$ having dimensions $i(n_u + n_y) \times j$ are respectively defined as follows:

$$\mathbf{L}_p = \begin{bmatrix} \mathbf{\Delta}_i - \mathbf{A}_d^i\mathbf{\Gamma}_i^+\mathbf{H}_i & \mathbf{A}_d^i\mathbf{\Gamma}_i^+ \end{bmatrix}, \ \mathbf{W}_p = \begin{bmatrix} \mathbf{U}_p \\ \mathbf{Y}_p \end{bmatrix} \tag{2.36}$$

The matrix of future outputs $\mathbf{Y}_f$ can be rewritten with an organized version of the future state matrix $\mathbf{Z}_f$ as follows:

$$\mathbf{Y}_f = \mathbf{\Gamma}_i \mathbf{Z}_f + \mathbf{H}_i \mathbf{U}_f = \mathbf{\Gamma}_i \mathbf{L}_p \mathbf{W}_p + \mathbf{H}_i \mathbf{U}_f \tag{2.37}$$

Define the projection matrix onto the set of future inputs denoted by $\mathbf{\Pi}_{\mathbf{U}_f^\perp}$ having dimensions $j \times j$ as:

$$\mathbf{\Pi}_{\mathbf{U}_f^\perp} = \mathbf{I} - \mathbf{U}_f^T \left(\mathbf{U}_f \mathbf{U}_f^T \right)^+ \mathbf{U}_f \tag{2.38}$$

By post-multiplying the matrix of future output $\mathbf{Y}_f$ with the projection matrix onto the set of future inputs $\mathbf{\Pi}_{\mathbf{U}_f^\perp}$, the following two matrix equations are obtained:

$$\mathbf{Y}_f \mathbf{\Pi}_{\mathbf{U}_f^\perp} = \mathbf{\Gamma}_i \mathbf{L}_p \mathbf{W}_p \mathbf{\Pi}_{\mathbf{U}_f^\perp}, \quad \mathbf{H}_i \mathbf{U}_f \mathbf{\Pi}_{\mathbf{U}_f^\perp} = \mathbf{O} \tag{2.39}$$

For simplicity, define the following matrix of dimensions $j \times j$ denoted with $\bar{\mathbf{W}}_p$ and given by:

$$\bar{\mathbf{W}}_p = \left(\mathbf{W}_p \mathbf{\Pi}_{\mathbf{U}_f^\perp} \right)^+ \mathbf{W}_p \tag{2.40}$$

The post-multiplication of Equation (2.39) by the matrix $\bar{\mathbf{W}}_p$ can be written as follows:

$$\mathbf{Y}_f \mathbf{\Pi}_{\mathbf{U}_f^\perp} \bar{\mathbf{W}}_p = \mathbf{\Gamma}_i \mathbf{L}_p \mathbf{W}_p \mathbf{\Pi}_{\mathbf{U}_f^\perp} \bar{\mathbf{W}}_p \tag{2.41}$$

Consequently, the following matrix equations can be deduced:

$$\mathbf{O}_i = \mathbf{Y}_f \mathbf{\Pi}_{\mathbf{U}_f^\perp} \bar{\mathbf{W}}_p = \mathbf{Y}_f \mathbf{\Pi}_{\mathbf{U}_f^\perp} \left(\mathbf{W}_p \mathbf{\Pi}_{\mathbf{U}_f^\perp} \right)^+ \mathbf{W}_p \tag{2.42}$$

and

$$\mathbf{O}_i = \mathbf{\Gamma}_i \mathbf{L}_p \mathbf{W}_p = \mathbf{\Gamma}_i \mathbf{Z}_f \tag{2.43}$$

Finally, a fundamental matrix equation is obtained as follows:

$$\mathbf{O}_i = \mathbf{\Gamma}_i \mathbf{Z}_f \tag{2.44}$$

where the matrix $\mathbf{O}_i$ is a rectangular matrix with dimensions $in_y \times j$. The fundamental matrix $\mathbf{O}_i$ can be post-processed with the weighting matrices $\mathbf{W}_1$ of dimensions $in_y \times j$ and $\mathbf{W}_2$ of dimensions $j \times j$ as follows:

$$\bar{\mathbf{O}}_i = \mathbf{W}_1 \mathbf{O}_i \mathbf{W}_2 \tag{2.45}$$

where the matrix $\bar{\mathbf{O}}_i$ with dimensions $in_y \times j$ defines the post-processed version of the matrix denoted by $\mathbf{O}_i$. The specific definition of the weight matrices indicated as $\mathbf{W}_1$ and $\mathbf{W}_2$ significantly affects the success of the estimated model, as well as of the identification process when using the N4SID approach. There are various types of weighting matrices, such as the Multivariable Output-Error State sPace (MOESP) method and the Canonical Variate Analysis (CVA) method. In this paper, the weight matrices $\mathbf{W}_1$ and $\mathbf{W}_2$ are determined according to the CVA technique as follows:

$$\begin{cases} \mathbf{W}_1 = E[(\mathbf{Y}_f \mathbf{\Pi}_{\mathbf{U}_f^\perp})(\mathbf{Y}_f \mathbf{\Pi}_{\mathbf{U}_f^\perp})^T])^{-1/2} \\ \mathbf{W}_2 = \mathbf{\Pi}_{\mathbf{U}_f^\perp} \end{cases} \tag{2.46}$$

where $E[x]$ identifies the expected value of the variable x. The post-processed matrix $\bar{\mathbf{O}}_i$ can be partitioned by a Singular Value Decomposition (SVD) to yield:

$$\bar{\mathbf{O}}_i = \mathbf{U} \mathbf{\Sigma} \mathbf{V}^T \tag{2.47}$$

where the matrix $\mathbf{\Sigma}$ with dimensions $in_y \times j$ consists of the singular value of the post-processed matrix indicated by $\bar{\mathbf{O}}_i$, while the orthogonal matrix $\mathbf{U}$ with dimensions $in_y \times in_y$ and the orthogonal matrix $\mathbf{V}$ with dimensions $j \times j$ are square matrices obtained using the singular value decomposition. As a result, the post-processed matrix $\bar{\mathbf{O}}_i$ can be written as follows:

$$\bar{\mathbf{O}}_i = \mathbf{U}_1 \mathbf{\Sigma}_1 \mathbf{V}_1^T \tag{2.48}$$

where:

$$\mathbf{U} = \begin{bmatrix} \mathbf{U}_1 & \mathbf{U}_2 \end{bmatrix}, \quad \mathbf{\Sigma} = \begin{bmatrix} \mathbf{\Sigma}_1 & \mathbf{O} \\ \mathbf{O} & \mathbf{O} \end{bmatrix}, \quad \mathbf{V}^T = \begin{bmatrix} \mathbf{V}_1^T \\ \mathbf{V}_2^T \end{bmatrix} \tag{2.49}$$

where the matrix $\mathbf{U}_1$ with dimensions $in_y \times \hat{n}_z$, the matrix $\mathbf{U}_2$ with dimensions $in_y \times \left(in_y - \hat{n}_z\right)$, the matrix $\mathbf{V}_1$ with dimensions $j \times \hat{n}_z$, and the matrix $\mathbf{V}_2$ with dimensions $j \times (j - \hat{n}_z)$ represent submatrices of $\mathbf{U}$ and $\mathbf{V}$, which are obtained from the singular value decomposition of the post-processed matrix $\bar{\mathbf{O}}_i$. Additionally, the matrix $\mathbf{\Sigma}_1$ having dimensions $\hat{n}_z \times \hat{n}_z$ is a square diagonal matrix given as:

$$\mathbf{\Sigma}_1 = \text{diag}(\sigma_1, \sigma_2, ..., \sigma_{\hat{n}_z}) \tag{2.50}$$

where $\hat{n}_z$ is the number of nonzero singular values indicated with σ_h, $h = 1, 2, ..., \hat{n}_z$ and represents the dimensions of the estimated state-space model. At this stage, the fundamental matrix denoted by $\mathbf{O}_i$ can be written with the weighting matrices as follows:

$$\mathbf{O}_i = \mathbf{W}_1^{-1} \mathbf{U}_1 \mathbf{\Sigma}_1 \mathbf{V}_1^T \mathbf{W}_2^{-1} = \mathbf{\Gamma}_i \mathbf{Z}_f \tag{2.51}$$

The equation can be partitioned into two parts as follows:

$$\begin{cases} \mathbf{\Gamma}_i = \mathbf{W}_1^{-1}\mathbf{U}_1\mathbf{\Sigma}_1^{1/2}\,\mathbf{T} \\ \mathbf{Z}_f = \mathbf{T}^{-1}\mathbf{\Sigma}_1^{1/2}\,\mathbf{V}_1^T\mathbf{W}_2^{-1} \end{cases} \tag{2.52}$$

where $\mathbf{T}$ denotes a similarity transformation matrix having dimensions $\hat{n}_z \times \hat{n}_z$ which is an appropriate non-singular square matrix. The similarity transformation matrix $\mathbf{T}$ can also be assumed as the identity matrix to simplify the mathematical manipulations. By using these assumptions, the equations can be written as follows:

$$\begin{cases} \mathbf{Z}_f = \mathbf{\Sigma}_1^{1/2}\,\mathbf{V}_1^T\mathbf{W}_2^{-1} \\ \mathbf{\Gamma}_i = \mathbf{W}_1^{-1}\mathbf{U}_1\mathbf{\Sigma}_1^{1/2} \end{cases} \tag{2.53}$$

The last step of the N4SID method is the extraction of discrete-time state-space matrices denoted by $\mathbf{A}_d$, $\mathbf{B}_d$, $\mathbf{C}$, and $\mathbf{D}$ from Equation (2.53). Firstly, the discrete-time matrix $\hat{\mathbf{C}}$, which is the identified output influence matrix, can be calculated with the first n_y rows of the Toeplitz matrix $\mathbf{\Gamma}_i$ as follows:

$$\hat{\mathbf{C}} = \mathbf{E}_{n_y}^T\mathbf{\Gamma}_i \tag{2.54}$$

where $\mathbf{E}_{n_y}$ represents a proper Boolean matrix. The identified discrete-time state matrix indicated with $\hat{\mathbf{A}}_d$ can be calculated as:

$$\hat{\mathbf{A}}_d = \left(\underline{\mathbf{\Gamma}_i}\right)^{+}\overline{\mathbf{\Gamma}_i} \tag{2.55}$$

where the matrix $\left(\underline{\mathbf{\Gamma}_i}\right)^{+}$ represents the Moore-Penrose pseudo-inverse matrix of the matrix $\underline{\mathbf{\Gamma}_i}$, while the matrix $\underline{\mathbf{\Gamma}_i}$ with dimensions $(i-1)n_y \times n_z$ and the matrix $\overline{\mathbf{\Gamma}_i}$ with dimensions $(i-1)n_y \times n_z$ represent the modified versions of the Toeplitz matrix $\mathbf{\Gamma}_i$, in which the last matrix block and the first matrix block with dimensions $n_y \times n_z$ are removed, respectively. The modified versions of the Toeplitz matrix can be assembled as follows:

$$\underline{\boldsymbol{\Gamma}_i} = \begin{bmatrix} \mathbf{C} \\ \mathbf{C}\mathbf{A}_d \\ \mathbf{C}\mathbf{A}_d^2 \\ \vdots \\ \mathbf{C}\mathbf{A}_d^{i-2} \end{bmatrix}, \quad \overline{\boldsymbol{\Gamma}_i} = \begin{bmatrix} \mathbf{C}\mathbf{A}_d \\ \mathbf{C}\mathbf{A}_d^2 \\ \mathbf{C}\mathbf{A}_d^3 \\ \vdots \\ \mathbf{C}\mathbf{A}_d^{i-1} \end{bmatrix} \tag{2.56}$$

To estimate the identified discrete-time input influence matrix $\hat{\mathbf{B}}_d$ and the identified direct transmission matrix $\hat{\mathbf{D}}$, the matrix of the future output $\mathbf{Y}_f$ is multiplied by the matrices $\mathbf{U}_f^+$ and $\boldsymbol{\Gamma}_i^\perp$ as follows:

$$\boldsymbol{\Gamma}_i^\perp \mathbf{Y}_f \mathbf{U}_f^+ = \boldsymbol{\Gamma}_i^\perp \boldsymbol{\Gamma}_i \mathbf{Z}_f \mathbf{U}_f^+ + \boldsymbol{\Gamma}_i^\perp \mathbf{H}_i \mathbf{U}_f \mathbf{U}_f^+ = \boldsymbol{\Gamma}_i^\perp \mathbf{H}_i \tag{2.57}$$

where the matrix $\mathbf{U}_f^+$ denotes the Moore-Penrose pseudo-inverse of the matrix of future inputs denoted with $\mathbf{U}_f$, while $\boldsymbol{\Gamma}_i^\perp$ represents the projection matrix associated with the observability matrix $\boldsymbol{\Gamma}_i$ which is a full rank matrix. To simplify the final equations, the following mathematical manipulations can used:

$$\mathbf{N} = \boldsymbol{\Gamma}_i^\perp \mathbf{Y}_f \mathbf{U}_f^+, \quad \mathbf{P} = \boldsymbol{\Gamma}_i^\perp \tag{2.58}$$

where the matrix $\mathbf{N}$ with dimensions $n_z \times in_u$ and the matrix $\mathbf{P}$ with dimensions $n_z \times in_y$ are appropriate rectangular matrices. By using the previous matrix factorizations and the simplifications given by Equation (2.58), Equation (2.57) can be rewritten as follows:

$$\mathbf{N} = \mathbf{P}\mathbf{H}_i \tag{2.59}$$

After that, the Equation (2.59) can be expanded as follows:

$$\begin{bmatrix} \mathbf{N}_1 & \mathbf{N}_2 & \dots & \mathbf{N}_i \end{bmatrix} = \begin{bmatrix} \mathbf{P}_1 & \mathbf{P}_2 & \dots & \mathbf{P}_i \end{bmatrix} \mathbf{H}_i \tag{2.60}$$

Thus, Equation (2.60) can be rewritten as follows:

$$\begin{bmatrix} \mathbf{N}_1 \\ \mathbf{N}_2 \\ \vdots \\ \mathbf{N}_i \end{bmatrix} = \begin{bmatrix} \mathbf{P}_1 & \mathbf{P}_2 & \dots & \mathbf{P}_i \\ \mathbf{P}_2 & \mathbf{P}_3 & \dots & \mathbf{O} \\ \vdots & \vdots & \ddots & \vdots \\ \mathbf{P}_i & \mathbf{O} & \dots & \mathbf{O} \end{bmatrix} \begin{bmatrix} \mathbf{I} & \mathbf{O} \\ \mathbf{O} & \underline{\mathbf{\Gamma}}_i \end{bmatrix} \mathbf{\Omega} \tag{2.61}$$

where the matrix $\mathbf{\Omega}$ with dimensions $\left(n_z + n_y\right) \times n_u$ is a rectangular matrix consisting of the identified version of the matrices $\mathbf{B}_d$ and $\mathbf{D}$. This matrix is defined as:

$$\mathbf{\Omega} = \begin{bmatrix} \mathbf{D} \\ \mathbf{B}_d \end{bmatrix} \tag{2.62}$$

Therefore, one obtains the following matrix equation:

$$\mathbf{\Omega} = \begin{bmatrix} \mathbf{I} & \mathbf{O} \\ \mathbf{O} & \underline{\mathbf{\Gamma}}_i \end{bmatrix}^{+} \begin{bmatrix} \mathbf{P}_1 & \mathbf{P}_2 & \dots & \mathbf{P}_i \\ \mathbf{P}_2 & \mathbf{P}_3 & \dots & \mathbf{O} \\ \vdots & \vdots & \ddots & \vdots \\ \mathbf{P}_i & \mathbf{O} & \dots & \mathbf{O} \end{bmatrix}^{+} \begin{bmatrix} \mathbf{N}_1 \\ \mathbf{N}_2 \\ \vdots \\ \mathbf{N}_i \end{bmatrix} \tag{2.63}$$

where the plus superscript symbol indicates the Moore-Penrose pseudo-inverse matrix. Finally, the identified discrete-time input influence matrix $\hat{\mathbf{B}}_d$ and the identified discrete-time direct transmission matrix $\hat{\mathbf{D}}$ are determined as follows:

$$\hat{\mathbf{D}} = \mathbf{E}_{n_y}^T \mathbf{\Omega}, \quad \hat{\mathbf{B}}_d = \mathbf{E}_{n_z}^T \mathbf{\Omega} \tag{2.64}$$

where $\mathbf{E}_{n_y}$ is a proper Boolean matrix that is used to obtain the matrix $\hat{\mathbf{D}}$ from the first n_y rows of the matrix $\mathbf{\Omega}$, while $\mathbf{E}_{n_z}$ is a proper Boolean matrix that is used to

obtain the matrix $\hat{\mathbf{B}}_d$ from the last n_z rows of the matrix $\boldsymbol{\Omega}$. The identified discrete-time state-space matrices can be written as:

$$\begin{cases} \hat{\mathbf{A}}_d = \left(\underline{\boldsymbol{\Gamma}_i}\right)^{+} \overline{\boldsymbol{\Gamma}_i} \\ \hat{\mathbf{B}}_d = \mathbf{E}_{n_z}^T \boldsymbol{\Omega} \\ \hat{\mathbf{C}} = \mathbf{E}_{n_y}^T \boldsymbol{\Gamma}_i \\ \hat{\mathbf{D}} = \mathbf{E}_{n_y}^T \boldsymbol{\Omega} \end{cases} \tag{2.65}$$

where $\hat{\mathbf{A}}_d$, $\hat{\mathbf{B}}_d$, $\hat{\mathbf{C}}$, and $\hat{\mathbf{D}}$ denote the identified discrete-time state matrix of dimensions $\hat{n}_z \times \hat{n}_z$, the identified discrete-time input influence matrix with dimensions $\hat{n}_z \times \hat{n}_u$, the identified output influence matrix with dimensions $\hat{n}_y \times \hat{n}_u$, and the identified direct transmission matrix with dimensions $\hat{n}_y \times \hat{n}_u$ obtained with the use of the N4SID method, respectively.

CHAPTER THREE
ANALYSIS OF LUMPED PARAMETER MECHANICAL SYSTEM

3.1 Introduction

In this chapter, the modeling of a four-dof system is studied with the CTSI method. The mechanical system is described as a lumped mass-spring-damping system. Firstly, the analytic solution of the mechanical system is studied. The equation of motion of the mechanical system is obtained using the Laplace transform. For the purpose obtain simulation signals of the system, an FE model of the mechanical system is created in ANSYS/APDL program. Displacement signals for the four masses are obtained for both step and impulse inputs. Subsequently, mathematical models of the system are identified using the obtained input and output signals. The CTSI method is utilized to obtain four transfer functions of the system. Finally, the identified vibration responses are compared to the numerical vibration responses.

3.2 Analytical Solution

In this subsection, the analytic solution of the four-dof system is described indeed. The mechanical system used in this thesis is shown in Figure 3.1.

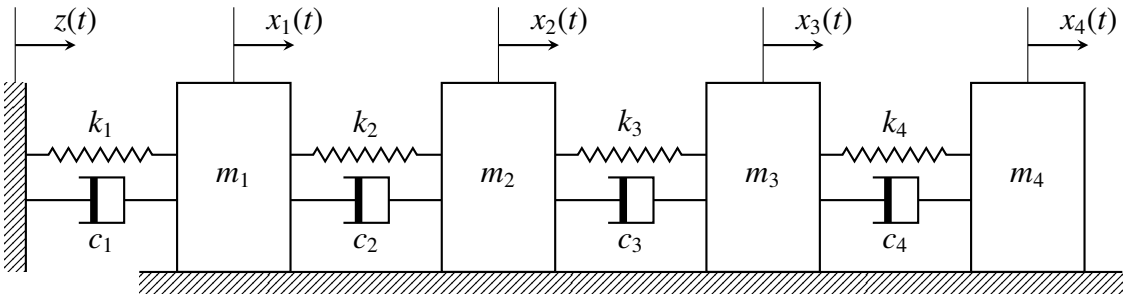


Figure 3.1 Four-dof mass-damper-spring system

In Figure 3.1, the parameters m_1, m_2, m_3, m_4 present the mass constants, the parameters c_1, c_2, c_3, c_4 denote the damper constants and k_1, k_2, k_3, k_4 represent the spring constants, respectively. The values of the system parameters are selected as $m_1 = m_2 = m_3 = m_4 = 1$ kg, $c_1 = 1.5$ Ns/m, $c_2 = 1.2$ Ns/m, $c_3 = c_4 = 0.8$ Ns/m, $k_1 = 600$ N/m, $k_2 = 400$ N/m, $k_3 = k_4 = 200$ N/m, respectively (Yavuz et al., 2016a). The displacements of the masses of the considered mechanical system are denoted with $x_1(t)$, $x_2(t)$, $x_3(t)$ and $x_4(t)$, whereas the base excitation as the input of the system is denoted with $z(t)$.

The matrix form of the equation of motion of the mechanical system is defined as follows:

$$\mathbf{M}\ddot{x}(t) + \mathbf{C}\dot{x}(t) + \mathbf{K}x(t) = c_1\dot{z}(t) + k_1 z(t) \tag{3.1}$$

where $\mathbf{M}$ denotes the mass matrix of the mechanical system with dimensions 4×4, $\mathbf{C}$ denotes the damping matrix with dimensions 4×4, whereas $\mathbf{K}$ represents the spring matrix with dimensions 4×4. The displacement of the point mass of the considered mechanical system is denoted with $x(t)$, the velocity of the point mass is denoted with $\dot{x}(t)$, and the acceleration of the point mass is denoted with $\ddot{x}(t)$.

The mass, damping, and spring matrices of the mechanical systems are calculated with Newton's laws as follows:

$$\mathbf{M} = \begin{bmatrix} m_1 & 0 & 0 & 0 \\ 0 & m_2 & 0 & 0 \\ 0 & 0 & m_3 & 0 \\ 0 & 0 & 0 & m_4 \end{bmatrix},$$

$$\mathbf{C} = \begin{bmatrix} c_1 + c_2 & -c_2 & 0 & 0 \\ -c_2 & c_2 + c_3 & -c_3 & 0 \\ 0 & -c_3 & c_3 + c_4 & -c_4 \\ 0 & 0 & -c_4 & c_4 \end{bmatrix}, \tag{3.2}$$

$$\mathbf{K} = \begin{bmatrix} k_1 + k_2 & -k_2 & 0 & 0 \\ -k_2 & k_2 + k_3 & -k_3 & 0 \\ 0 & -k_3 & k_3 + k_4 & -k_4 \\ 0 & 0 & -k_4 & k_4 \end{bmatrix}$$

The following eigenvalue equation is used to obtain undamped natural frequencies of the mechanical system denoted as ω.

$$|-\omega^2\mathbf{M} + \mathbf{K}| = 0 \tag{3.3}$$

The eigenvalue equation can be written as follows:

$$\begin{vmatrix} 1000 - \omega^2 & -400 & 0 & 0 \\ -400 & 600 - \omega^2 & -200 & 0 \\ 0 & -200 & 400 - \omega^2 & -200 \\ 0 & 0 & -200 & 200 - \omega^2 \end{vmatrix} \begin{Bmatrix} x_1(t) \\ x_2(t) \\ x_3(t) \\ x_4(t) \end{Bmatrix} = \begin{Bmatrix} 0 \\ 0 \\ 0 \\ 0 \end{Bmatrix} \tag{3.4}$$

$$\omega^8 - 2200\omega^6 + 1400000\omega^4 - 280000000\omega^2 + 9600000000 = 0 \tag{3.5}$$

The undamped natural frequencies of the mechanical system are calculated as follows:

$$f_{n1} = 1.042\ Hz, \quad f_{n2} = 2.738\ Hz, \quad f_{n3} = 3.899\ Hz, \quad f_{n4} = 5.652\ Hz \tag{3.6}$$

Transfer functions of the mechanical system are found with the Laplace transform method. The results are obtained by using $\mathbf{X}(s) = \mathbf{H}(s)\mathbf{Z}(s)$. $\mathbf{H}(s)$ represents the transfer function matrix with dimensions 4×4, whereas $\mathbf{X}(s)$ and $\mathbf{Z}(s)$ present the Laplace transforms of the displacements denoted with $\mathbf{x}(t)$ and base excitation denoted with $\mathbf{z}(t)$. The transfer function matrix is given as follows:

$$\mathbf{H}(s) = [s^2\mathbf{M} + s\mathbf{C} + \mathbf{K}]^{-1} \tag{3.7}$$

$H_{i,j}$ presents the element of ith row and jth column of the matrix $\mathbf{H}(s)$. The transfer functions for the displacements are given as follows:

$$\begin{aligned}
H_{11}(s) &= \frac{250s^6 + 1100s^5 + 301200s^4 + 660192s^3 + 9016 \times 10^4 s^2 + 4.4 \times 10^9 s + 4 \times 10^9}{D(s)} \\
H_{21}(s) &= \frac{300s^5 + 100720s^4 + 420192s^3 + 6016 \times 10^4 s^2 + 4.4 \times 10^9 s + 4 \times 10^9}{D(s)} \\
H_{31}(s) &= \frac{240s^4 + 140192s^3 + 2016 \times 10^4 s^2 + 4.4 \times 10^9 s + 4 \times 10^9}{D(s)} \\
H_{41}(s) &= \frac{192s^3 + 16 \times 10^4 s^2 + 4.4 \times 10^9 s + 4 \times 10^9}{D(s)}
\end{aligned} \tag{3.8}$$

where

$$\begin{aligned}
D(s) &= 250s^8 + 1775s^7 + 553810s^6 + 2.333 \times 10^6 s^5 + 3.524 \times 10^8 s^4 + 7.074 \times 10^8 s^3 \\
&+7.016 \times 10^{10} s^2 + 3.24 \times 10^{10} s + 2.4 \times 10^{12}
\end{aligned} \tag{3.9}$$

where $H_{11}(s)$ represents relationship between base excitation denoted with $Z(s)$ and displacement of the first mass denoted with $X_1(s)$, $H_{21}(s)$ represents relationship between $Z(s)$ and the displacement of the second mass denoted with $X_2(s)$, $H_{31}(s)$ represents relationship between $Z(s)$ and the displacement of the third mass $X_3(s)$, $H_{41}(s)$ represents relationship between $Z(s)$ and the displacement of the fourth mass denoted with $X_4(s)$, whereas $D(s)$ represents denominator of the transfer functions denoted with $H_{11}(s)$, $H_{21}(s)$, $H_{31}(s)$, and $H_{41}(s)$.

3.3 Finite Element Model

The FE model of the considered mechanical system is built by ANSYS / APDL software (ANSYS Inc., 2012) with MASS21 and COMBIN14 elements. The model is shown in Figure 3.2.



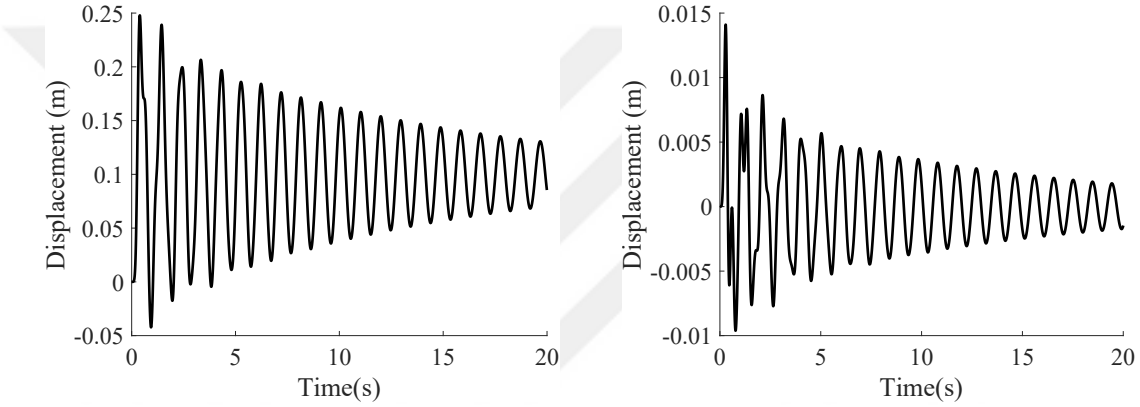
Figure 3.2 Four-dof mechanical system

In Figure 3.2, M_0 represents MASS21 elements for the each mass, whereas K_0 denotes COMBIN14 element for each set of spring and damping of the four-dof mechanical system. For the base excitation, the displacements of the masses as the output signals of the system are obtained from ANSYS/APDL.

The modal analysis is studied to obtain natural frequencies of the mechanical system in ANSYS/APDL program. The natural frequencies of the system are 1.042 Hz, 2.732 Hz, 3.8985 Hz and 5.6521 Hz. Time parameters of the transient analysis are selected according to the fourth natural frequency of the mechanical system. Time step are calculated as $dt = 1/f_{n4}/20 = 0.0088$ s and steady-state time is selected as $t_{ss} = 20$ s.

3.4 Identification of the Mechanical System

This subsection details the process of identifying the mechanical system, in which the transfer functions are obtained through the implementation of the CTSI method. To identify the transfer functions, two distinct datasets are utilized for both identification and validation datasets. Specifically, the identification dataset is generated from the FE model, applying a step input with a magnitude of 10 cm. On the other hand, the validation dataset is acquired from the FE model, implementing an impulse input with a value of 10 cm. Figure 3.3 shows $x_4(s)$ the output signals for both identification and validation datasets.



(a) (b)

Figure 3.3 Vibration responses of fourth mass (a) identification (b) validation

In the SI method, the transfer functions between input and output signals are identified. Therefore, the relationships of the transfer functions obtained by using the CTSI method can be written as follows:

$$\begin{Bmatrix} x_1(s) \\ x_2(s) \\ x_3(s) \\ x_4(s) \end{Bmatrix} = \begin{bmatrix} H_{11}(s) \\ H_{21}(s) \\ H_{31}(s) \\ H_{41}(s) \end{bmatrix} (c_1 s + k_1)\{z(s)\} = \begin{bmatrix} G_{11}(s) \\ G_{21}(s) \\ G_{31}(s) \\ G_{41}(s) \end{bmatrix} \{z(s)\} \tag{3.10}$$

where $G_{11}(s)$ represents relationship between base excitation denoted with $Z(s)$ and displacement of the first mass denoted with $X_1(s)$, $G_{21}(s)$ represents relationship between $Z(s)$ and the displacement of the second mass denoted with $X_2(s)$, $G_{31}(s)$ represents relationship between $Z(s)$ and the displacement of the third mass $X_3(s)$, $G_{41}(s)$ represents relationship

between $Z(s)$ and the displacement of the fourth mass denoted with $X_4(s)$.

The process of selecting the appropriate model order is a crucial step in the SI method. To achieve this, various criteria, such as FPE and AIC, are commonly utilized to optimize the model's complexity and goodness of fit. In the case of a mechanical system's SI process, transfer functions of the system are identified for different orders of the numerator and denominator. Subsequently, the FPE value and fit values for both the identification and validation datasets are determined for each set of orders. The FPE and fit values are listed in Table 3.1.

Table 3.1 Identification results of (a) $G_{11}(s)$ and $G_{21}(s)$ (b) $G_{31}(s)$ and $G_{41}(s)$

(a)

		$G_{11}(s)$			$G_{21}(s)$		
n	m	FPE	fit_{id}	fit_{val}	FPE	fit_{id}	fit_{val}
5	5	7.29×10^{-6}	74.64	30.96	4.99×10^{-6}	90.28	66.78
6	5	2.01×10^{-6}	86.69	73.71	2.14×10^{-6}	93.63	80.77
6	6	1.73×10^{-6}	87.65	71.65	1.72×10^{-6}	94.31	78.96
7	6	1.60×10^{-6}	88.14	77.97	1.56×10^{-6}	94.57	85.21
7	7	1.91×10^{-6}	87.05	34.19	2.11×10^{-6}	93.69	72.45
8	7	6.76×10^{-9}	99.23	96.64	4.21×10^{-10}	99.91	99.86
8	8	4.29×10^{-10}	99.81	99.86	4.20×10^{-10}	99.91	99.87

(b)

		$G_{31}(s)$			$G_{41}(s)$		
n	m	FPE	fit_{id}	fit_{val}	FPE	fit_{id}	fit_{val}
5	5	8.12×10^{-6}	93.14	75.38	1.98×10^{-6}	97.35	90.42
6	5	2.32×10^{-7}	98.84	94.81	8.66×10^{-9}	99.82	99.24
6	6	1.64×10^{-7}	99.02	94.02	6.21×10^{-9}	99.85	99.11
7	6	1.35×10^{-7}	99.12	95.29	5.23×10^{-9}	99.86	99.29
7	7	1.36×10^{-7}	99.11	94.43	5.15×10^{-9}	99.86	99.27
8	7	4.08×10^{-10}	99.95	99.89	3.94×10^{-10}	99.96	99.90
8	8	4.08×10^{-10}	99.95	99.89	3.94×10^{-10}	99.96	99.90

Table 3.1a lists the results of $G_{11}(s)$ and $G_{21}(s)$, while the results of $G_{31}(s)$ and $G_{41}(s)$ are provided in Table 3.1b. The mathematical model should be chosen for lower FPE and higher fit values with the minimum values of n and m representing the order of the mathematical model. For example, for the $G_{11}(s)$ transfer function, the FPE values decrease as the order of the mathematical model, similarly, identification and verification fit values increase. For $n = 7$, $m = 7$ and $n = 8$, $m = 7$, there is a significant variation between these values, while for

$n = 8$, $m = 7$ and $n = 8$, $m = 8$, there is a slight variation. When considering model selection within the framework of the SI method, it is generally advisable to prefer the simplest model among a set of models that fit the data equally well (Keesman, 2011). So, the estimated mathematical model can be represented by $n = 8$ and $m = 7$ for $G_{11}(s)$ transfer function. The CTSI is performed for other transfer functions. It is concluded that the numerator and denominator orders are selected as $n = 8$ and $m = 7$ for $G_{11}(s)$, $G_{21}(s)$, and $G_{31}(s)$ transfer functions, whereas the numerator and denominator orders are chosen as $n = 6$ and $m = 5$ for $G_{41}(s)$ transfer function, respectively. Since the fourth natural frequency is not dominant in $G_{41}(s)$, the transfer function is obtained to cover the first three natural frequencies. Considering that the fourth natural frequency is not predominant in $X_4(s)$, the $G_{41}(s)$ transfer function is obtained to include the first three natural frequencies.

A comparison of the vibration responses of the FE model and the identified mathematical models identified with the CTSI method is shown in Figure 3.4.

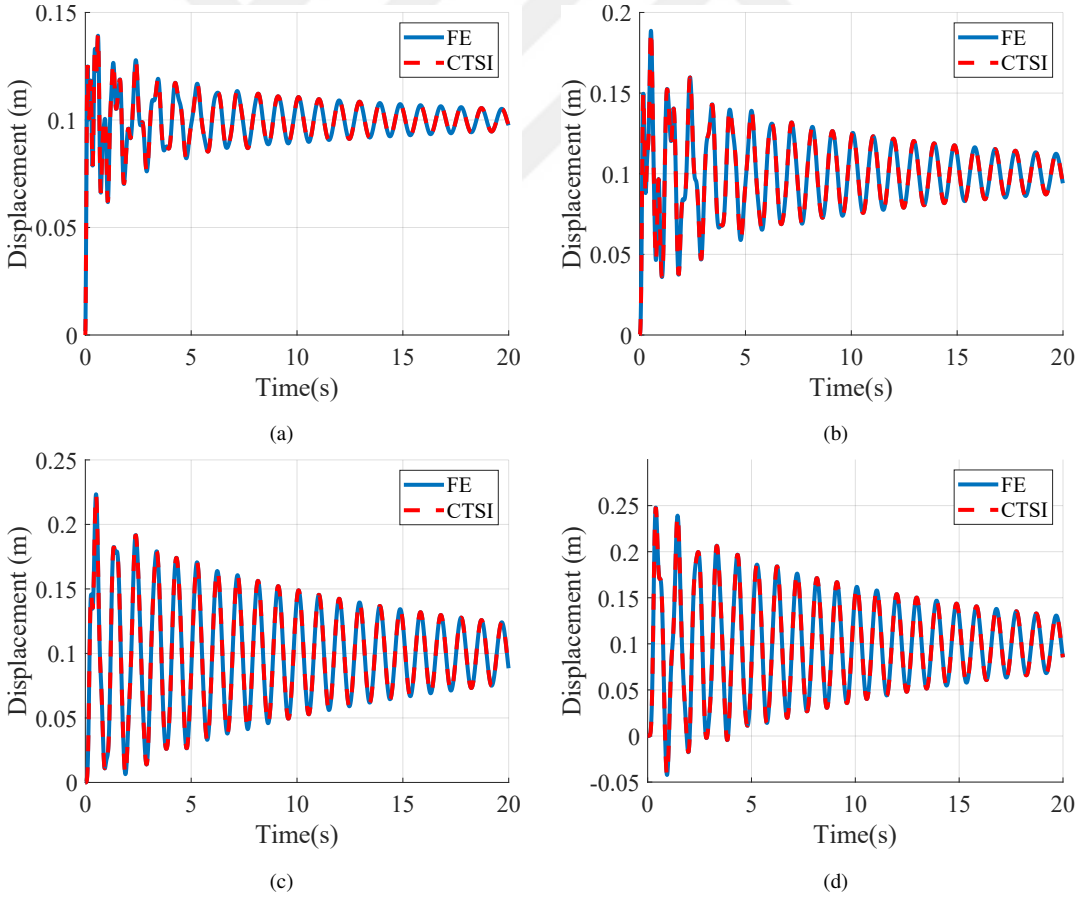


Figure 3.4 Comparison of the vibration responses (a) $G_{11}(s)$, (b) $G_{21}(s)$, (c) $G_{31}(s)$ and (d) $G_{41}(s)$ for the identification dataset

In Figures 3.4a, 3.4b, 3.4c, and 3.4d, the vibration responses of the FE model are compared with those obtained using the identified models determined with the use of the CTSI method for $G_{11}(s)$, $G_{21}(s)$, $G_{31}(s)$ and $G_{41}(s)$, respectively. By observing Figure 3.4, it is apparent that the identified vibration responses successfully match the vibration responses of the FE model for the mechanical system.

The vibration responses of the FE model and the identified mathematical models obtained with the CTSI method are shown in Figure 3.5 for the validation dataset.

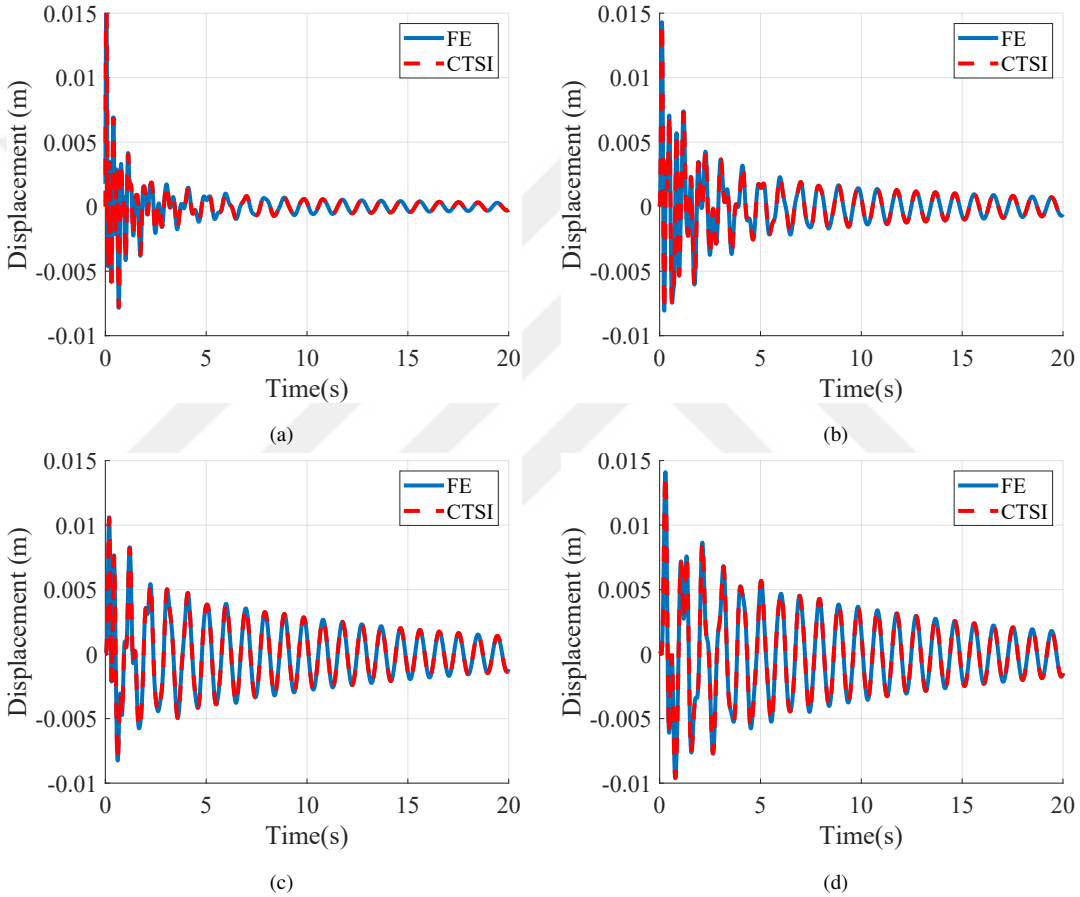


Figure 3.5 Comparison of the vibration responses (a) $G_{11}(s)$, (b) $G_{21}(s)$, (c) $G_{31}(s)$ and (d) $G_{41}(s)$ for the validation dataset

In Figures 3.5a, 3.5b, 3.5c, and 3.5d, the vibration responses of the FE model are compared with the vibration responses obtained using the identified models for $G_{11}(s)$, $G_{21}(s)$, $G_{31}(s)$ and $G_{41}(s)$, respectively, for the validation dataset. It is apparent in Figure 3.5 that the identified vibration responses and the vibration responses of the FE model successfully match for the validation dataset. The identified transfer functions are given as follows:

$$G_{11}(s) = \frac{4.268s^7 + 607.9s^6 + 7692s^5 + 7.178 \times 10^5 s^4 + 3.063 \times 10^6 s^3 + 2.112 \times 10^8 s^2 + 1.703 \times 10^8 s + 9.321 \times 10^9}{s^8 + 7.279s^7 + 2188s^6 + 9476s^5 + 1.38 \times 10^6 s^4 + 2.848 \times 10^6 s^3 + 2.731 \times 10^8 s^2 + 1.297x10^8 s + 9.321 \times 10^9} \tag{3.11}$$

$$G_{21}(s) = \frac{0.0676s^7 + 15.15s^6 + 2413s^5 + 2.496 \times 10^5 s^4 + 1.968 \times 10^6 s^3 + 1.416 \times 10^8 s^2 + 1.68 \times 10^8 s9.324 \times 10^9}{s^8 + 7.074s^7 + 2189s^6 + 9216s^5 + 1.38 \times 10^6 s^4 + 2.779 \times 10^6 s^3 + 2.731 \times 10^8 s^2 + 1.271 \times 10^8 s + 9.324 \times 10^9} \tag{3.12}$$

$$G_{31}(s) = \frac{0.001345s^7 + 0.1665s^6 + 33.93s^5 + 5556s^4 + 6.652 \times 10^5 s^3 + 4.837 \times 10^7 s^2 + 1.681 \times 10^8 s9.324 \times 10^9}{s^8 + 7.074s^7 + 2189s^6 + 9214s^5 + 1.38 \times 10^6 s^4 + 2.778 \times 10^6 s^3 + 2.731 \times 10^8 s^2 + 1.271 \times 10^8 s + 9.324 \times 10^9} \tag{3.13}$$

$$G_{41}(s) = \frac{-0.03353s^5 + 7.375s^4 - 86.44s^3 - 4860s^2 + 1.12 \times 10^5 s + 7.541 \times 10^6}{s^6 + 3.347s^5 + 937.5s^4 + 1522s^3 + 2.145 \times 10^5 s^2 + 7.954 \times 10^4 s + 7.541 \times 10^6} \tag{3.14}$$

To evaluate the performance of the identified transfer functions, the identified natural frequencies and relative errors of the identified natural frequencies are examined. The relative errors of the identified natural frequencies can be calculated by considering the corresponding numerical natural frequencies as follows:

$$\text{error } \hat{f}_{ni} = \left| \frac{\hat{f}_{ni} - f_{ni}}{f_{ni}} \right| \qquad \text{for i=1, 2, 3, 4} \tag{3.15}$$

where $\hat{f}_{ni}$, f_{ni} respectively denote the identified and numerical natural frequencies, whereas error $\hat{f}_{ni}$ represents the relative error of the identified natural frequency.

The fit values, the identified natural frequencies and errors of the natural frequencies for four transfer functions are listed in Table 3.2.

Table 3.2 Identified natural frequencies

	$G_{11}(s)$	$G_{21}(s)$	$G_{31}(s)$	$G_{41}(s)$
fit_{id} (%)	99.23	99.91	99.95	99.83
fit_{val} (%)	96.64	99.86	99.89	99.24
$\hat{f}_{n1}$ (Hz)	1.0416	1.0416	1.0416	1.0416
$\hat{f}_{n2}$ (Hz)	2.733	2.7325	2.7325	2.7327
$\hat{f}_{n3}$ (Hz)	3.8851	3.8831	3.8831	3.8893
$\hat{f}_{n4}$ (Hz)	5.6007	5.6056	5.6058	-
error $\hat{f}_{n1}$	3.54×10^{-4}	3.61×10^{-4}	3.62×10^{-4}	3.64×10^{-4}
error $\hat{f}_{n2}$	1.82×10^{-3}	2.01×10^{-3}	2.01×10^{-3}	1.94×10^{-3}
error $\hat{f}_{n3}$	3.55×10^{-3}	4.07×10^{-3}	4.09×10^{-3}	2.49×10^{-3}
error $\hat{f}_{n4}$	9.08×10^{-3}	8.20×10^{-3}	8.17×10^{-3}	-

It is shown in Table 3.2 that four natural frequencies are succesfully identified for $G_{11}(s)$, $G_{21}(s)$, $G_{31}(s)$ transfer functions, whereas first three natural frequencies are succesfully identified for $G_{41}(s)$ transfer function. The errors of first natural frequencies are calculated as 3.54×10^{-4}, 3.61×10^{-4}, 3.62×10^{-4} and 3.64×10^{-4} for $G_{11}(s)$, $G_{21}(s)$, $G_{31}(s)$ and $G_{41}(s)$ transfer functions, respectively.

In literature, the CTSI approach is utilized for time-domain and frequency-domain identification. After time-domain identification is successfully investigated, frequency-domain identification is studied for modeling. The frequency responses of the FE model and the identified mathematical models obtained from the CTSI method are shown in Figure 3.6.

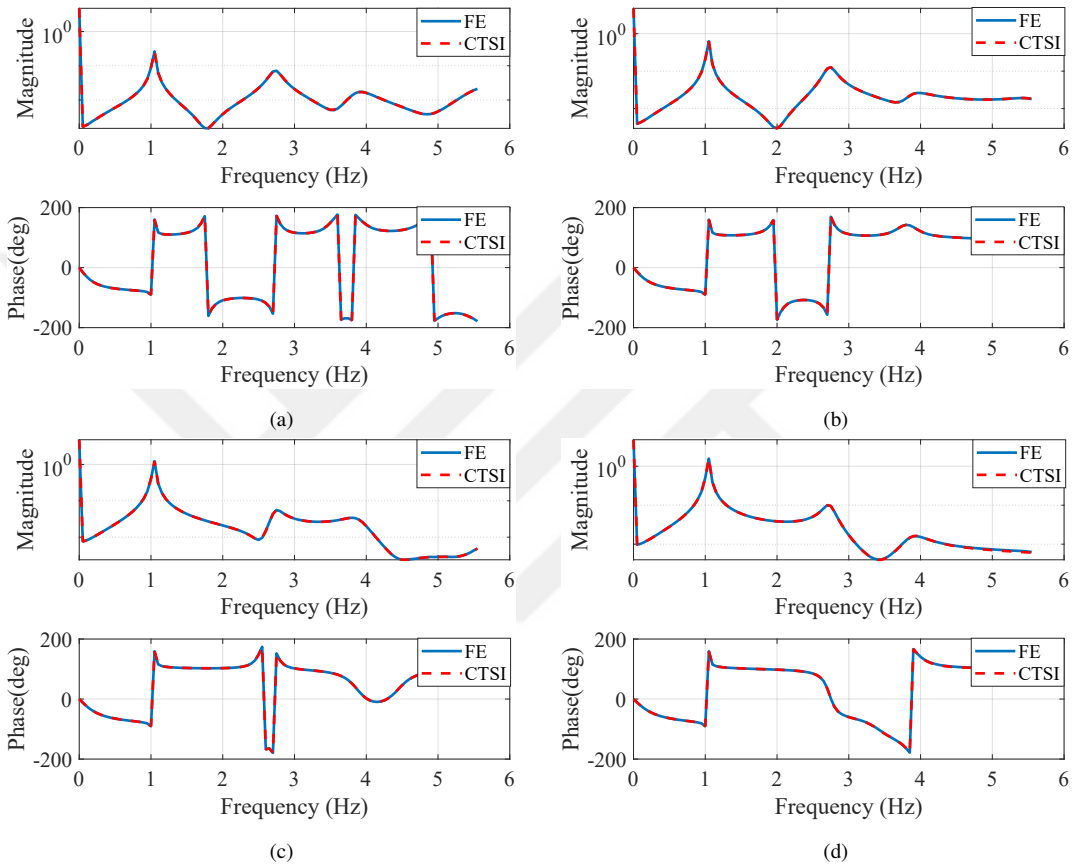


Figure 3.6 Frequency responses of (a) $G_{11}(s)$, (b) $G_{21}(s)$, (c) $G_{31}(s)$ and (d) $G_{41}(s)$ transfer functions

It is apparent in Figure 3.6 that the frequency responses of the identified mathematical models are successfully matched with the frequency responses of the FE model for all natural frequencies of the mechanical system.

CHAPTER FOUR
VIBRATION ANALYSIS OF FLEXIBLE MANIPULATORS

4.1 Introduction

This chapter provides a detailed description of an experimental system and an FE model of single-link curved manipulators used as the case study in the thesis. An experimental system is set up to synchronously drive the servo motor and measure the acceleration, displacement, and strain signals of the steel and composite manipulators. To evaluate the effectiveness and repeatability of the experimental system, the FE model of the SM is created to obtain the acceleration and displacement signals of the manipulator. A comparative analysis of the residual vibration responses obtained from the experimental system and the FE model is presented for the SM. The numerical and experimental signals of the SM are employed for vibration analysis, identification, and passive vibration control of the manipulators, while only the experimental signals are used for the composite manipulators.

4.2 Experimental System

In this subsection, the experimental system used to measure experimental input and output signals and experimental modal analysis of the steel and composite manipulators are described indeed. The experimental system is introduced to synchronously collect acceleration and displacement signals at the tip point of the single-link manipulators and strain signals at the end point of the manipulators for angular velocity input. The experimental system employed for this purpose is shown in Figure 4.1.

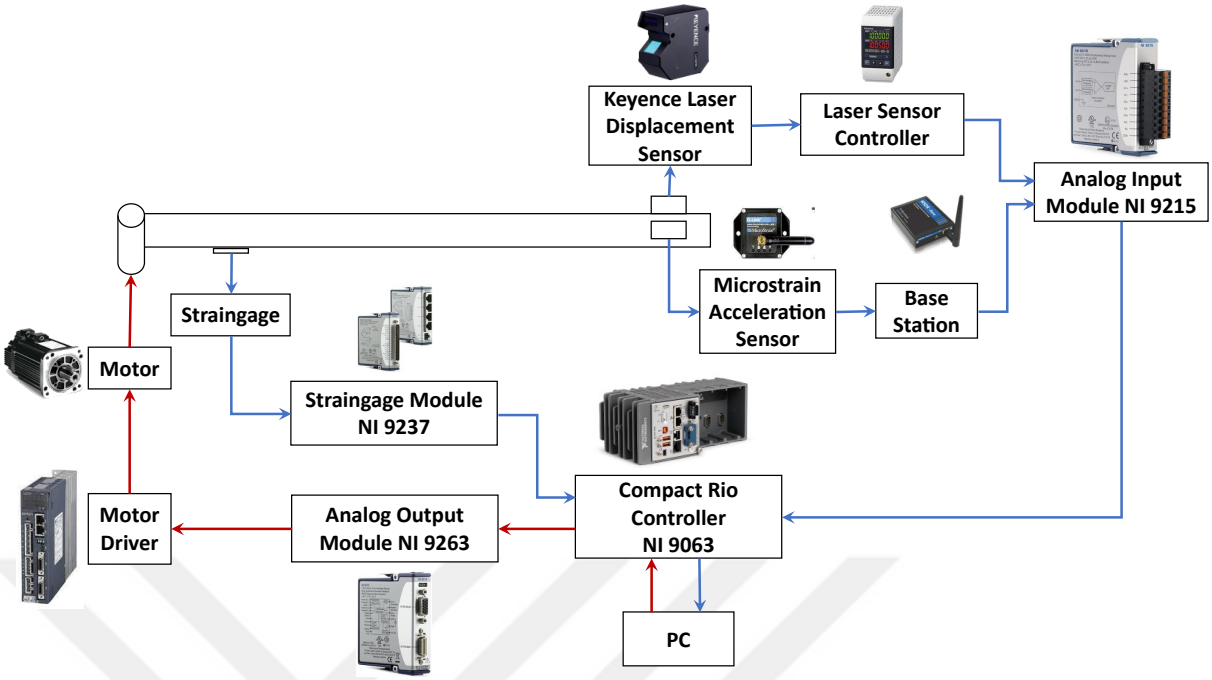


Figure 4.1 Experimental system

The experimental system with the electronic apparatus necessary for implementing the control system is shown in Figure 4.2.

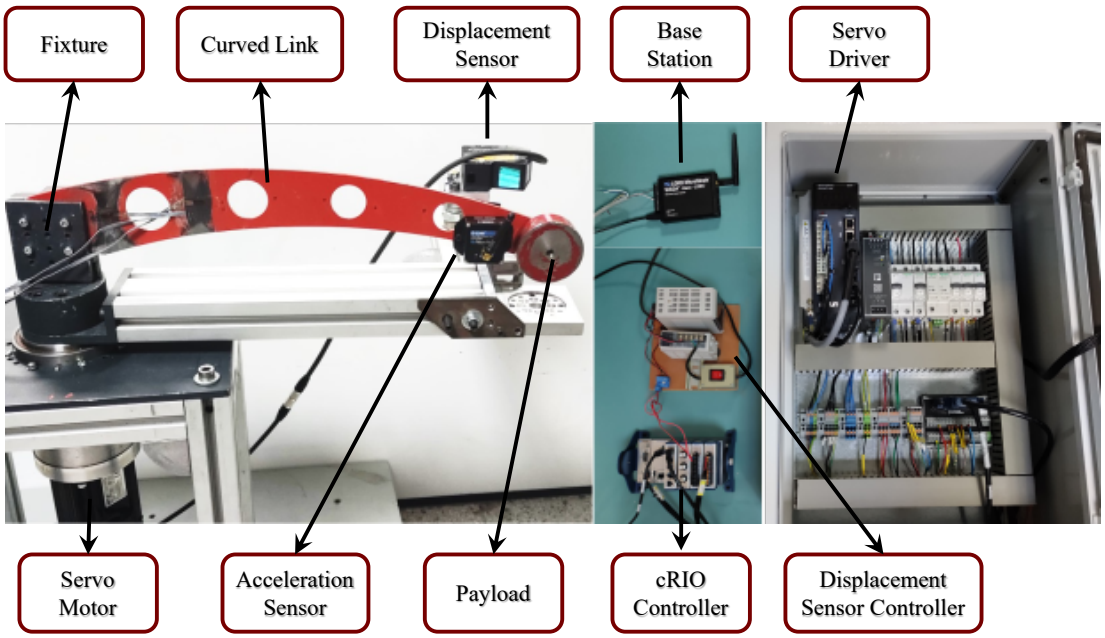


Figure 4.2 Experimental system of the flexible manipulator with electric apparatus

To synchronously drive and measure vibration signals of the flexible manipulators, a NI-CompactRIO 9063 controller is used, which is an embedded real-time controller with a reconfigurable FPGA. The NI-CompactRIO 9063 can be used with analog input and output modules. The flexible manipulator is driven with an Estun-EMJ08AFB24 servo motor with a power P_m equal to 750 W with an Estun-PR7O08AMF servo driver. A Nabtesco RV025 N-81 gear with a gearbox ratio ϵ equal to 81 is mounted to the servomotor to obtain the necessary torque for different payloads. The motion signals are transferred from the NI-CompactRIO 9063 controller to the servo driver with an NI 9263 analog output module.

The vibration signals of the manipulators can be measured as acceleration, displacement and strain with the experimental system. A microstrain wireless acceleration sensor and a microstrain base station are employed to measure the acceleration signals of the manipulator in the bending direction. The acceleration sensor is mounted at the tip of the manipulator. The base station of the acceleration sensor converts the measured acceleration signals to voltage and then these signals are transmitted to the cRIO controller via an NI 9215 voltage input module.

The displacement signals of the manipulator are measured with a Keyence LK-G157 laser displacement sensor and a Keyence controller. The sensor is capable of accurately measuring the displacement amplitudes within the range of +40 mm to -40 mm. The output of the Keyence controller takes analog voltages between +10V and -10V corresponding to measuring displacement range. The laser displacement sensor is mounted at a beam that is the same level as the acceleration sensor. The displacement signals are measured as a voltage with the Keyence controller and are transmitted to the cRIO controller via the NI 9215 voltage input module. The measured signals are converted from voltage to millimeter with K=1/4 parameter in the cRIO controller.

The strain signals are measured with a strain gauge sensor placed at the end point of the manipulator. Since the strain signals are at the maximum level at the end of the manipulator. The measured strain signals are transmitted to the cRIO controller with an NI 9949 quarter-bridge module and an NI 9237 strain module. The sampling frequency f_s of the NI 9215 module and the NI 9237 module is selected as 985 Hz. Thus, the experimental system devised for the manipulator considered as the case study of this thesis allows for recording a

proper input-output set of data suitable for the SI procedures of interest for this thesis.

LabVIEW software, which is a two-layer code given in Appendix B, is developed to control the servo motor and synchronously measure signals from acceleration, displacement, and strain sensors. In the first layer, the measured data is transmitted from FPGA to Real-time, and in the second layer, the measure signals are plotted. Besides, in the first layer, Trapezoidal and S-curve motion inputs are generated in voltage and the voltage signals are transferred from the NI 9263 module to the servo motor in the second layer.

The measured signals are filtered with a low pass filter with a cut-off frequency of 10 Hz.

In this thesis, four manipulators made of various materials are used for vibration analysis, identification and vibration control. These manipulators consist of a steel manipulator, an epoxy-glass manipulator with the orientation of [0/90] lay-up, an epoxy-glass manipulator with the orientation of [45/ − 45] lay-up and an epoxy-carbon manipulator with the orientation of [0/90] lay-up. The manipulators used in the thesis are shown in Table 4.1.

Table 4.1 Types of flexible manipulators

Manipulator	The shape of the manipulators	Material	Orientation
SM		Steel	–
EGM-a		Epoxy-Glass	[0/90]
EGM-b		Epoxy-Glass	[45/ − 45]
ECM		Epoxy-Carbon	[0/90]

In Table 4.1, SM, EGM-a, EGM-b and ECM denote a steel manipulator, an epoxy-glass manipulator with the orientation of [0/90] lay-up, an epoxy-glass manipulator with the orientation of [45/ − 45] lay-up and an epoxy-carbon manipulator with the orientation of [0/90] lay-up, respectively.

Experimental system with the SM, EGM-a, EGM-b and ECM are shown in Figures 4.3, 4.4 and 4.5.

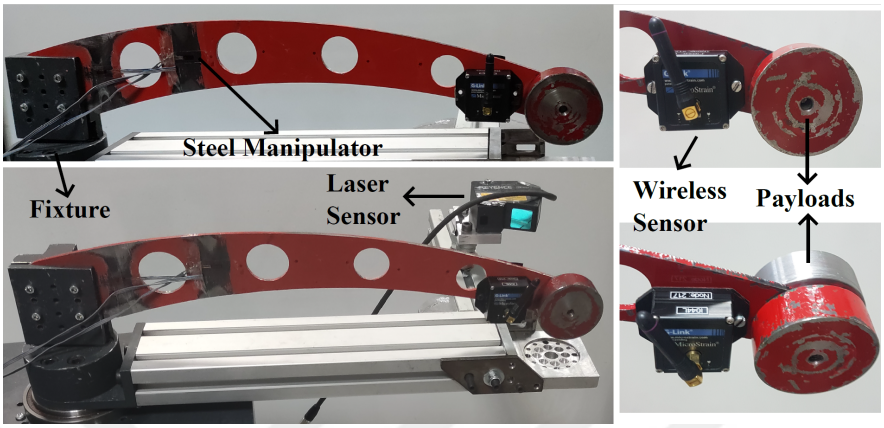


Figure 4.3 Experimental system with the SM

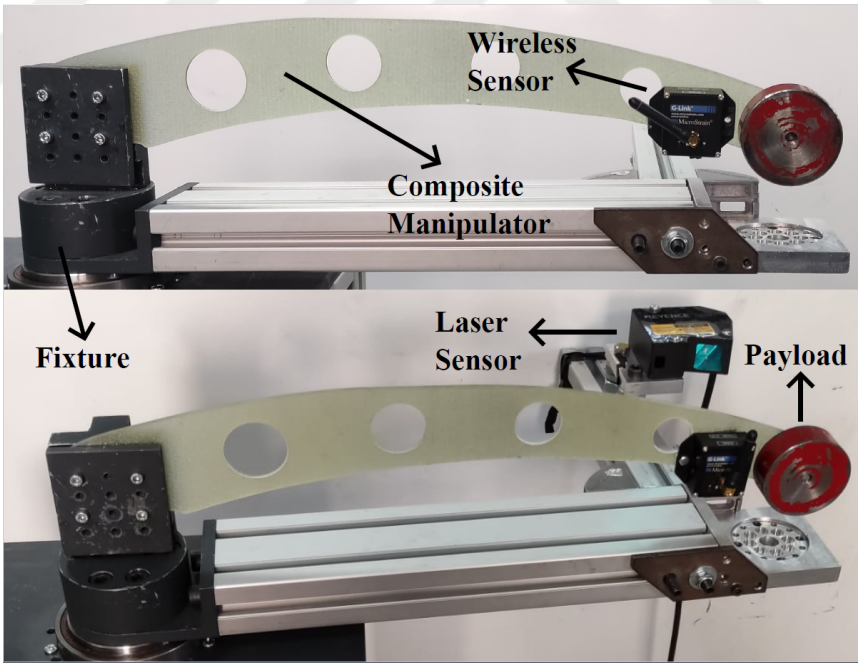


Figure 4.4 Experimental system with the EGM-a and EGM-b

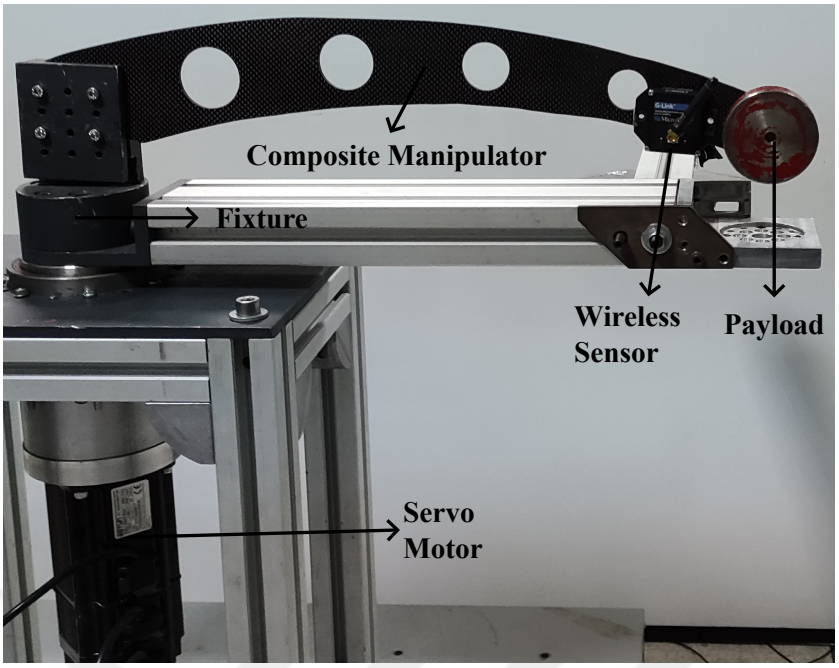


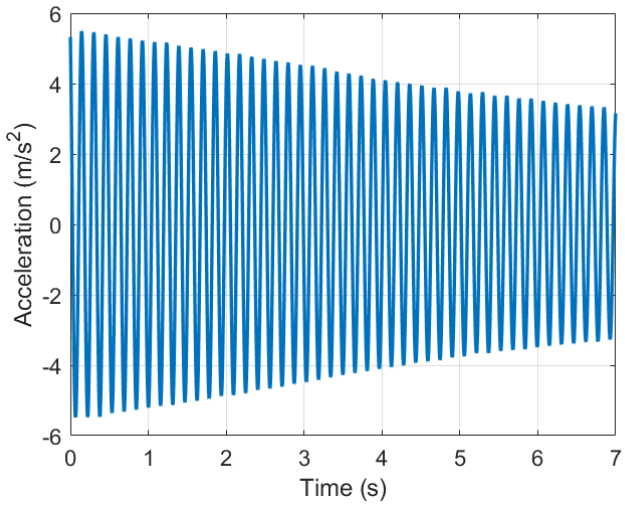
Figure 4.5 Experimental system with the ECM

The length L and the thickness W of the manipulator are 500 mm and 4 mm, respectively. An acceleration sensor and a payload are mounted at the tip point of the manipulator. The mass of the sensor m_s and the mass of the payload m_p are equal to 0.057 kg and 0.62 kg, respectively. The sensor and the payload are placed at a distance of d_s = 70 mm and d_p = 20 mm from the tip point of the manipulator, respectively.

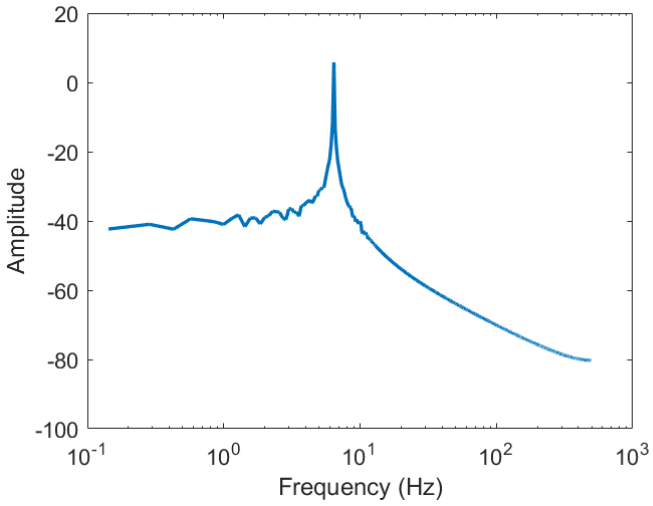
4.2.1 Experimental Modal Analysis

To experimentally obtain the first natural frequency of the manipulator, an experimental modal analysis is performed first. To this end, the time-domain and the frequency-domain responses of the SM shown in Figure 4.6 are employed.

In particular, Figure 4.6a represents the time-domain acceleration of the manipulator that is measured experimentally, while Figure 4.6b represents the corresponding frequency-domain signal calculated by using the Fast Fourier Transform (FFT). As shown in Figure 4.6b, the FFT is applied to the free vibration response of the manipulator represented in Figure 4.6a.



(a)



(b)

Figure 4.6 Free vibration response of the flexible manipulator (a) time-domain acceleration response (b) frequency-domain acceleration response

Then, the resulting frequency-domain response is used to experimentally identify the first natural frequency of the manipulator from its acceleration signal (Meirovitch, 2000, 1986). On the other hand, the damping ratio of the flexible manipulator is experimentally estimated with the use of the logarithmic decrement method (Little & Mann, 2019; Tweten et al., 2014). By using this simple and effective method, the dimensionless damping ratio of the system under study can be calculated as follows:

$$\xi_{\text{exp}} = \frac{\delta_{\text{exp}}}{\sqrt{4\pi^2 + \delta_{\text{exp}}^2}} \tag{4.1}$$

where δ_{exp} represents the logarithmic decrement obtained experimentally that is given by:

$$\delta_{\text{exp}} = \frac{1}{n} \ln\left(\left|\frac{x_1}{x_{n+1}}\right|\right) \tag{4.2}$$

where n is an integer number, x_1 represents amplitude at the first peak of the vibration response, x_n denotes the amplitude of the n-th peak of the vibration response, while ξ_{exp} represents the damping ratio of the flexible manipulator estimated experimentally. Natural frequencies and damping ratios of the steel and composite manipulators are listed in Table 4.2 calculated with the FFT and logaritmic decrement method.

Table 4.2 Natural frequencies and damping ratios of the flexible manipulators

Manipulators	m_p (kg)	f_n (Hz)	ξ
SM	0.62	6.42	0.0019
	1.24	4.86	0.0021
EGM-a	0.62	2.12	0.0027
	1.24	1.46	0.0024
EGM-b	0.62	2.28	0.0036
	1.24	1.66	0.004
ECM	0.62	3.56	0.0035
	1.24	2.6	0.0021

4.3 Finite Element Model

The SM is designed using the SOLIDWORKS program. Subsequently, the CAD model is transferred to ANSYS/APDL software for the FE analysis (ANSYS Inc., 2012). The FE model and the geometric dimensions of the manipulator are shown in Figure 4.7.

In particular, Figure 4.7a shows the dimensions of the geometric model of the manipulator, whereas Figure 4.7b shows the FE mesh constructed for the manipulator. The point O shown in Figure 4.7b represents the global origin of the FE model.

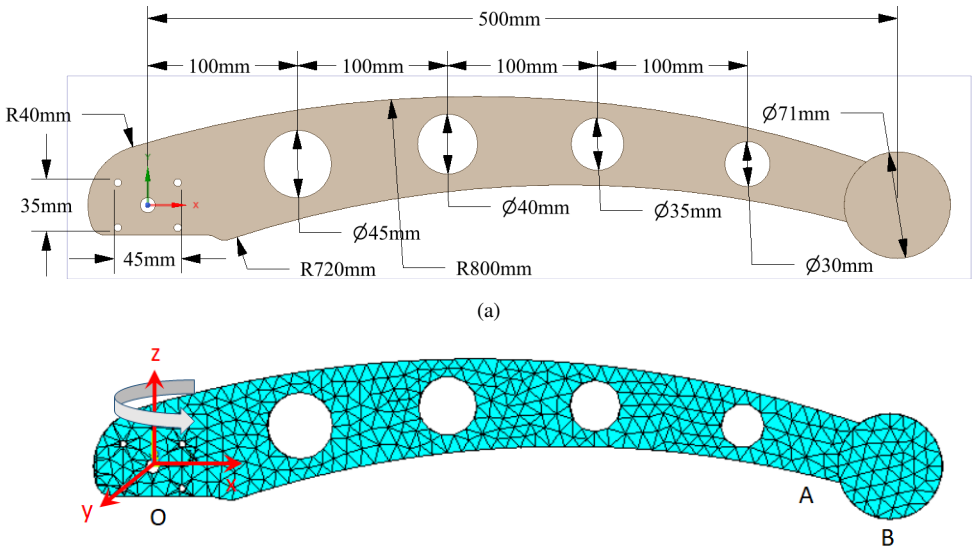


Figure 4.7 (a) Dimensions and (b) finite element model of the curved manipulator

In the experiments, the manipulator is driven by a servomotor, which is endowed with mechanical flexibility in the coupling between the motor shaft and the robotic link. Therefore, in the three-dimensional FE model, a revolute joint with a rotational spring constant denoted with k_m and equal to $1.6 \cdot 10^4$ Nm/rad is considered in the point O. Additionally, two masses are included at the tip point of the manipulator to respectively represent the sensor and the payload. The sensor is placed at the point A of the FE mesh, while the point B represents the collocation point of the payload.

The manipulator is made of steel. For performing the FE analysis of the flexible manipulator, the mass density ρ, the Young modulus E, and the Poisson ratio ν considered in the FE model are equal to 7860 kg/m^3, 210 GPa, and 0.3, respectively.

To create the FE mesh of the manipulator, three-dimensional ten-node tetrahedral elements with quadratic shape functions were used, which are suitable for modeling irregular meshes and lead to accurate numerical solutions, considering the SOLID187 element implemented in ANSYS. The mesh size s selected is equal to 10 mm. Consequently, the FE model of the manipulator was constructed by using 3236 tetrahedral elements and 6375 three-dimensional nodes, which represent a proper FE mesh leading to the convergence of the numerical results. Additionally, to include both the mass of the sensor and the mass of the payload in the FE mesh, point mass elements having three dof are considered by using the MASS21 element

implemented in ANSYS.

The sampling frequency f_s of the FE analysis is selected as 200 Hz, which correspond to a time step Δt of the numerical algorithm equal to 0.005 s. The sparse solver implemented in ANSYS, suitable for simulating both linear and nonlinear mechanical systems, was selected to carry out the dynamical simulations necessary for performing the transient analysis.

To properly take into account the structural dissipation of the flexible manipulator, two Rayleigh damping coefficients should be considered in the transient analysis of the FE model. To this end, the mass proportional coefficient denoted with α_{fem} and the stiffness proportional coefficient denoted with β_{fem} are estimated with the use of the PDC identification method considered in the paper and by using the first natural frequency $f_{n,\text{exp}}$ and the first damping ratio ξ_{exp} obtained experimentally. By doing so, the α_{fem} and β_{fem} coefficients are respectively estimated equal to $5.7895 \cdot 10^{-8}\ 1/s$ and $9.4204 \cdot 10^{-5}\ s$, which lead to a damping ratio denoted with ξ_{fem} and equal to 0.0019. It is worth observing that including the dissipation effects, modeled as structural damping in the FE model, leads to more accurate numerical results obtained from the transient analysis.

In addition to the transient analysis of the manipulator, a modal analysis of the FE model is carried out in ANSYS to identify the first mode shape and the first natural frequency of the mechanical system under study. In Figure 4.8, the modal displacement associated with the first vibration mode of the FE model of the flexible manipulator constructed using ANSYS is represented.

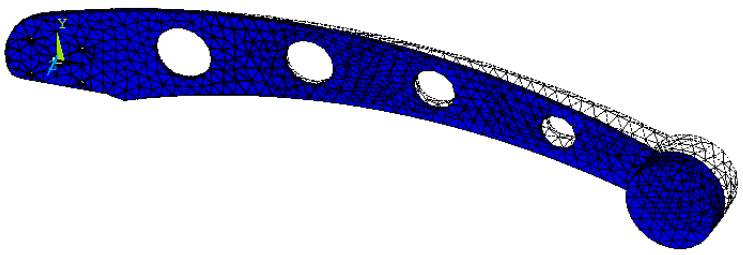


Figure 4.8 First mode shape of the flexible manipulator

As expected, the geometric form of the first normal mode shown in Figure 4.8 obtained for the manipulator is quite similar to the first mode shape of a cantilever beam, while the natural frequency $f_{n,\text{fem}}$ found in the correspondence of the first vibration mode is equal to 6.446 Hz. As discussed below, the numerical results of both the transient analysis and the modal analysis carried out using ANSYS are used for performing a comparative study of the performance of the SI algorithms considered in the thesis.

Output signals are obtained from the FE model according to the global axis. However, the displacement and acceleration signals perpendicular to manipulator are required for the identification. Therefore, the measured signals are calculated according to the local axis. The global and local axis are shown in Figure 4.9.

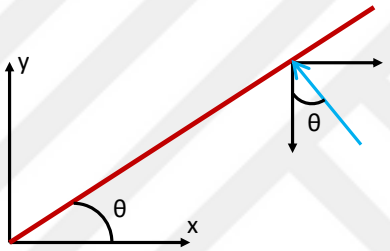


Figure 4.9 The local and global axis of the manipulator

The local output signals are calculated with the global output signals as follows:

$$\begin{aligned} y_d &= -y^g_{d_x} sin(\theta) + y^g_{d_y} cos(\theta) \\ y_a &= -y^g_{a_x} sin(\theta) + y^g_{a_y} cos(\theta) \end{aligned} . \tag{4.3}$$

where $y^g_{d_x}$, $y^g_{d_y}$, $y^g_{a_x}$, $y^g_{a_y}$ represent global displacement signals at x and y directions and global acceleration signals at x and y directions, respectively, whereas y_d and y_a denote local displacement and acceleration signals, respectively.

CHAPTER FIVE
IDENTIFICATION OF FLEXIBLE MANIPULATORS

5.1 Introduction

In this chapter, to compare the four identification methods described in Chapter 2, namely the ARX, CTSI, SSEST, and N4SID techniques, a set of mathematical models of the flexible manipulator is estimated using the vibration responses of the single-link flexible manipulators obtained from the FE model and the experimental system described in Chapter 4. Firstly, the definition of the numerical and experimental signals is provided. The numerical and experimental identification results for the SM are obtained for the ARX, CTSI, SSEST, and N4SID methods. Besides, experimental identification of the composite manipulators is studied with CTSI and N4SID methods. Finally, a comparative analysis of the performance of the identification methods is presented.

5.2 Description of Cases

In this subsection, cases used to identify the steel and composite manipulators are defined. Four flexible links made of steel and composite materials are studied with two different payloads and three different output types as the acceleration, displacement, and strain signals. The cases created for different links, outputs, and payloads are listed in Table 5.1.

It is shown in Table 5.1 that the acceleration signal as an output type is used for the numerical identification of the SM with two payloads. In contrast, the acceleration, displacement, and strain signals are utilized as output types for the experimental identification of the SM with two payloads (m_p = 0.62 kg, m_p = 1.24 kg). Furthermore, the composite manipulators are identified with two payloads and the acceleration signal as the output type.

Table 5.1 Cases

Cases		Material	Orientation	Output Type	$m_p(kg)$
SM	1	Steel	-	acceleration	0.62
	2			acceleration	1.24
	3			displacement	0.62
	4			displacement	1.24
	5			strain	0.62
EGM-a	1	Epoxy-Glass	[0/90]	acceleration	0.62
	2			acceleration	1.24
EGM-b	1	Epoxy-Glass	[45/-45]	acceleration	0.62
	2			acceleration	1.24
ECM	1	Epoxy-Carbon	[0/90]	acceleration	0.62
	2			acceleration	1.24

5.3 Definition of Inputs and Outputs

In this subsection, the set of input and output signals employed for numerical and experimental identification is described. For both the FE model and the experimental system, the input signal is selected as the motion profile that is used to drive the servomotor, while the output signals are chosen as the acceleration, displacement, and strain measurements performed at the tip point of the manipulator. In particular, the shape of the motion profile is selected as a trapezoidal motion profile, which is generally used in the literature to drive industrial robotic manipulators. The trapezoidal motion profile is shown in Figure 5.1.

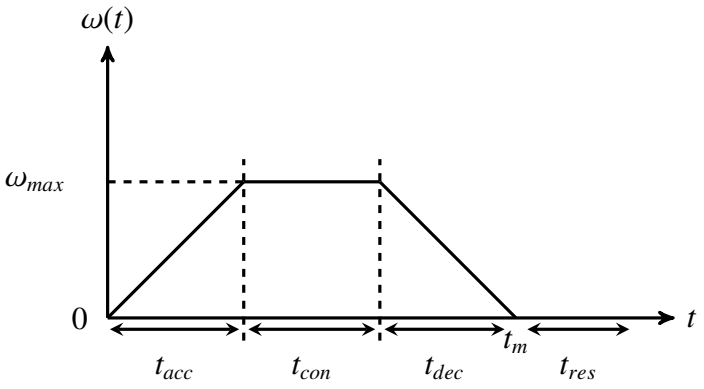


Figure 5.1 Trapezoidal motion profile

In Figure 5.1, t_{acc}, t_{con}, t_{dec}, t_m and t_{res} are the time parameters of the motion profile which represent the acceleration time in s, the constant time in s, the deceleration time in s, the motion time in s and the residual time in s, respectively, whereas ω_{max} denotes the maximum angular velocity of the profile.

Time parameters and maximum angular velocity of the trapezoidal motion input are calculated as follows:

$$
\begin{aligned}
t_{1h} &= \frac{1}{f_{n1}/2} \\
t_{con} &= 2t_{1h} \\
t_{dec} &= 1t_{1h} \quad \text{for identification dataset} \\
t_{dec} &= 3t_{1h} \quad \text{for validation dataset} \\
t_{acc} &= t_m - t_{con} - t_{dec} \\
\omega_{max} &= \frac{\theta_m}{0.5t_{acc} + t_{con} + 0.5t_{dec}}
\end{aligned}
\tag{5.1}
$$

where f_{n1} represents the first natural frequency and t_{1h} denotes the half of first period, whereas θ_m represents the stopping position of the manipulator.

Assuming the trapezoidal motion profile mentioned before, the tip point of the flexible manipulator is displaced from $t_0 = 0$ s and $\theta_m = 0°$ to $t_m = 2$ s and $\theta_m = 60°$. The other parameters that characterize the form of the trapezoidal motion profile were properly selected to obtain the vibration response of the manipulator. Consistent vibration responses are obtained from the FE model and the experimental system corresponding to the same input signal. The input angular velocity signal of the servo motor and the corresponding output acceleration and displacement signals of the manipulator are used for identification methods, are shown in Figures 5.2, 5.3 and 5.4.

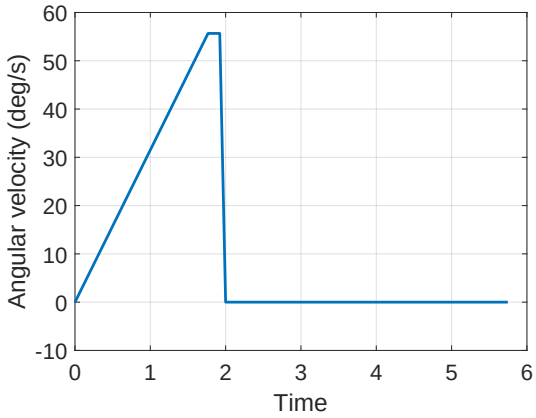
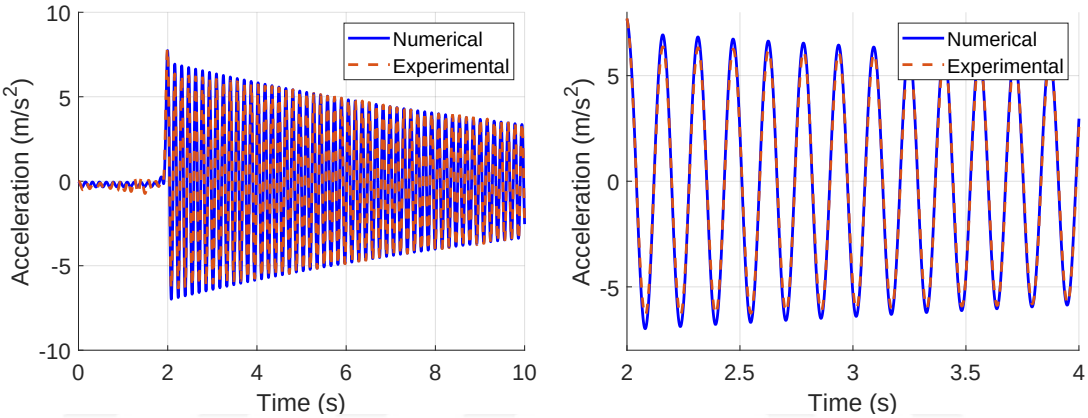
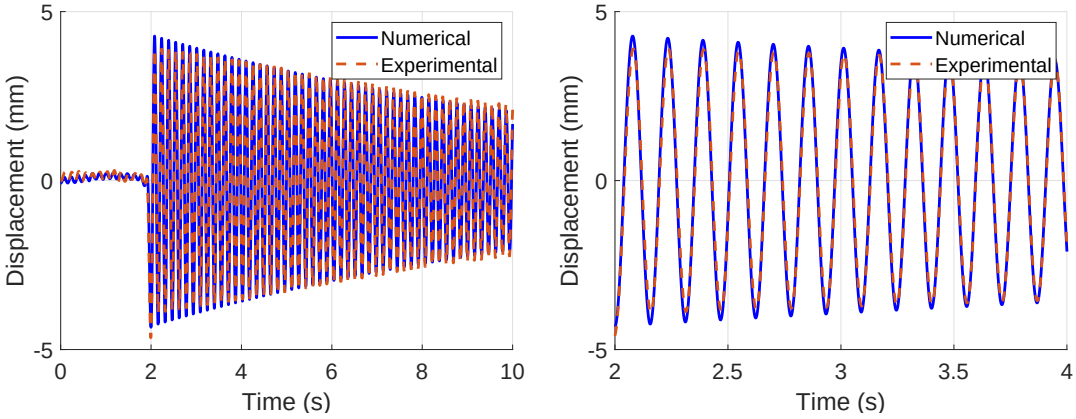


Figure 5.2 Input signal



(a) Complete time span (b) Zoomed time window

Figure 5.3 Comparison of acceleration output signals



(a) Complete time span (b) Zoomed time window

Figure 5.4 Comparison of displacement output signals

In particular, Figure 5.2 represents the angular velocity profile that drives the servo motor considered as the input signal, Figure 5.3 represents the acceleration signals of the SM obtained from the numerical and the experimental vibration responses and the zoomed time window of the acceleration signal, whereas Figure 5.4 represents the displacement signals of the SM obtained from the numerical and the experimental vibration responses and the zoomed time window of the displacement signal. As shown in Figures 5.3 and 5.4, the numerical and experimental vibration responses of the manipulator made of steel material for displacement and acceleration signals are successfully matched for the trapezoidal motion input.

5.4 Identification Results of Steel Manipulator

In this subsection, the identification of the SM is studied with four identification approaches: the ARX, CTSI, SSEST, and N4SID. The mathematical models of the flexible manipulator are obtained as a discrete-time transfer function in the case of the ARX method, a continuous-time transfer function in the case of the CTSI method, a continuous-time state-space model in the case of the SSEST method, and a discrete-time state-space model in the case of the N4SID method.

In the N4SID method, different weighting matrices are studied. At the end of the preliminary analysis performed considering the weighting matrices to be used in the N4SID method, the CVA approach is chosen as the weighting matrix because this approach provides the best set of numerical and experimental results. For performing the dynamical simulations as well as for running the identification computational algorithms, the initial conditions are set to zero for all methods.

5.4.1 Analysis of Identification Using the Finite Element Model

The mathematical models of the manipulator are identified using the numerical dataset obtained from the FE model of the manipulator. The identification results obtained from the numerical analysis of the SM are compared to the four identification methods analyzed. To present the identified results obtained from the numerical analysis in a compact and synthetic fashion, the identified continuous-time state-space matrices are reported in Appendix C.

A comparison of the vibration responses of the FE model and the identified mathematical models is shown in Figures 5.5 and 5.6 for the identification and validation dataset.

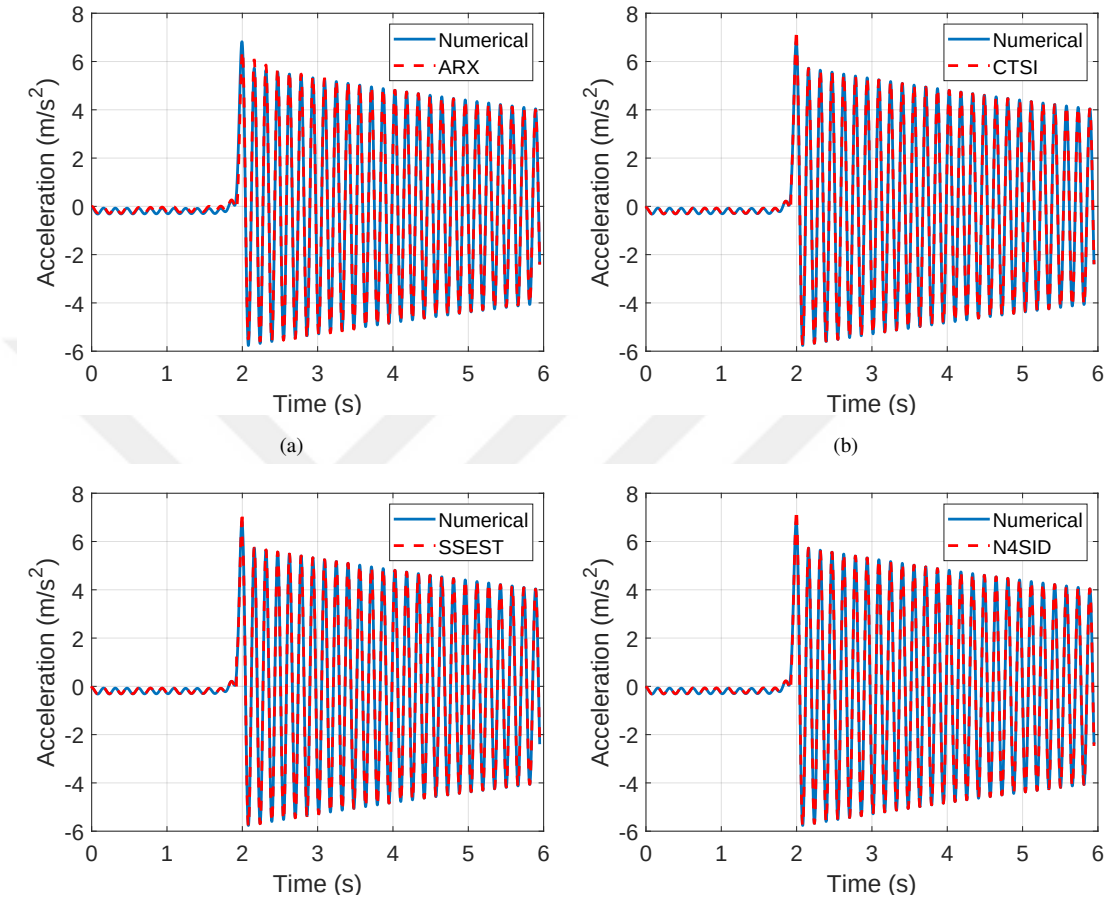


Figure 5.5 Comparison of the vibration responses obtained from (a) ARX (b) CTSI (c) SSEST (d) N4SID for identification dataset

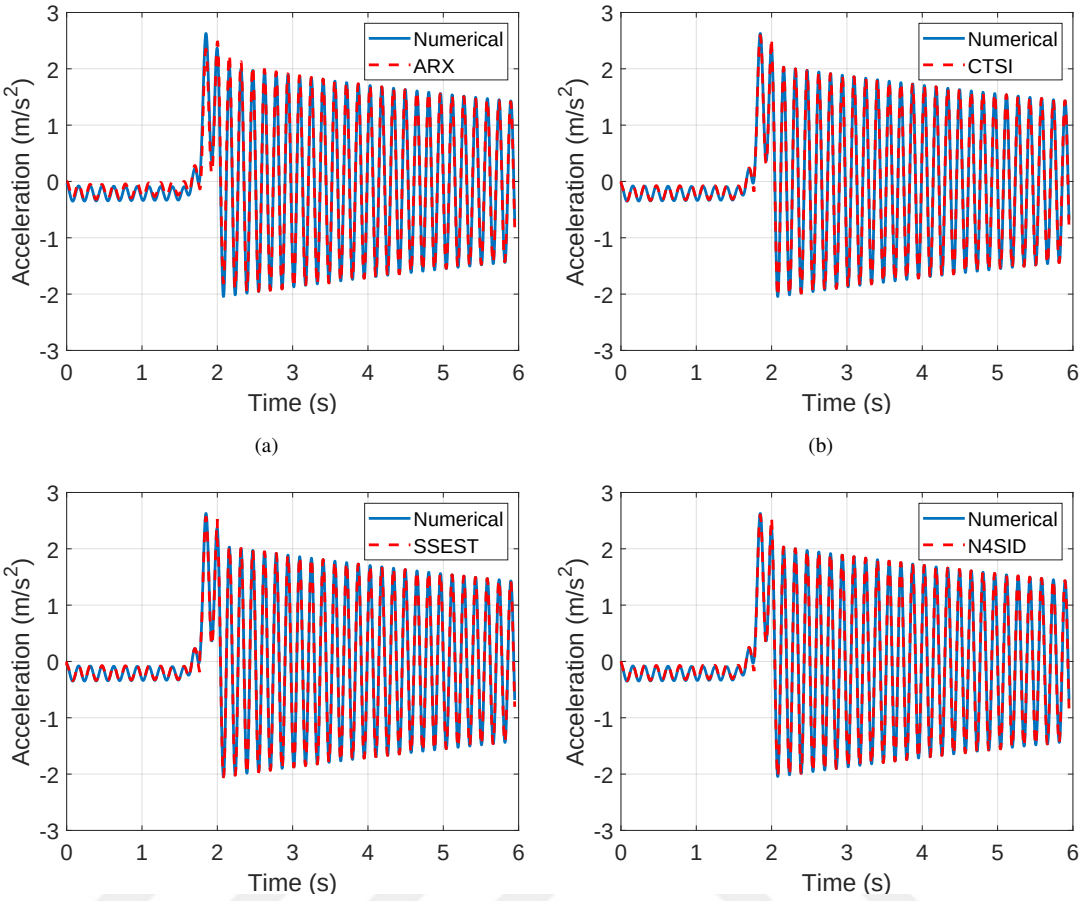


Figure 5.6 Comparison of the vibration responses obtained from (a) ARX (b) CTSI (c) SSEST (d) N4SID for validation dataset

In Figures 5.5a and 5.6a, the vibration responses of the FE model are compared with those obtained using the identified model determined with the ARX model, in Figures 5.5b and 5.6b, the vibration responses of the FE model are compared with those obtained using the identified model determined with the CTSI method, in Figures 5.5c and 5.6c, the vibration responses of the FE model are compared with those obtained using the identified state-space model determined with the SSEST method, whereas in Figures 5.5d and 5.6d, the vibration responses of the FE model are compared with those obtained using the identified state-space model determined with the N4SID method.

By observing Figures 5.5 and 5.6, it is apparent that the identified vibration responses are matched well with the vibration response of the FE model constructed for the manipulator.

In order to consistently compare the performance of the identification methods of interest for this investigation, the identification process is focused only on the estimation of the first natural frequency corresponding to the first mode shape of the manipulator, which is predominant in its vibratory motion. It is difficult to comment on vibration results over time responses. Therefore, vibration results can be evaluated with the RMS values of time-domain vibration signals. The RMS values are calculated from the residual vibrations of the manipulator. The RMS formula can be given as follows:

$$RMS = \sqrt{\frac{1}{n}\sum_{i=1}^{n} y_i^2} \tag{5.2}$$

where n is the number of samples and y_i is the samples of a vibration signal. Subsequently, the complete set of numerical results including the fit and RMS values, the identified natural frequencies, the identified damping factors and relative errors for the identified mathematical models using the identification methods analyzed are provided in Table 5.2.

Table 5.2 Identification results for the numerical analysis

	Numerical	ARX	CTSI	SSEST	N4SID
Model order		[3,3,1]	[3,3]	2	3
Fit id (%)	-	94.51	98.87	94.15	97.46
Fit val (%)	-	89.84	94.75	88.54	92.9
RMS id (m/s^2)	3.4603	3.475	3.46	3.48	3.468
RMS val (m/s^2)	1.2264	1.235	1.229	1.234	1.232
$\hat{f}_n$(Hz)	6.44	6.4250	6.4260	6.4250	6.4260
$\hat{\xi}$	0.0019	0.0025	0.0023	0.0026	0.0023
Relative error $\hat{f}_n$	-	2.35×10^{-3}	2.20×10^{-3}	2.37×10^{-3}	2.21×10^{-3}
Relative error $\hat{\xi}$	-	3.16×10^{-1}	2.14×10^{-1}	3.51×10^{-1}	2.16×10^{-1}

In Table 5.2, $\hat{f}_n$ and $\hat{\xi}$ respectively represent the identified natural frequency and the identified damping ratio originally obtained from the implementation of the various identification methods. In Table 5.2, the relative errors for both the identified natural frequency $\hat{f}_n$ and the identified damping ratio $\hat{\xi}$ found for each method are computed by considering the corresponding numerical values respectively. For the identified transfer functions, the numerator, denominator and delay orders of the ARX model are selected as $n_a = 3$, $n_b = 3$ and $n_k = 1$, whereas the numerator, the denominator orders of the CTSI model are selected as $m = 3$, $n = 3$ according to final prediction error criteria and fit values,

respectively. For the identified state-space models, the model order of the SSEST model is selected as 2, whereas the model order of the N4SID model is selected as 3 according to FPE criteria and fit values.

It is apperent in Table 5.2 that the fit values of the identified models are found as 94.51 %, 98.87 %, 94.15 %, 97.46 % for the identification dataset and 89.84 %, 94.75 %, 88.54 %, 92.9 % with validation dataset using the ARX, CTSI, SSEST and N4SID methods. The best relative error of the identified natural frequency is 2.20×10^{-3}, while the best relative error of the identified damping ratio is 2.14×10^{-1} obtained with the CTSI method.

The frequency responses of the FE model and the identified mathematical models obtained from the ARX, CTSI, SSEST and N4SID methods are shown in Figure 5.7.

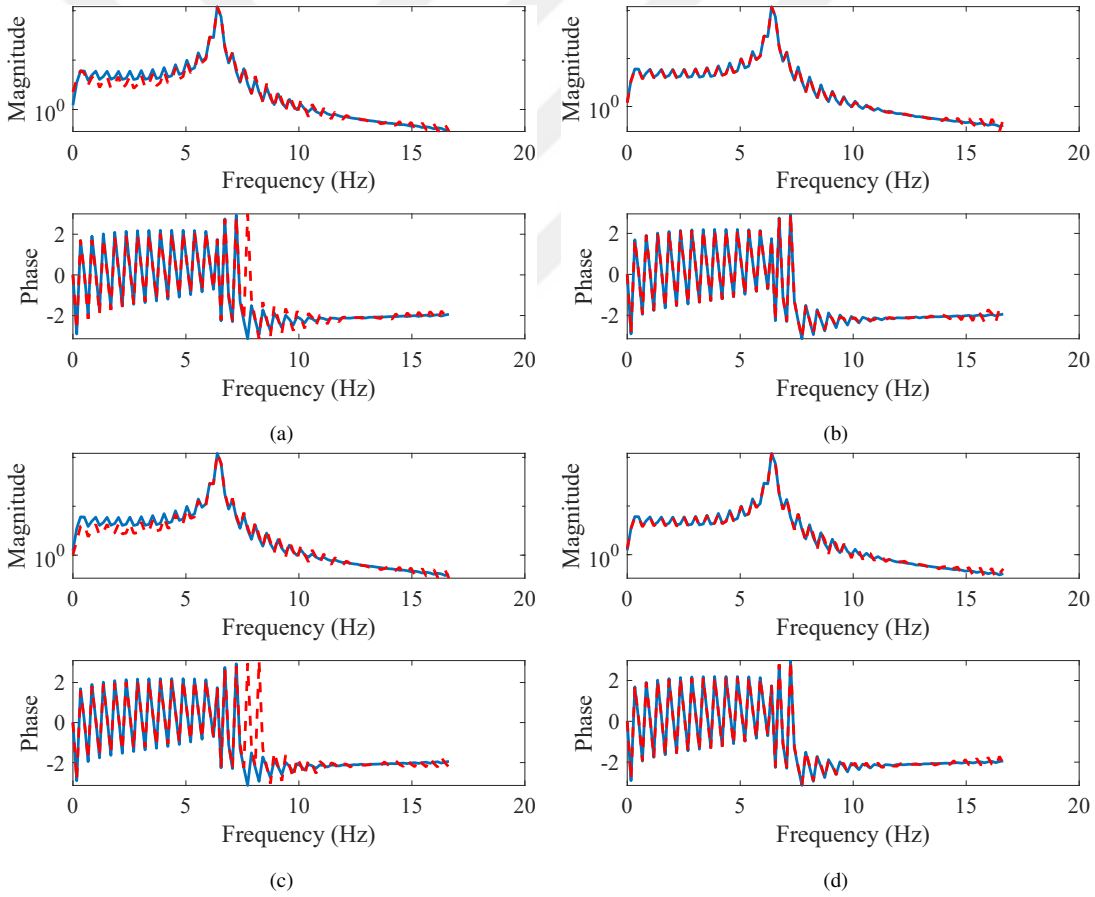


Figure 5.7 Comparison of the frequency responses obtained from (a) ARX (b) CTSI (c) SSEST (d) N4SID for SM-1

It is shown in Figure 5.7 that the frequency responses of the identified mathematical models obtained from the identification methods especially CTSI and N4SID methods are successfully

matched with the frequency response of the FE model.

5.4.2 Analysis of Identification Using the Experimental Signals

In this subsection, the identification results obtained from the use of the experimental system of the SM are compared considering the computer implementation of the four identification methods analyzed. To present the identified results obtained from the experimental analysis in a compact and synthetic fashion, the identified continuous-time state-space matrices are reported in Appendix D.

Comparison of the time and frequency vibration responses of the experimental system and the identified mathematical models for the acceleration signal as output type are shown in Figures 5.8 and 5.9.

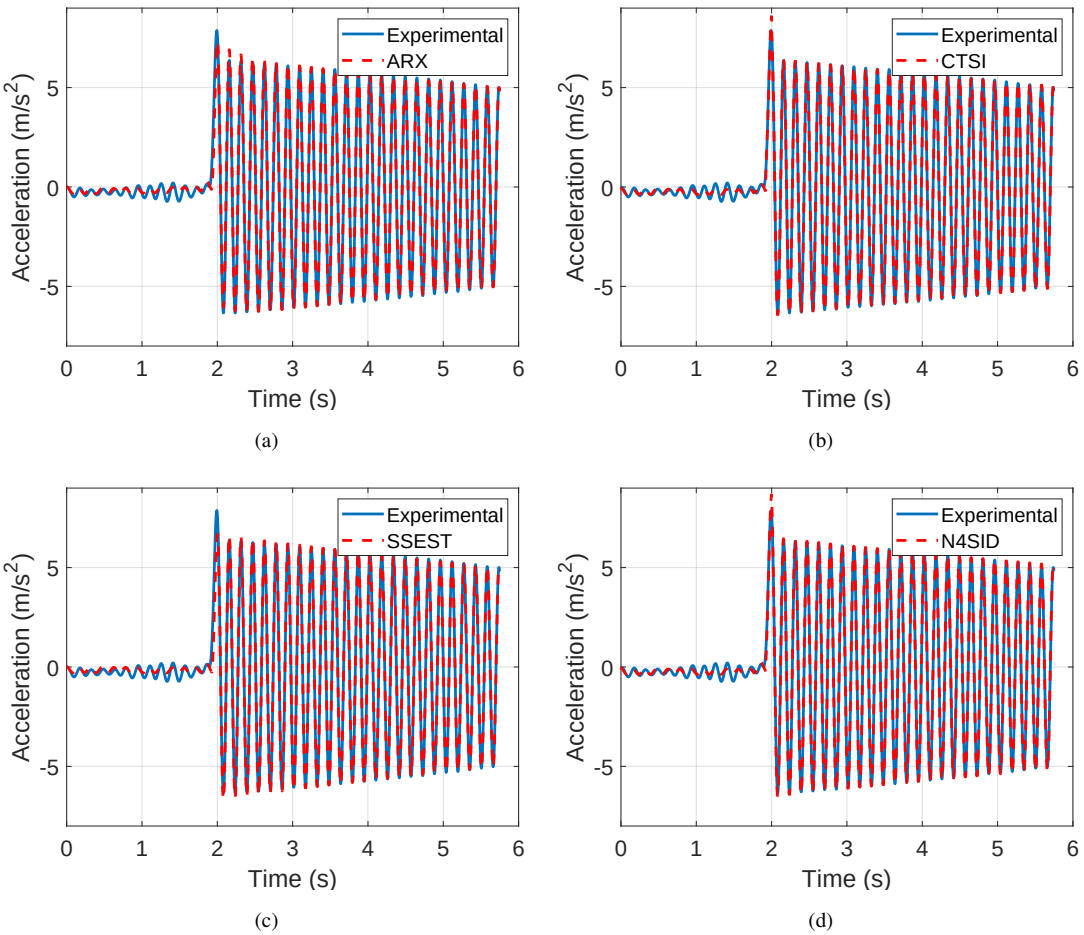


Figure 5.8 Comparison of the vibration responses obtained from (a) ARX (b) CTSI (c) SSEST (d) N4SID for SM-1

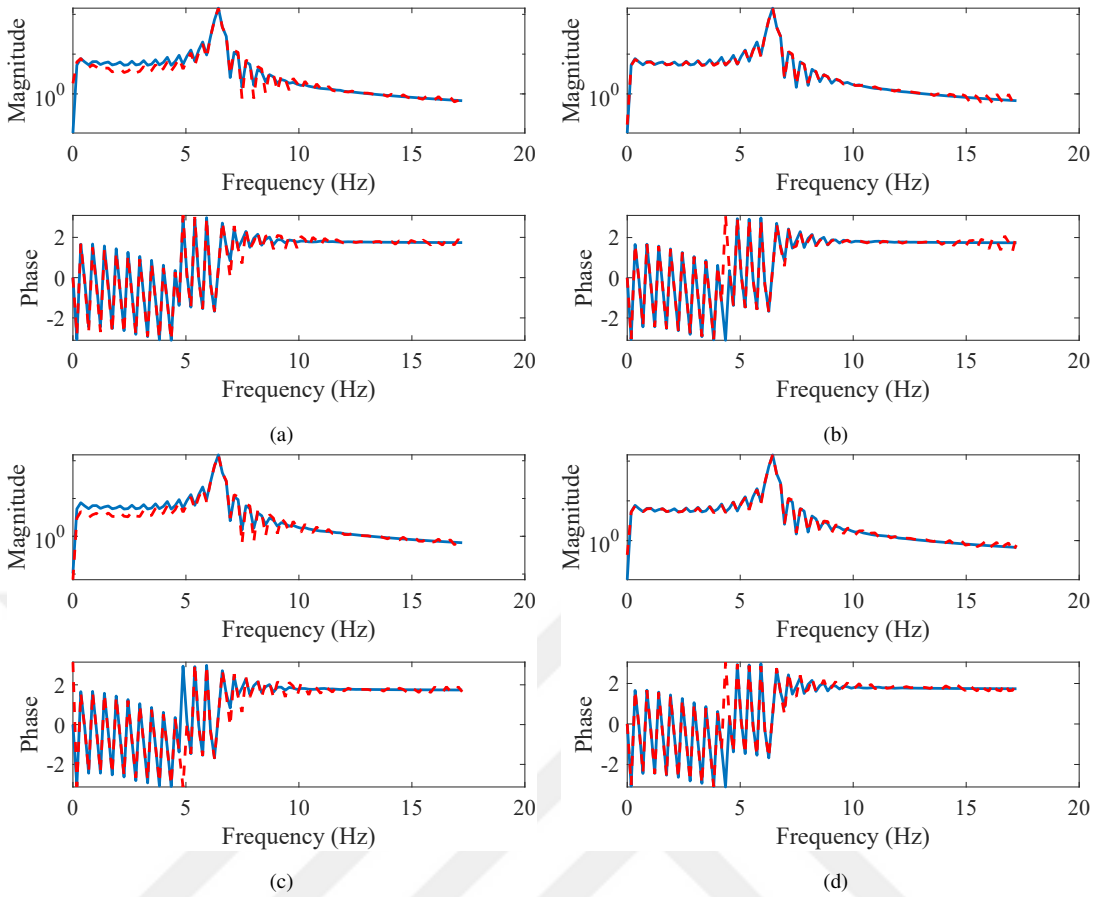


Figure 5.9 Comparison of the frequency responses obtained from (a) ARX (b) CTSI (c) SSEST (d) N4SID for SM-1

By observing the experimental results shown in Figures 5.8 and 5.9 , it is apparent that the identified vibration responses successfully match with the vibration responses of the experimental system up for SM-1.

Comparison of the time and frequency vibration responses of the experimental system and the identified mathematical models for the displacement signal as output type are shown in Figures 5.10 and 5.11.

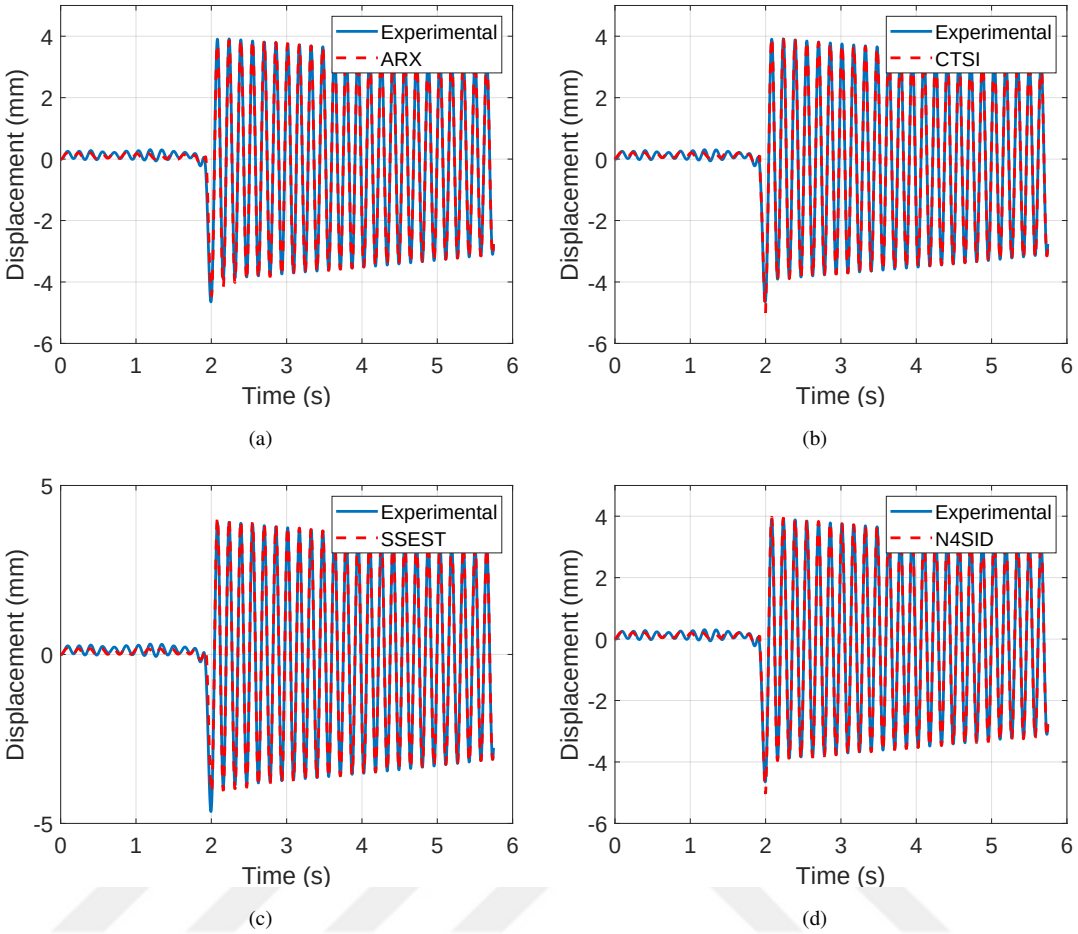


Figure 5.10 Comparison of the vibration responses obtained from (a) ARX (b) CTSI (c) SSEST (d) N4SID for SM-3

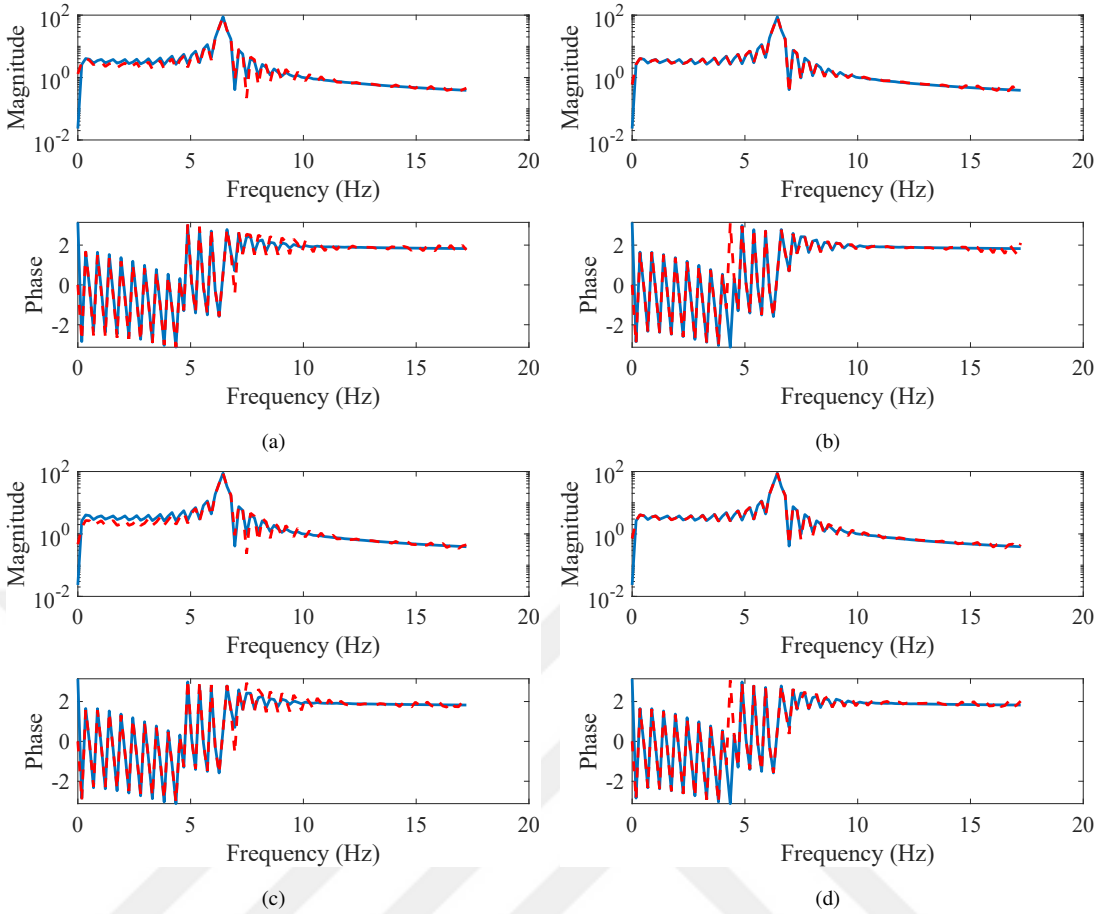


Figure 5.11 Comparison of the frequency responses obtained from (a) ARX (b) CTSI (c) SSEST (d) N4SID for SM-3

By observing the experimental results shown in Figures 5.10 and 5.11, it is apparent that the identified frequency responses obtained using the identified models determined with the ARX, CTSI, SSEST, N4SID are matched well the displacement frequency response of the experimental system for SM-3.

Figure 5.12 represents the vibration responses of the experimental system and the identified mathematical models for strain output.

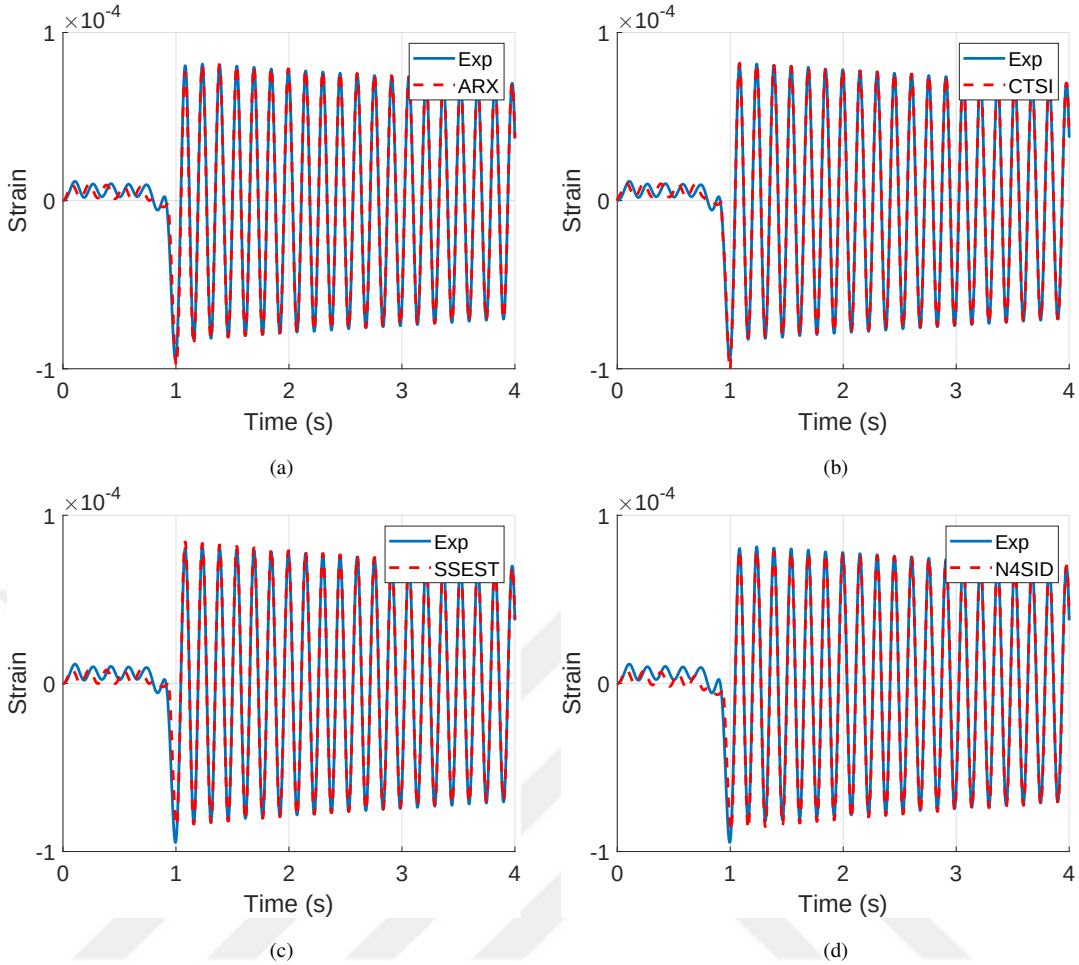


Figure 5.12 Comparison of the vibration responses obtained from (a) ARX (b) CTSI (c) SSEST (d) N4SID for SM-5

It is shown in Figure 5.12, the identified vibration responses obtained using the identified models determined with the ARX, CTSI, SSEST, N4SID are matched well the experimental vibration signals for SM-5.

To compare the performance of the identification methods, the complete set of experimental results including the natural frequencies, the damping factors, relative errors for the identified mathematical models are provided in Tables 5.3 and 5.4.

Table 5.3 Identification results of (a) SM-1 and SM-2 (b) SM-3 and SM-4

(a)

	SM-1					SM-2				
	Exp	ARX	CTSI	SSEST	N4SID	Exp	ARX	CTSI	SSEST	N4SID
Model order	-	[3,3,1]	[3,3]	2	3	-	[3,3,1]	[3,3]	2	3
Fit id (%)	-	92.63	97.03	92.22	94.58	-	91.75	97.41	91.02	95.93
Fit val (%)	-	88.14	92.3	85.85	91.23	-	79.25	80.22	76.67	82.26
RMS id (m/s^2)	4.0925	4.1070	4.0920	4.1210	4.1360	2.8848	2.9060	2.8850	2.9130	2.8830
RMS val (m/s^2)	1.4750	1.4640	1.4570	1.4640	1.4730	1.0478	1.0110	1.0020	1.0090	1.0010
$\hat{f}_n(Hz)$	6.4200	6.4220	6.4240	6.4220	6.4240	4.8600	4.8390	4.8410	4.8390	4.8410
$\hat{\xi}$	0.0019	0.0018	0.0016	0.0019	0.0016	0.0021	0.0025	0.0020	0.0026	0.0020
Relative error $\hat{f}_n$	-	3.49×10^{-4}	5.65×10^{-4}	3.33×10^{-4}	5.51×10^{-4}	-	4.27×10^{-3}	3.85×10^{-3}	4.28×10^{-3}	3.85×10^{-3}
Relative error $\hat{\xi}$	-	2.77×10^{-2}	1.62×10^{-1}	1.36×10^{-2}	1.71×10^{-1}	-	2.10×10^{-1}	3.48×10^{-2}	2.60×10^{-1}	3.34×10^{-2}

(b)

	SM-3					SM-4				
	Exp	ARX	CTSI	SSEST	N4SID	Exp	ARX	CTSI	SSEST	N4SID
Model order	-	[3,3,1]	[3,3]	2	3	-	[3,3,1]	[3,3]	2	3
Fit id (%)	-	94.41	97.97	94.05	95.76	-	90.04	96.39	90.45	94.06
Fit val (%)	-	84.89	84.84	81.8	87.17	-	81.1	88.07	82.29	87.28
RMS id (mm)	2.5235	2.5320	2.5240	2.5370	2.5470	2.7654	2.8200	2.7640	2.7930	2.8390
RMS val (mm)	0.8673	0.9048	0.9016	0.9048	0.9099	0.9489	0.9810	0.9629	0.9701	0.9892
$\hat{f}_n(Hz)$	6.4200	6.4310	6.4320	6.4310	6.4320	4.8600	4.8450	4.8460	4.8440	4.8460
$\hat{\xi}$	0.0019	0.0017	0.0015	0.0018	0.0015	0.0021	0.0027	0.0021	0.0027	0.0021
Relative error $\hat{f}_n$	-	1.66×10^{-3}	1.83×10^{-3}	1.65×10^{-3}	1.82×10^{-3}	-	3.08×10^{-3}	2.87×10^{-3}	3.26×10^{-3}	2.87×10^{-3}
Relative error $\hat{\xi}$	-	1.09×10^{-1}	2.01×10^{-1}	6.25×10^{-2}	2.08×10^{-1}	-	2.79×10^{-1}	8.42×10^{-3}	2.95×10^{-1}	5.18×10^{-3}

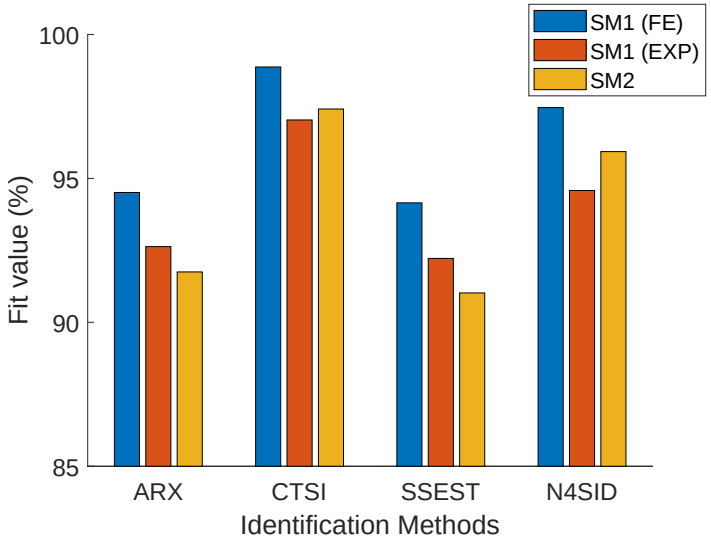
Table 5.4 Identification results of SM-5

	Exp	ARX	CTSI	SSEST	N4SID
	-	[3,3,1]	[3,3]	2	3
Fit id (%)	-	92.76	95.83	91.92	90.97
Fit val (%)	-	81.73	85.48	79.90	79.36
RMS id	5.411×10^{-5}	5.439×10^{-5}	5.407×10^{-5}	5.443×10^{-5}	5.457×10^{-5}
RMS val	1.731×10^{-5}	1.844×10^{-5}	1.829×10^{-5}	1.840×10^{-5}	1.857×10^{-5}
$\hat{f}_n(Hz)$	6.4200	6.5640	6.5656	6.5634	6.5657
$\hat{\xi}$	0.0019	0.0014	0.0013	0.0017	0.0014
Relative error $\hat{f}_n$	-	2.24×10^{-2}	2.27×10^{-2}	2.23×10^{-2}	2.27×10^{-2}
Relative error $\hat{\xi}$	-	2.54×10^{-1}	3.21×10^{-1}	1.11×10^{-1}	2.75×10^{-1}

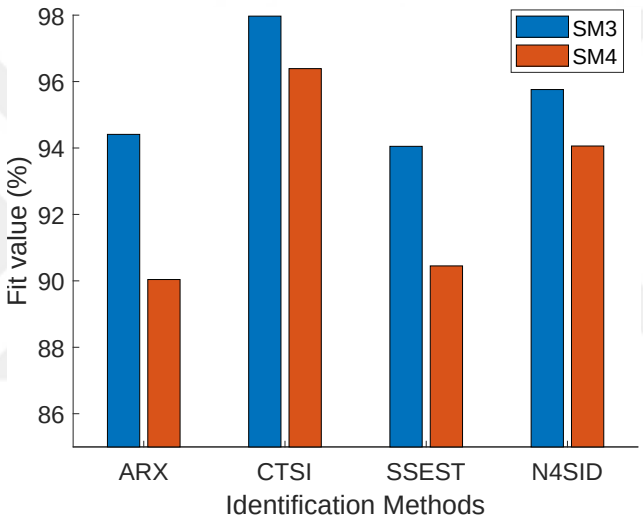
In Tables 5.3 and 5.4, the identified natural frequencies of the SM1 are 6.4220 Hz, 6.4240 Hz, 6.4220 Hz, and 6.4240 , the identified natural frequencies of the SM3 are 6.4310 Hz, 6.4320 Hz, 6.4310 Hz and 6.4320 Hz, while the identified natural frequencies of the SM5 are 6.5640 Hz, 6.5656 Hz, 6.5634 Hz and 6.5657 Hz obtained by using ARX, CTSI, SSEST and N4SID methods. It is observed from the identified natural frequencies and relative error of the identified natural frequencies that the best identification results are obtained from the acceleration signals as the output type of the manipulator.

For acceleration output and various payloads, the RMS values of the SM-1 are obtained as 4.0925 m/s^2, 4.1070 m/s^2, 4.0920 m/s^2, 4.1210 m/s^2 and 4.1360 m/s^2, whereas the RMS values of SM-2 are 2.8848 m/s^2, 2.9060 m/s^2, 2.8850 m/s^2, 2.9130 m/s^2, and 2.8830 m/s^2 for vibration responses of experimental signal and the identified model determined with the ARX, CTSI, SSEST and N4SID, respectively. The RMS values obtained from the identified model with the ARX model match well with the RMS values of the vibration responses measured from the experimental system for two payloads.

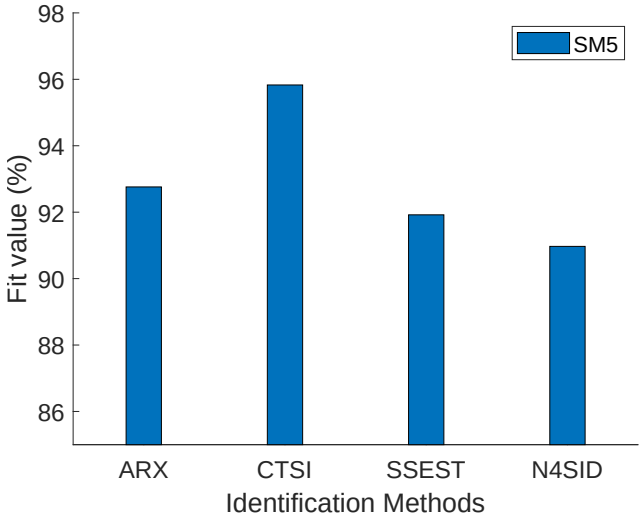
To analyze the performance and effectiveness of the ARX, CTSI, SSEST and N4SID methods, the fit values for two payloads and three output types as acceleration, displacement and strain signals are shown in Figure 5.13 for the experimental signals.



(a)



(b)



(c)

Figure 5.13 Comparison of identification results for (a) acceleration (b) displacement (c) strain signals

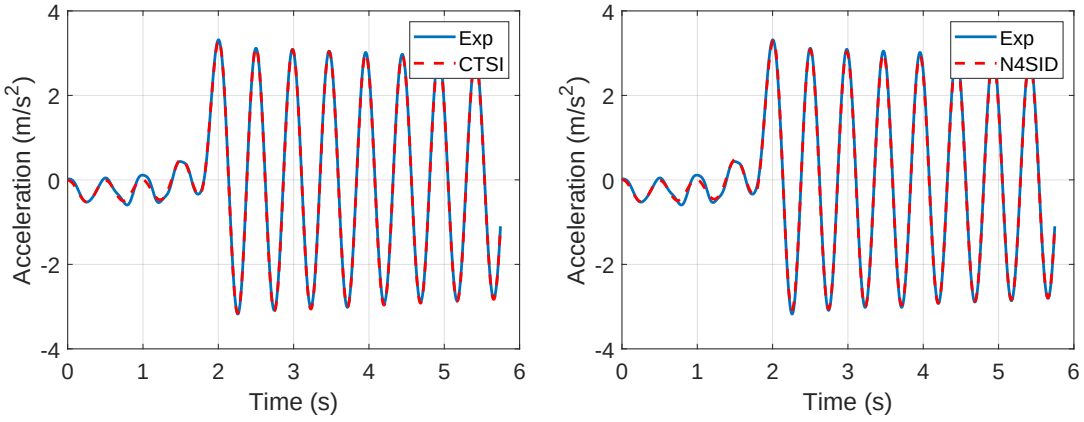
Figure 5.13a shows the fit values obtained from the acceleration signals of the manipulator for m_p = 0.62 kg and m_p = 1.24 kg via the numerical and experimental dataset, Figure 5.13b shows the fit values obtained from the displacement signals of the manipulator for m_p = 0.62 kg and m_p = 1.24 kg via the experimental dataset and Figure 5.13c shows the fit values obtained from the strain signals of the manipulator for m_p = 0.62 kg via the experimental dataset. It is apparent from Figure 5.13 that for all cases and identification methods, the fit values are over 90 %. The CTSI and N4SID methods, in particular, demonstrate a powerful identification capability for the manipulator for all output types.

It is observed from Figure 5.13a that the identification results obtained from the FE model are more successful than those obtained from the experimental system since the vibration responses obtained from the FE model are not affected by noise.

5.5 Identification Results of Composite Manipulators

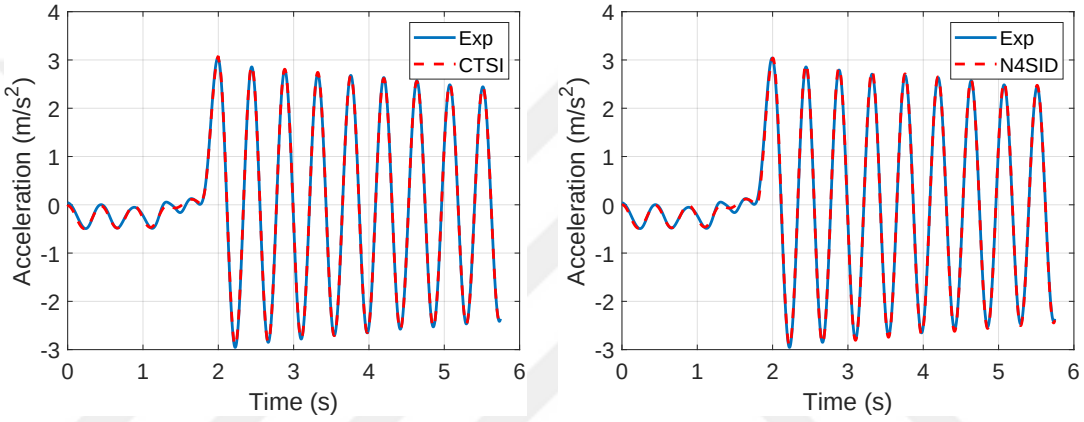
In this subsection, the identification of the composite manipulators made of epoxy-carbon and epoxy-glass materials with different lay-ups is examined thoroughly using knowledge of modeling of the SM observed in Figure 5.13. In modeling of the SM, the CTSI and N4SID techniques are more successful than other methods. Therefore, the CTSI and N4SID methods are employed to identify composite manipulators. The identification of the manipulators is studied for two different payloads to examine the effect of the payload on the identification. For performing the CTSI and N4SID algorithms, the initial conditions are set to zero for all methods.

Figures 5.14, 5.15, 5.16 show the vibration responses of the experimental system and the identified mathematical models obtained from the CTSI and N4SID with payload m_p = 0.62 kg for the EGM-a, the EGM-b and ECM, respectively.



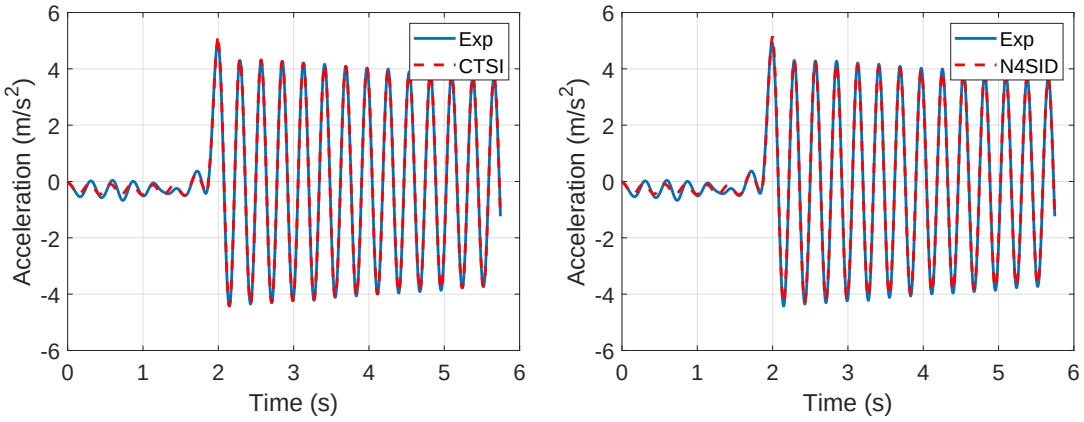
(a) (b)

Figure 5.14 Vibration responses of the EGM-a for (a) the CTSI method and (b) N4SID method



(a) (b)

Figure 5.15 Vibration responses of the EGM-b for (a) the CTSI method and (b) N4SID method



(a) (b)

Figure 5.16 Vibration responses of the ECM for (a) the CTSI method and (b) N4SID method

Figures 5.14a, 5.15a, 5.16a show the vibration responses of the identified model obtained from the CTSI method, while Figures 5.14b, 5.15b, 5.16b show the vibration responses of the identified model obtained from the N4SID method. As seen from Figures 5.14, 5.15 and 5.16,

the experimental vibration responses of the composite manipulators are successfully matched with the identified model responses for the CTSI and N4SID methods.

Model orders, fit and RMS values for identification and validation datasets, the identified natural frequencies denoted with $\hat{f}_n$ (Hz), the identified damping ratios denoted with $\hat{\xi}$ and relative errors for the identified natural frequencies and the identified damping ratios are listed for the EGM-a, EGM-b and ECM in Table 5.5 for two different payloads as $m_p = 0.62$ kg and $m_p = 1.24$ kg.

In Table 5.5a, the identified natural frequencies and the identified damping ratios of three composite manipulator for $m_p = 0.62$ kg are given, whereas the identified natural frequencies and the identified damping ratios for $m_p = 1.24$ kg are listed in Table 5.5b. For the EGM-a1, the natural frequencies for the experimental system, the identified model from the CTSI and N4SID approaches are 2.12 Hz, 2.06 Hz and 2.06 Hz, respectively, while the natural frequencies for the experimental system, the identified model from the CTSI and N4SID approaches are 1.46 Hz, 1.472 Hz and 1.472 Hz for EGM-a1, respectively.

It is apperent in Table 5.5a that the results of the CTSI method is more successful than that of N4SID approach. For example, the RMS values of the identification datasets of the EGM-a1 for experimental vibration response, the CTSI vibration response and N4SID vibration response are 2.1331 m/s^2, 2.1340 m/s^2 and 2.1040 m/s^2, respectively, while the RMS values of the identification datasets of the EGM-a2 for experimental vibration response, the CTSI vibration response and N4SID vibration response are 1.6694 m/s^2, 1.6740 m/s^2 and 1.6250 m/s^2, respectively.

To analyze the performance and effectiveness of the ARX, CTSI, SSEST and N4SID methods, the fit values for two payloads and three output types as acceleration, displacement and strain signals are shown in Figure 5.17 for the experimental signals.

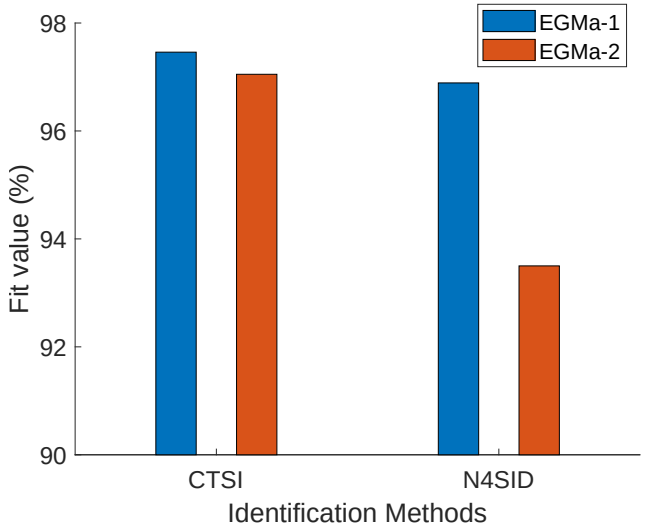
Table 5.5 Identification results of composite manipulators (a) $m_p = 0.62$ kg (b) $m_p = 1.24$ kg

(a)

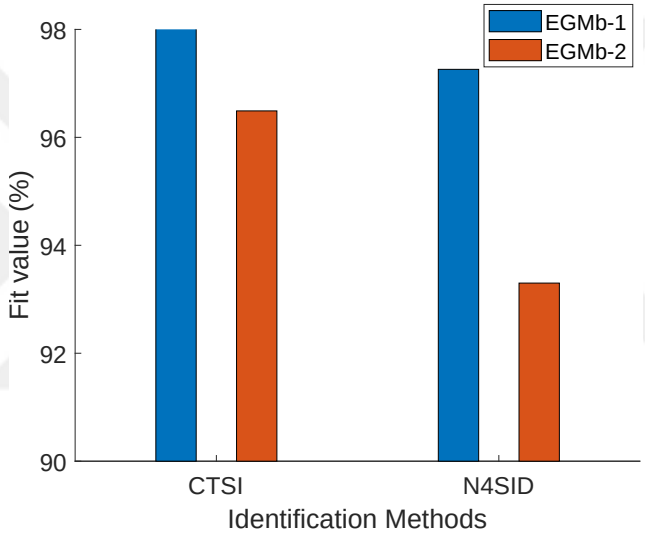
	EGM-a1			EGM-b1			ECM-1		
	Exp	CTSI	N4SID	Exp	CTSI	N4SID	Exp	CTSI	N4SID
Model order	-	[3,3]	3	-	[3,3]	3	-	[3,3]	3
Fit id (%)	-	97.46	96.89	-	98.09	97.26	-	97.17	95.64
Fit val (%)	-	91.87	91.69	-	88.4	87.94	-	86.02	84.78
RMS id (m/s^2)	2.1331	2.1340	2.1040	1.8944	1.8950	1.9180	2.8709	2.8720	2.82
RMS val (m/s^2)	1.0450	1.0220	1.0080	0.6524	0.6475	0.6557	1.0825	1.1260	1.105
$\hat{f}_n(Hz)$	2.1200	2.0600	2.06	2.2800	2.2810	2.2810	3.5600	3.5580	3.557
$\hat{\xi}$	0.0027	0.00245	0.0024	0.0036	0.0037	0.0036	0.0035	0.0022	0.002223
Relative error $\hat{f}_n$	-	2.83×10^{-2}	2.85×10^{-2}	-	4.80×10^{-4}	4.24×10^{-4}	-	6.97×10^{-4}	7.15×10^{-4}
Relative error $\hat{\xi}$	-	7.87×10^{-2}	1.09×10^{-1}	-	3.69×10^{-2}	1.04×10^{-2}	-	3.62×10^{-1}	3.65×10^{-1}

(b)

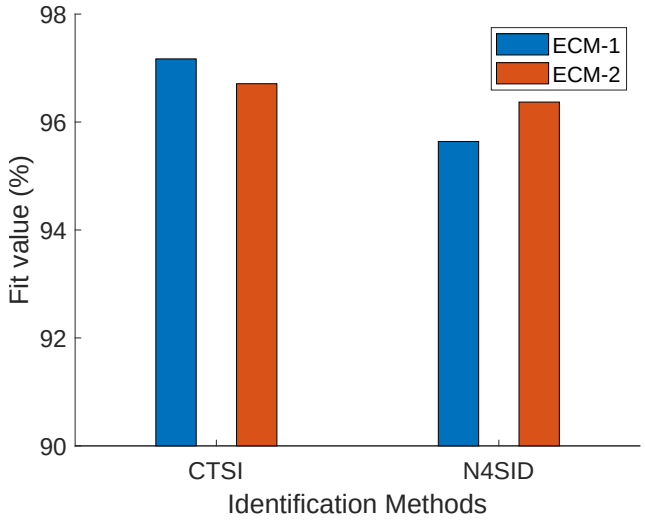
	EGM-a2			EGM-b2			ECM-2		
	Exp	CTSI	N4SID	Exp	CTSI	N4SID	Exp	CTSI	N4SID
Model order	-	[3,3]	3	-	[3,3]	3	-	[3,3]	3
Fit id (%)	-	97.05	93.5	-	96.49	93.3	-	96.71	96.37
Fit val (%)	-	92.46	91.77	-	94.1	91.4	-	85.43	84.93
RMS id (m/s^2)	1.6694	1.6740	1.6250	1.4692	1.4700	1.5040	2.4974	2.4970	2.516
RMS val (m/s^2)	1.8135	1.8040	1.7580	0.7768	0.7641	0.7810	1.0976	1.0650	1.073
$\hat{f}_n(Hz)$	1.4600	1.4720	1.4720	1.6600	1.6530	1.6530	2.6000	2.5830	2.583
$\hat{\xi}$	0.0024	0.0028	0.0025	0.0040	0.0038	0.0038	0.0021	0.0016	0.001609
Relative error $\hat{f}_n$	-	8.14×10^{-3}	8.35×10^{-3}	-	4.39×10^{-3}	4.18×10^{-3}	-	6.61×10^{-3}	6.69×10^{-3}
Relative error $\hat{\xi}$	-	1.75×10^{-1}	4.43×10^{-2}	-	5.38×10^{-2}	4.09×10^{-2}	-	2.42×10^{-1}	2.34×10^{-1}



(a)



(b)



(c)

Figure 5.17 Comparison of identification results for (a) EGM-a (b) EGM-b (c) ECM

Figure 5.17a shows the fit values obtained from the composite manipulator made of epoxy-glass material with [0/90] lay-up, Figure 5.17b shows the fit values obtained from composite manipulator made of epoxy-glass material with [45/-45] lay-up, Figure 5.17c shows the fit values obtained from composite manipulator made of epoxy-carbon material with [0/90] lay-up via the experimental dataset. It is apparent from Figure 5.17 that the fit values are over 93 % for the CTSI and N4SID.

CHAPTER SIX
PASSIVE VIBRATION CONTROL OF FLEXIBLE MANIPULATORS

6.1 Introduction

In this chapter, passive vibration control is studied using various motion profiles for steel and composite manipulators. S-curve motion input and the optimized motion input with the GA are utilized to suppress the vibration response of the manipulators. For S-curve motion input, time parameters are determined based on the first natural frequency of the manipulator. Due to the higher flexibility of composite manipulators compared to steel manipulators, the time parameters of the trapezoidal motion input are optimized with the GA to successfully suppress residual vibration responses of the composite manipulators. The mathematical models determined using the CTSI method, which is the most powerful method in Chapter 5, are utilized to optimize time parameters with the GA. Experimental vibration responses and identified vibration responses are compared to evaluate the success and effectiveness of the S-curve motion input and optimization with the GA for the steel and composite manipulators.

6.2 S-Curve Motion Input

Industrial manipulators are worked with servo motors utilizing generally triangle and trapezoidal velocity profiles (Malgaca et al., 2016). Different motion inputs can be generated to drive the servo motors (Ankaralı et al., 2012; Fang et al., 2019; Li et al., 2009). To suppress unwanted vibrations, the motion input and its properties are critical in control practices. In this thesis, a S-curve motion input is designed to reduce residual vibrations of the SM.

6.2.1 Design of S-curve Motion Input

An ideal S-curve motion input is seven-segment one, whereas the designed S-curve motion input is five-segment one as shown in Figure 6.1.

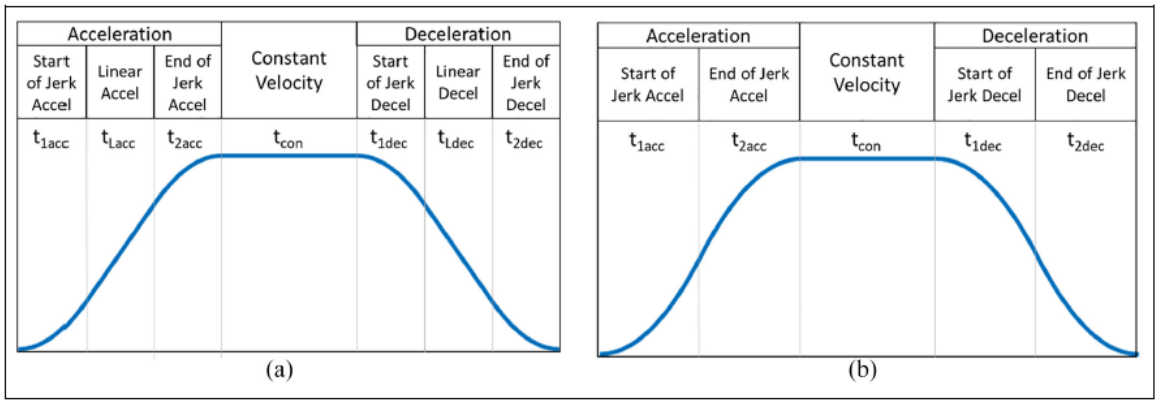


Figure 6.1 S-curve motion input

The motion time t_m can be expressed in the ideal S-curve motion input as follows:

$$\begin{aligned} t_m &= t_{1acc} + t_{Lacc} + t_{2acc} + t_{con} + t_{1dec} + t_{Ldec} + t_{2dec} \\ t_{acc} &= t_{1acc} + t_{Lacc} + t_{2acc} \\ t_{dec} &= t_{1dec} + t_{Ldec} + t_{2dec} \end{aligned} \tag{6.1}$$

where t_{acc} is the acceleration time, t_{con} is the constant velocity time and t_{dec} is the deceleration time. t_{acc} and t_{dec} are defined as three segments with polynomial and linear parts in the ideal S-curve motion input. If the S-curve is symmetrical, then $t_{acc} = t_{dec}$. In the designed S-curve, it is aimed to calculate the time parameters to obtain an optimal motion input for efficient vibration suppression. Therefore, seven segments are reduced to five segments by ignoring the linear acceleration time $t_{Lacc} = 0$ and linear deceleration time $t_{Ldec} = 0$. It is observed that the linear acceleration and deceleration parts increase in motion vibrations, so the residual vibrations increase as the increase in motion vibrations. Besides, it is aimed to minimize in-motion vibrations with this effort. In the symmetrical designed S-curve, t_m can be expressed as follows:

$$\begin{aligned} t_m &= t_{1acc} + t_{2acc} + t_{con} + t_{1dec} + t_{2dec} \\ t_{acc} &= t_{1acc} + t_{2acc} \\ t_{acc} &= t_{1dec} + t_{2dec} \end{aligned} \tag{6.2}$$

It is desired from the motion input that a system reaches a maximum velocity ω_{max} at $t = t_{acc}$. The value of t_{acc} especially affects motion vibrations of the system, while that of t_{dec} affects residual vibrations of the system (Malgaca et al., 2016). The selection of the acceleration and deceleration times is crucial to reduce the vibrations. In this thesis, a symmetrical S-Curve velocity profile is designed by considering modal properties of the manipulator for t_{acc} and t_{dec}, which are taken as $t_{1acc} = t_{2acc}$ and $t_{1dec} = t_{2dec}$. The undamped natural period is expressed as $T_{n1} = 1/f_{n1}$ where f_{n1} is the first natural frequency of the manipulator Then, t_{1h} is defined as the half of T_{n1} and used to design the time parameters of S-curve as follows:

$$t_{1h} = T_{n1}/2 \tag{6.3}$$

The time parameters are selected as $t_{1dec} = rt_{1h},\ r = 1, 2, 3...n$ (Malgaca et al., 2016). The value of r can be determined based on the length of t_m. The time parameters defined in Equation 6.2 must not be negative for any r value.

For $t_{1dec} = t_{1h}$, the designed S-curve motion input with five segments can be defined as a piecewise function as follows:

$$\omega_m(t) = \begin{cases} \omega_{1m}(t) = \alpha t^2 & 0 \le x < t_{1h} \\ \omega_{2m}(t) = -\alpha(t - 2t_{1h})^2 + 2\omega_{1m}(t_{1h}) & t_{1h} \le x < 2t_{1h} \\ \omega_{3m}(t) = \omega_{2m}(2t_{1h}) & 2t_{1h} \le x < t_m - 2t_{1h} \\ \omega_{4m}(t) = -\alpha(t - t_m + 2t_{1h})^2 + \omega_{3m}(0) & t_m - 2t_{1h} \le x < t_m - t_{1h} \\ \omega_{5m}(t) = \alpha(x - t_m)^2 & t_m - t_{1h} \le x \le t_m \end{cases} \tag{6.4}$$

The acceleration and deceleration segments have second-degree polynomial functions with a coefficient α as given in Equation 6.4. The function must be continuous and thus the final value and slope of the one function must be the same as the initial value and slope of the consecutive function. The relationships for t_{1h} are given as follows:

$$\omega_{(i)m} = \omega_{(i+1)m}(t_{1h}) \text{ for i=1, 2, 3, 4, 5} \tag{6.5}$$

$$\frac{d}{dt}\omega_{(i)m}(t_{1h}) = \frac{d}{dt}\omega_{(i+1)m}(t_{1h}) \text{ for i=1, 2, 3, 4, 5} \tag{6.6}$$

The motion input must satisfy the stopping position θ_m at $t = t_m$. Since position is integral of velocity, integrating angular velocity with time and equating it to θ_m gives the following equation to determine α.

$$\theta_m = \int_0^{t_1 h} \omega_{1m}(t)dt + \int_{t_{1h}}^{2t_{1h}} \omega_{2m}(t)dt + \int_{2t_{1h}}^{t_m - 2t_{1h}} \omega_{3m}(t)dt + \int_{t_m - 2t_{1h}}^{t_m - t_{1h}} \omega_{4m}(t)dt + \int_{t_m - t_{1h}}^{t_m} \omega_{5m}(t)dt \tag{6.7}$$

α coefficient can be calculated as follows:

$$\alpha = \frac{2\theta_m}{t_m - 2t_{1h}} \tag{6.8}$$

The parameters θ_m, t_m, and t_{1h} are inputs of the designed S-Curve motion input. Since the designed S-Curve is symmetrical, the time parameters t_{2dec} and t_{2acc} are equal to t_{1dec} and t_{1acc} and then the constant time denoted with t_{con} can be calculated as follows:

$$t_{con} = t_m - (t_{1dec} + t_{2dec}) - (t_{1acc} + t_{2acc}) \tag{6.9}$$

A MATLAB code is improved to obtain the samples of the designed S-curve angular velocity input for consideration in the experiments and mathematical models. The repeatability and dynamic performance of manipulators are significantly impacted by the payload, stopping position, and motion time. While the payload affects the natural frequencies

of the system as stated above, the motion input change depending on θ_m and t_m. In addition, each part of the designed S-curve motion input is dependent on the natural frequency. Motion inputs are created for different values of m_p, θ_m, and t_m are listed in Table 6.1.

Table 6.1 Time parameters of S-curve motion input for the SM

	m_p (kg)	$f_n(Hz)$	$\theta_m(^\circ)$	$t_m(s)$	$t_{acc}(s)$	$t_{con}(s)$	$t_{dec}(s)$
SM-M1a	0.62	6.42	30	1	0.1	0.8	0.1
					0.1558	0.6885	0.1558
					0.3115	0.3769	0.3115
					0.4673	0.0654	0.4673
SM-M1b	1.24	4.86	30	1	0.1	0.8	0.1
					0.2058	0.5885	0.2058
					0.4115	0.1770	0.4115
SM-M2a	0.62	6.42	30	2	0.1	1.8	0.1
					0.1558	1.6885	0.1558
					0.3115	1.3769	0.3115
					0.4673	1.0654	0.4673
					0.6231	0.7539	0.6231
SM-M2b	1.24	4.86	30	2	0.1	1.8	0.1
					0.2058	1.5885	0.2058
					0.4115	1.1770	0.4115
					0.6173	0.7654	0.6173
					0.8230	0.3539	0.8230
SM-M3a	0.62	6.42	45	1	0.1	0.8	0.1
					0.1558	0.6885	0.1558
					0.3115	0.3769	0.3115
					0.4673	0.0654	0.4673
SM-M3b	1.24	4.86	45	1	0.1	0.8	0.1
					0.2058	0.5885	0.2058
					0.4115	0.1770	0.4115
SM-M4a	0.62	6.42	45	2	0.1	1.8	0.1
					0.1558	1.6885	0.1558
					0.3115	1.3769	0.3115
					0.4673	1.0654	0.4673
					0.6231	0.7539	0.6231
SM-M4b	1.24	4.86	45	2	0.1	1.8	0.1
					0.2058	1.5885	0.2058
					0.4115	1.1770	0.4115
					0.6173	0.7654	0.6173
					0.8230	0.3539	0.8230

The S-curve motion inputs are generated with combination of two different stopping positions $\theta_m = 30^\circ$ and $\theta_m = 45^\circ$ and two different motion time $t_m = 1$ s and $t_m = 2$ s. Besides,

the effect of the mass is examined with payloads m_p = 0.62 kg and m_p = 1.24 kg. In SM-M1 and SM-M2, the fast and slow reaching of the manipulator to the same stopping position with two different payloads are examined. SM-M3 and SM-M4 are similar to SM-M1 and SM-M2 considering a different stopping position. SM-M1, SM-M2, SM-M3 and SM-M4 include sub-cases involve the variation of the payload.

6.2.2 Vibration Responses for S-curve Motion Input

The vibration responses measured from the experimental system and obtained from the identified models are compared for the identification and validation datasets. The identification responses are obtained for t_{dec} = 0.1 s, which is the uncontrolled case, while the validation responses are obtained for different t_{dec} values to suppress the vibrations of the SM. Vibration responses for SM-M1a and SM-M3a with sub-cases are shown in Figures 6.2 and 6.3.

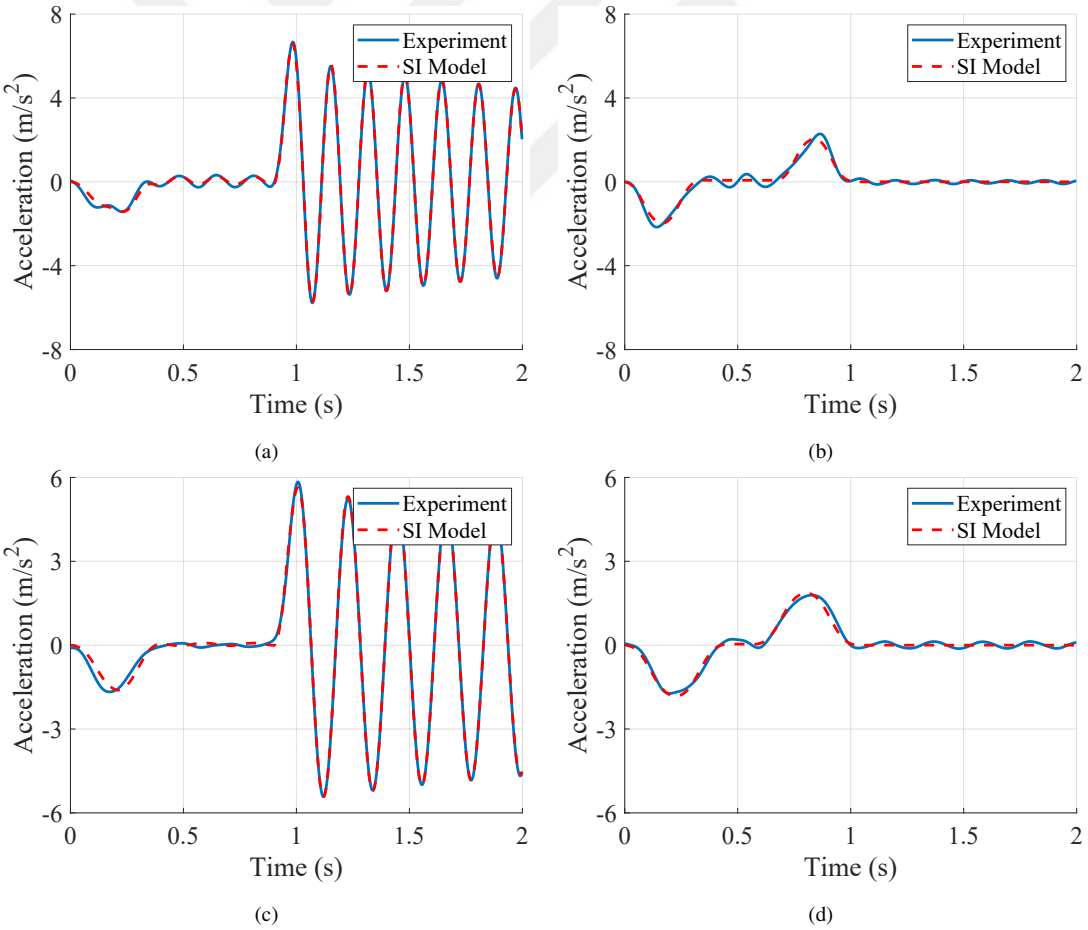


Figure 6.2 Vibration responses: (a) SM-M1a t_{dec}=0.1 s (b) SM-M1a t_{dec}=2t_{1h} s (c) SM-M1b t_{dec}=0.1 s (d) SM-M1b t_{dec}=2t_{1h} s

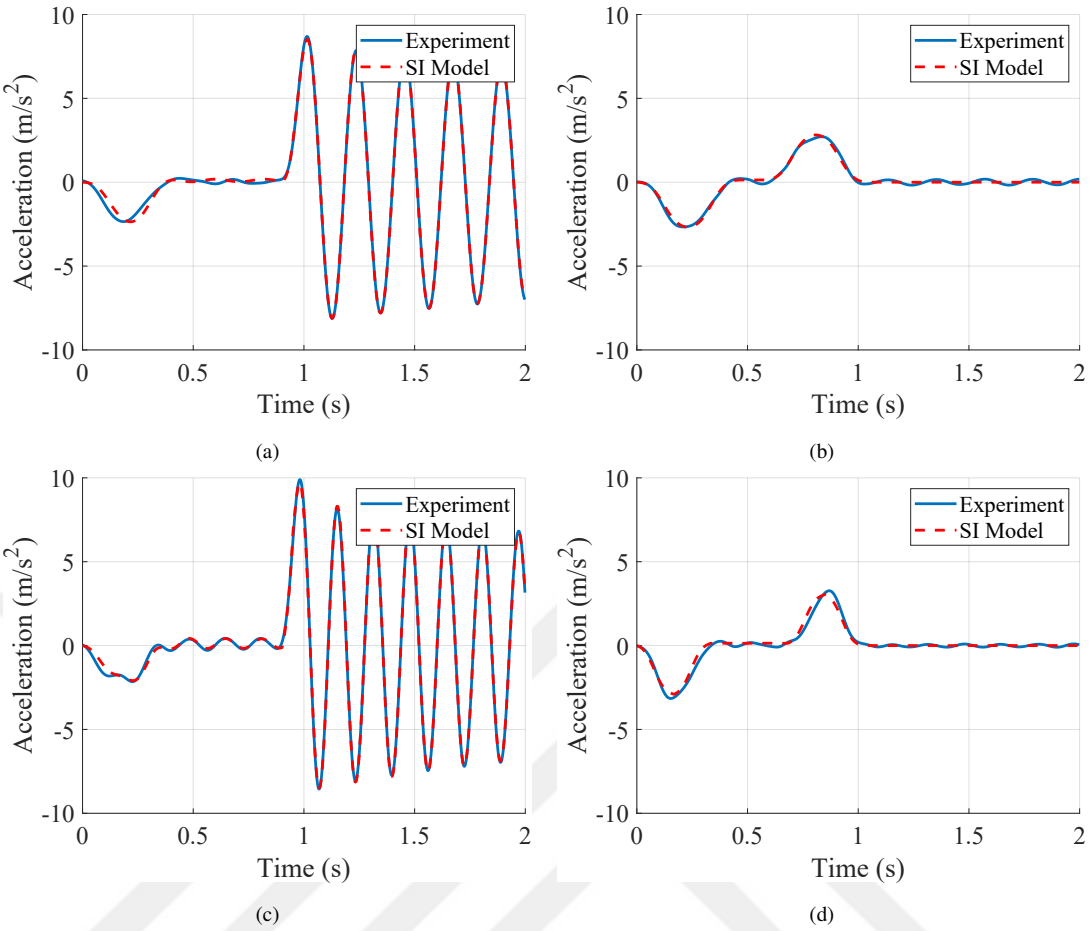


Figure 6.3 Vibration responses: (a) SM-M3a t_{dec}=0.1 s (b) SM-M3a t_{dec}=2t_{1h} s (c) SM-M3b t_{dec} =0.1 s (d) SM-M3b t_{dec}=2t_{1h} s

It is observed from Figures 6.2 and 6.3 that the vibration responses obtained from the identified model of the manipulator match the experimental vibration responses well for the identification and validation. The vibration amplitudes shown in Figures 6.2a, 6.3c, 6.2c, and 6.3a are the highest for identification results to accurately identify the SM. These vibration responses are called uncontrolled responses for comparison of vibration control results. The vibration amplitudes shown in Figures 6.2b, 6.3d, 6.2d, and 6.3b corresponding to the validation results are successfully suppressed for $t_{dec} = 2t_{1h}$. These vibration responses are called controlled responses.

It is difficult to comment on vibration results over time responses. Therefore, the performance of the designed S-curve motion can be evaluated with the RMS values of time signals and reduction ratios which are calculated from the RMS values for different t_{dec} values according to the uncontrolled responses considered in each case. The RMS values and

reduction ratios of the residual vibrations are presented in Table 6.2.

Table 6.2 RMS and reduction ratios for S-curve velocity profile

Cases	t_{dec} (s)	RMS (m/s^2)		Reduction (%)	
		Experiment	SI	Experiment	SI
SM-M1a	0.1	2.638	2.633	-	-
	$1t_{1h}$	0.7977	1.009	69.76	61.69
	$2t_{1h}$	0.0558	0.0012	97.88	99.96
	$3t_{1h}$	0.1484	0.1687	94.38	93.59
SM-M1b	0.1	2.788	2.786	-	-
	$1t_{1h}$	2.306	2.284	17.29	18.03
	$2t_{1h}$	0.0749	0.0049	97.31	99.83
SM-M2a	0.1	1.357	1.097	-	-
	$1t_{1h}$	1.252	0.781	7.73	28.81
	$2t_{1h}$	0.0719	0.0005	94.7	99.96
	$3t_{1h}$	0.1551	0.1019	88.57	90.71
	$4t_{1h}$	0.0603	0.0002	95.56	99.98
SM-M2b	0.1	1.341	1.178	-	-
	$1t_{1h}$	1.208	0.6363	56.66	77.16
	$2t_{1h}$	0.0518	0.0017	98.14	99.94
	$3t_{1h}$	0.1919	0.1006	93.12	96.39
	$4t_{1h}$	0.0236	0.0011	99.15	99.96
SM-M3a	0.1	3.939	3.936	-	-
	$1t_{1h}$	1.104	1.292	71.97	67.18
	$2t_{1h}$	0.0591	0.006	98.5	99.85
	$3t_{1h}$	0.238	0.2272	93.96	94.23
SM-M3b	0.1	4.124	4.122	-	-
	$1t_{1h}$	3.126	3.456	24.19	16.16
	$2t_{1h}$	0.1044	0.0033	97.47	99.92
SM-M4a	0.1	2.045	1.652	-	-
	$1t_{1h}$	1.789	1.009	12.54	38.94
	$2t_{1h}$	0.1052	0.0024	94.85	99.85
	$3t_{1h}$	0.2922	0.1338	85.71	91.9
	$4t_{1h}$	0.0326	0.0008	98.41	99.95
SM-M4b	0.1	1.83	1.741	-	-
	$1t_{1h}$	1.589	0.8469	13.16	51.36
	$2t_{1h}$	0.105	0.0007	94.26	99.96
	$3t_{1h}$	0.3258	0.1386	82.19	92.04
	$4t_{1h}$	0.0603	0.0011	96.7	99.94

For S-Curve motion inputs in Table 6.2, t_{dec} = 0.1 s corresponds to uncontrolled cases. For passive vibration control, the values of t_{dec} are determined according to r values. The values of t_{dec} 0.1558 s, 0.3115 s, 0.4673 s, 0.6231 s for Cases a, while 0.2058 s, 0.4115 s, 0.6173 s, 0.8230 s for Cases b are the controlled results, corresponding to r = 2, 4, 6, and 8, respectively. It is observed from Figures 6.2b, 6.3d, 6.2d, and 6.3b and Table 6.2 that the passive vibration control of the manipulator is successfully achieved for $r > 2$.

Since the motion time is insufficient, some results are obtained up to $r = 6$ in SM-M1a and SM-M3a and up to $r = 4$ in SM-M1b and SM-M3b. The results are presented up to $r = 8$ for other cases.

As seen from Table 6.2, the experimental results match the SI results well in uncontrolled responses. The vibration amplitudes of the uncontrolled responses increase as the payload and stopping position increase for the same motion time.

For example, due to the payload increase in SM-M1, the RMS values increase from 2.638 m/s^2 to 2.788 m/s^2 and 2.633 m/s^2 to 2.786 m/s^2 for the experiment and CTSI, respectively. With increasing the stopping position in SM-M3, the RMS values increase from 3.939 m/s^2 to 4.124 m/s^2 and 3.936 m/s^2 to 4.122 m/s^2 for the experiment and SI, respectively. It is observed that the RMS values of uncontrolled responses in SM-M3 and SM-M4 decrease significantly as the motion time increases.

As seen in Table 6.2 for $r = 2$, even if the vibrations are suppressed in SM-M1a and SM-M3a, this is unsatisfactory enough in other cases. It is observed that passive vibration control has been successfully performed and the reduction ratios are well matched for $r > 2$ in all cases. The error values of the reduction ratios obtained from the experimental system and the identified model can be evaluated. For $r > 2$, the maximum error values corresponding to SM-M1, SM-M2, SM-M3 and SM-M4 are calculated as 4.29%, 5.55%, 2.52%, and 11.98%, respectively. The error value of the reduction ratios is generally below 12% for all cases and the residual vibrations of the manipulator are reduced up to 99.15% in the experimental system, while those are reduced up to 99.98% in the identified model.

6.3 Optimization of Motion Input with Genetic Algorithm

In this subsection, the optimization of a velocity profile to vibration control of the manipulator with the GA is described in detail. The flowchart of the optimization of the time parameters with the GA is shown in Figure 6.4.

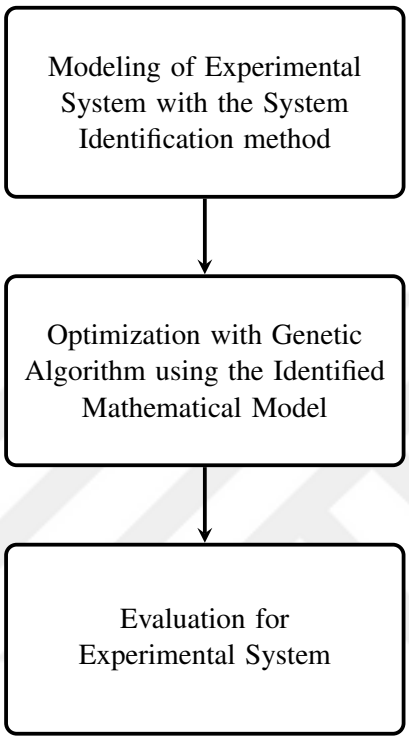


Figure 6.4 Flowchart of the proposed control method

The optimization approach involves three main steps. In the first step, the manipulator is modeled using SI methods, and the details of this process are provided in Chapters 4 and 5. In the second step, the time parameters of the motion profile are optimized using the identified mathematical models of the manipulator. For this purpose, the GA is employed to perform the optimization process. Subsequently, the optimized motion profile with the obtained time parameters is used to suppress the unwanted vibrations of the manipulator.

Obtaining the mathematical models with the SI method, the process is sped up considerably. For instance, when 30 populations and 30 generations are selected for optimization, the time parameters obtained should be evaluated 900 times. Implementing the optimization in a simulation like ANSYS or experimentally is a challenging process.

6.3.1 Flowchart of Genetic Algorithm

In this subsection, the GA and its implementation are described indeed. The GA is an optimization method that is improved inspired by Darwinian theory of evolutionary (Sivanandam & N., 2007; Kramer, 2017). The flowchart of the GA method is shown in Figure 6.5.

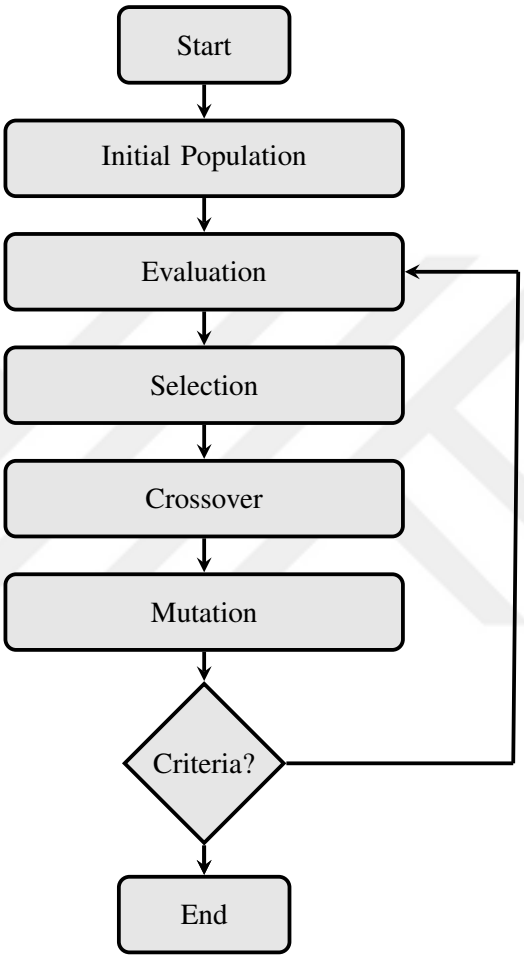


Figure 6.5 Genetic algorithm flowchart

The GA method consists of three steps: selection, crossover, and mutation. The selection operator is the process of choosing individuals from the population to become parents of the next generation. There are different selection types such as rank selection, roulette wheel selection, tournament selection, elite selection, and Boltzmann selection (Sivanandam & N., 2007; Kramer, 2017). The roulette wheel selection type, where individuals are determined based on their fitness score, and the probability of selection is proportional to their fitness, is used in this thesis.

The second evolutionary operator is crossover. After the selection step, the next generation is created with crossover. Two of popular crossover techniques in the literature are single-point crossover and double-point crossover. The chromosomes of two parents are swapped before and after a single point in the single-point crossover, whereas there are two crossover points, and the chromosomes between the points are swapped in the double-point crossover (Sivanandam & N., 2007; Kramer, 2017). The single-point and double-point crossovers are shown in Figure 6.6.

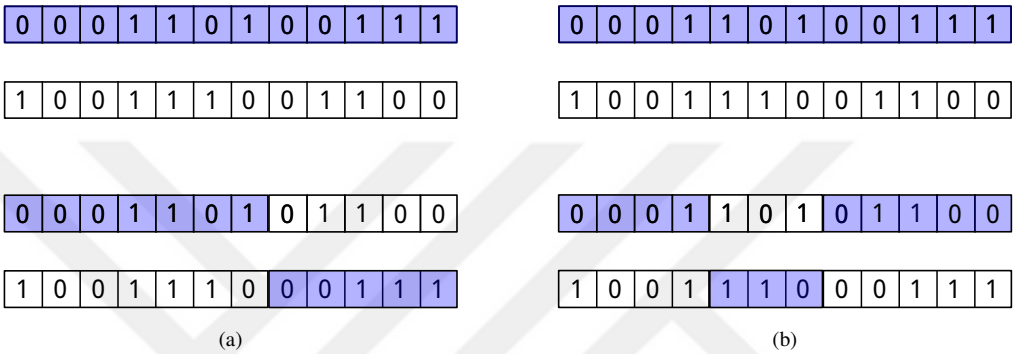


Figure 6.6 Crossover (a) single-point (b) double-point

In the mutation step, the genotype of the individual is randomly changed. The mutation step plays an important role in preserving genetic diversity within the population and preventing premature convergence towards an unsatisfactory solution (Sivanandam & N., 2007; Kramer, 2017).

Some of the most used mutation types are gaussian, power mutation, unifor, non-uniform. A random number from a Gaussian distribution with 0 mean is added to the next generation in the gaussian mutation. An example of the mutation operator is shown in Figure 6.7.

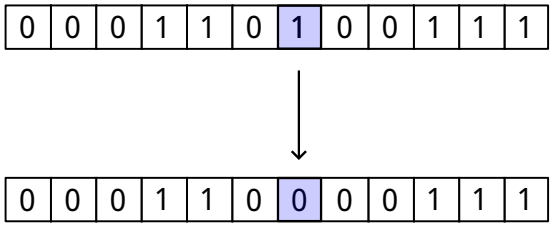


Figure 6.7 An example for mutation operator

The thesis aims to optimize the time parameters of the trapezoidal motion input, namely t_{acc}, t_{con}, and t_{dec}, in order to reduce residual vibrations. To achieve this, linear equality constraints are defined as the sum of the time parameters, which must be equal to the motion time. Additionally, lower and upper bounds are set to ensure that the time parameters must be positive throughout the optimization process. Linear equality, lower and upper bounds of optimization are given as follows:

$$\begin{aligned} &t_{acc} + t_{con} + t_{dec} = t_m \\ &0 < t_{acc} < t_m \\ &0 < t_{con} < t_m \\ &0 < t_{dec} < t_m \end{aligned} \tag{6.10}$$

Two fitness functions are selected to evaluate the quality of the solutions: the RMS and maximum values of the residual vibration signals. These fitness functions are used to search for minimizing residual vibrations. However, the best result is obtained for the RMS as the fitness function.

Initial population size and maximum generation parameters are selected as 30 and 30, respectively. When the initial population size is selected large, the probability of catching the global minimum increases. On the other hand, the processing time of the algorithm also increases as the initial population size increases.

Since composite manipulators are more flexible than steel manipulators, the optimization method is employed to suppress the vibrations of two epoxy-glass composite manipulators with different lay-ups.

The best and mean of the population values for EGM-a and EGM-b are shown in Figure 6.8 for the RMS as the fitness function.

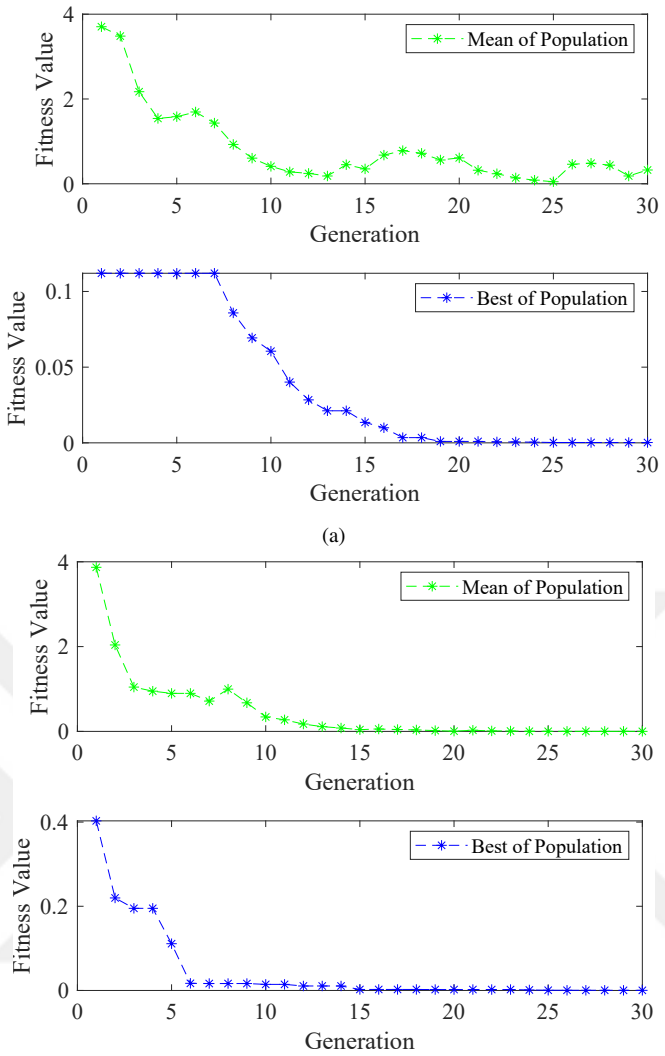


Figure 6.8 The best and mean of population of (a) EGM-a (b) EGM-b

In Figure 6.8, the mean of the population describes the average fitness value of each generation, whereas the best of the population describes the minimum fitness value for each generation. As shown in Figure 6.8, the best fit is obtained at 20 generations for both manipulators. The optimum time parameters are found as t_{acc} = 0.972 s, t_{con} = 0.0572 s and t_{dec} = 0.9705 s for the EGM-a and t_{acc} = 0.6721 s, t_{con} = 0.6306 s and t_{dec} = 0.6969 s for EGM-b. The optimum time parameters are applied to the experimental system to reduce the residual vibrations of the manipulator.

Residual vibration responses of the optimization method are compared with the classical trapezoidal and the designed S-curve motion inputs to evaluate the effectiveness of the optimization method. The vibration amplitudes of the flexible manipulators were suppressed by the trapezoidal (Malgaca et al., 2016) and triangular (Ankaralı et al., 2012; Malgaca et al., 2016) motion inputs. In (Malgaca et al., 2016), the deceleration time of the trapezoidal motion input is selected as $t_{dec} = 1t_{1h}$ for the uncontrolled vibration response, while that of the trapezoidal motion input is selected as $t_{dec} = 2t_{1h}$ for the controlled vibration response. Also, the deceleration time of the designed S-curve motion input is determined as $t_{dec} = 2t_{1h}$.

The classical trapezoidal, the designed S-curve and the optimized trapezoidal motion inputs are created for two stopping position are listed in Table 6.3.

Table 6.3 Time parameters of motion inputs for the EGM-a and EGM-b

Cases	Motion Profile	$\theta_m(^\circ)$	$t_m(s)$	$t_{acc}(s)$	$t_{con}(s)$	$t_{dec}(s)$
EGMa-M1	Trapezoidal	30	2	1.2925	0.4717	0.2358
	Trapezoidal			1.0566	0.4717	0.4717
	S-curve			0.5849	0.4717	0.9434
	Trapezoidal with GA			0.9720	0.0572	0.9705
EGMa-M2	Trapezoidal	60	2	1.2925	0.4717	0.2358
	Trapezoidal			1.0566	0.4717	0.4717
	S-curve			0.5849	0.4717	0.9434
	Trapezoidal with GA			0.9720	0.0572	0.9705
EGMb-M1	Trapezoidal	30	2	1.3421	0.4386	0.2193
	Trapezoidal			1.1228	0.4386	0.4386
	S-curve			0.6842	0.4386	0.8772
	Trapezoidal with GA			0.6721	0.6306	0.6969
EGMb-M2	Trapezoidal	60	2	1.3421	0.4386	0.2193
	Trapezoidal			1.1228	0.4386	0.4386
	S-curve			0.6842	0.4386	0.8772
	Trapezoidal with GA			0.6721	0.6306	0.6969

In Table 6.3, EGMa-M1 and EGMa-M2 denote the motion inputs of the EGM-a for $\theta_m = 30^\circ$ and $\theta_m = 60^\circ$, while EGMb-M1 and EGMb-M2 present the motion inputs of the EGM-b for $\theta_m = 30^\circ$ and $\theta_m = 60^\circ$, respectively.

6.3.2 Vibration Responses for the Optimization

The vibration responses measured from the experimental system and obtained from the identified models are compared for Trapezoidal, the designed S-curve and the optimized Trapezoidal motion inputs are shown in Figure 6.9 for the EGM-a and the EGM-b.

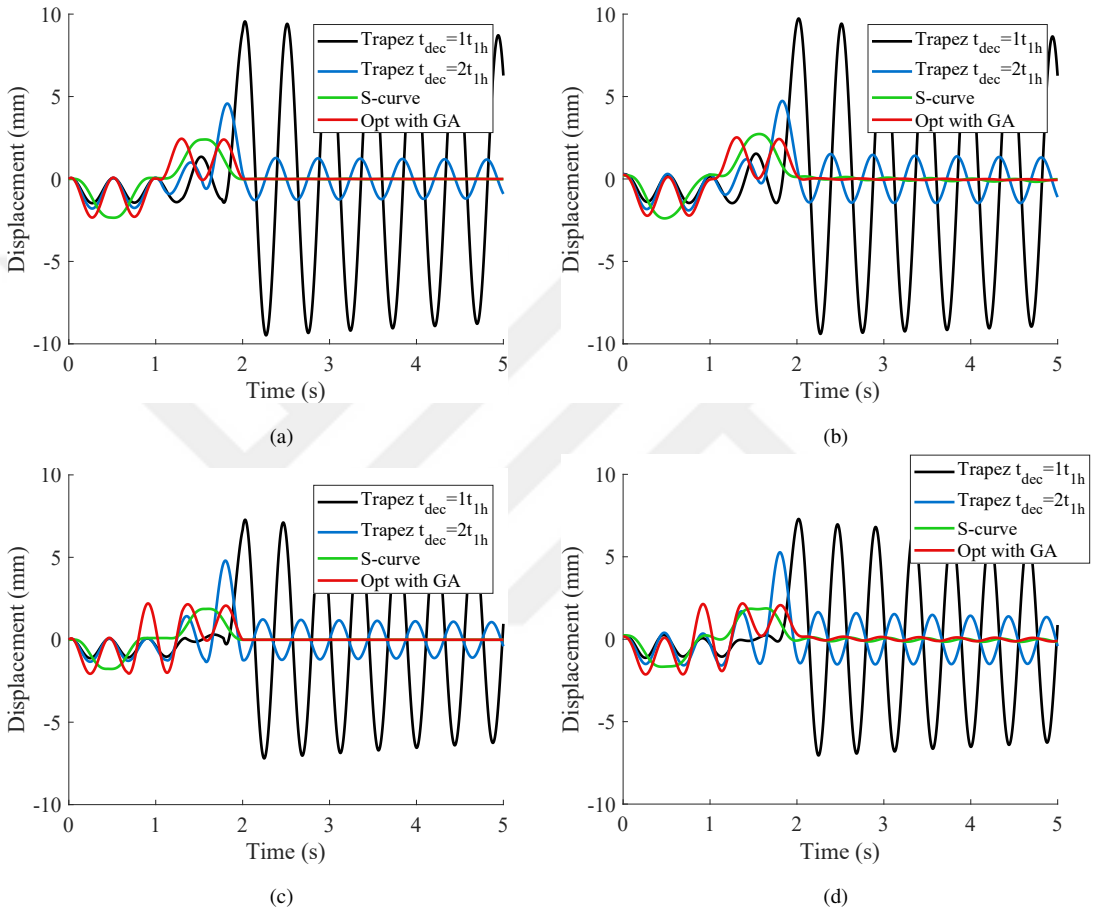


Figure 6.9 Vibration responses for (a) and (b) EGMa-M1 (c) and (d) EGMb-M1

Figures 6.9a and 6.9c show residual vibration responses obtained from the identified model for EGM-a and EGM-b, whereas Figures 6.9b and 6.9d show residual vibration responses measured from the experimental system for EGM-a and EGM-b, respectively. The residual vibrations of EGM-a and EGM-b are suppressed more successfully than the classical trapezoidal profile in (Malgaca et al., 2016) with the optimization method and the designed S-curve motion input.

It is difficult to comment on vibration results over time responses. Therefore, the performance of the optimization with the GA can be evaluated with the RMS values of time signals and reduction ratios which are calculated from the RMS values for different t_{dec} values according to the uncontrolled responses considered in each case. The RMS values and reduction ratios for the EGM-a and the EGM-b are listed in Table 6.4.

Table 6.4 RMS and reduction ratios for the EGM-a and EGM-b

		RMS (mm)		Reduction (%)	
Cases	Motion Profile	SI	Experiment	SI	Experiment
EGMa-M1	Trapezoidal	6.5204	6.0013	-	-
	Trapezoidal	0.8624	0.9342	86.7742	84.4340
	S-curve	0.0090	0.1023	99.8615	98.2958
	Trapezoidal with GA	0.0005	0.0496	99.9920	99.1742
EGMa-M2	Trapezoidal	13.0409	11.5149	-	-
	Trapezoidal	1.7248	1.7181	86.7742	85.0789
	S-curve	0.0181	0.1820	99.8615	98.4192
	Trapezoidal with GA	0.0010	0.1294	99.9920	98.8759
EGMb-M1	Trapezoidal	4.7849	4.0699	-	-
	Trapezoidal	0.8158	0.9307	82.9509	77.1328
	S-curve	0.0002	0.0872	99.9956	97.8579
	Trapezoidal with GA	0.0004	0.0825	99.9918	97.9739
EGMb-M2	Trapezoidal	9.5699	8.2149	-	-
	Trapezoidal	1.6316	1.5908	82.9509	80.6358
	S-curve	0.0004	0.1436	99.9956	98.2520
	Trapezoidal with GA	0.0008	0.2084	99.9918	97.4627

In Table 6.4, RMS values and reduction ratios for stopping positions 30° and 60° are listed, respectively. For EGM-a, reduction ratios obtained from the identified model and experimental vibration responses are 99.99% and 99.17%, respectively, for 30° stopping position. For EGM-b, reduction ratios obtained from simulation and experimental vibration responses are 99.99% and 97.97% for 30° stopping position, respectively. For all cases, the residual vibrations are suppressed by more than 97.46% reduction ratio.

CHAPTER SEVEN
CONCLUSIONS

In this thesis, modeling and passive vibration control of single-link flexible manipulators are studied with different identification methods and motion inputs. Four identification methods such as the ARX, CTSI, N4SID and SSEST methods are utilized to identify the manipulators made of steel and composite materials.

Firstly, the identification of the four-dof mass-damper-spring system is studied. A numerical dataset for the identification is obtained from the FE model of the mechanical system. Four transfer functions for the mechanical system are successfully identified with the CTSI method using step response as an identification dataset.

An experimental system is set up to estimate mathematical models of the single-link manipulators. Also, the FE model of the SM is established to investigate the performance and repeatability of the experimental system. The measured vibration responses match well with the vibration responses obtained from the FE model of the SM for the acceleration and displacement signals.

Using the input and output signals obtained from the FE model and experimental system, the mathematical models of the SM are identified with the ARX, CTSI, SSEST and N4SID methods for two payloads and three output types. Four identification methods identified the mathematical models of the manipulator with over 90% success for different case studies. However, especially the CTSI and N4SID methods are more successful in the identification of the SM. As the vibration responses obtained from the FE model of the SM are not affected by noise, identification results for the simulation dataset are more successful than identification results for experimental signals. Besides, according to the identified natural frequencies and damping ratios, the best identification results are obtained for the acceleration signals as the output type. Identification of the epoxy-carbon and the epoxy-glass manipulators with different lay-ups are studied with the CTSI and N4SID methods using knowledge of the modeling of the SM. Three composite manipulators are successfully identified with two different payloads.

In this thesis, the residual vibrations of the manipulators made of steel and composite materials are reduced with the designed S-curve and the optimized Trapezoidal motion inputs. While an ideal S-curve motion input has seven segments, the designed S-curve is developed with five segments excluding linear acceleration and deceleration times. To evaluate the performance of the designed S-curve motion input, different deceleration times denoted with t_{dec} are considered for the comparison of different stopping positions, motion times and payloads. The highest residual vibrations are measured for the deceleration time $t_{dec} = 0.1s$, which is called an uncontrolled case. For $t_{dec} = 2t_{1h}$ and $t_{dec} = 4t_{1h}$, the residual vibrations of the SM are reduced with reduction ratios of 99%. For $t_{dec} = 1t_{1h}$, the reduction ratios are calculated between 16.16-71.16%, while the reduction ratios are calculated between 90.71-96.39% for $t_{dec} = 3t_{1h}$, respectively. As a result, it is observed that residual vibrations are sufficiently suppressed with $t_{dec} = 3t_{1h}$. However, the residual vibrations of the SM are more efficiently suppressed for the double values of the deceleration time.

The time parameters of the trapezoidal motion input are optimized with the GA approach to reduce residual vibrations of the composite manipulators. The RMS and maximum values of the residual vibrations are selected as the fitness function and the best results are obtained for the RMS values as the fitness function. The time parameters optimized with the GA method are tested with the identified transfer functions for providing the minimum RMS value of the residual vibrations and the reduction ratios are obtained from the identified model for two epoxy-glass manipulators over 99.99%. The optimized time parameters are utilized in the experimental system and the experimental residual vibrations of the two composite manipulators are reduced with reduction ratios of 97.46%.

In future work, several directions can be studied. Active vibration control can be studied with the identified mathematical models of the manipulator. The modeling of multi-link manipulators can be studied with identification methods.

REFERENCES

Abreu, G. L., Conceição, S. M. d., Lopes Jr, V., Brennan, M. J., Alves, M. T. S., et al. (2012a). System identification and active vibration control of a flexible structure. *Journal of the Brazilian Society of Mechanical Sciences and Engineering*, *34*(SPE), 386–392.

Abreu, G. L., Conceição, S. M. d., Lopes Jr, V., Brennan, M. J., Alves, M. T. S., et al. (2012b). System identification and active vibration control of a flexible structure. *Journal of the Brazilian Society of Mechanical Sciences and Engineering*, *34*, 386–392.

Ankaralı, A., Mecitoğlu, Z., & Diken, H. (2012). Response spectrum of a coupled flexible shaft-flexible beam system for cycloidal input motion. *Mechanism and Machine Theory*, *47*, 89–102.

ANSYS Inc. (2012). ANSYS Mechanical APDL Verification Manual. *ANSYS, Inc.*, *15317*(October), 724–746.

Banazadeh, A., Nobahari, H., & Seifouripour, Y. (2019). Identification of state space dynamics of a fixed-wing aerial vehicle with neural networks using flight test data. *Sharif Journal of Mechanical Engineering*, *35*(1), 13–22.

Bathelt, A., & Jelali, M. (2014). Comparative study of subspace identification methods on the tennessee eastman process under disturbance effects. *Idea*, *100*, 31–36.

Benyamin, R. B., Nugroho, M. A. A., Sepri, A. Y., Trilaksono, B. R., & Moelyadi, A. (2017). Dynamic modeling using system identification and attitude control design of ganefly flapping wings micro aerial vehicle (fwmav). In *2017 7th IEEE International Conference on System Engineering and Technology (ICSET)*, *IEEE*, 200–205.

Borjas, S., & Garcia, C. (2011). Subspace identification for industrial processes. *TEMA (São Carlos)*, *12*, 183–194.

Bu, X., Ye, L., Su, Z., & Wang, C. (2003). Active control of a flexible smart beam using a system identification technique based on armax. *Smart materials and Structures*, *12*(5), 845.

Chang, M., & Pakzad, S. N. (2014). Observer kalman filter identification for output-only systems using interactive structural modal identification toolsuite. *Journal of Bridge Engineering*, *19*(5), 04014002.

Chen, T., Lou, J., Yang, Y., Ma, J., Li, G., & Wei, Y. (2018). Auto-regressive moving average with exogenous excitation model based experimental identification and optimal discrete multi-poles shifting control of a flexible piezoelectric manipulator. *Journal of Vibration and Control*, *24*(24), 5707–5725.

Choubey, C., & Ohri, J. (2021). Gwo-based tuning of lqr-pid controller for a 3-dof parallel manipulator. *IETE Journal of Research*, 1–16.

Costa, A. G., Maldonado, J. L. B., Romero, F. A., Sanmartín, J. C., Valarezo, M., & Castillo, H. (2017). N4sid method applied to obtain a discrete-time linear state space system as a mathematical model of a jaw crusher prototype. In *2017 CHILEAN Conference on Electrical, Electronics Engineering, Information and Communication Technologies (CHILECON)*, *IEEE*, 1–6.

Dong, X.-J., Meng, G., & Peng, J.-C. (2006). Vibration control of piezoelectric smart structures based on system identification technique: Numerical simulation and experimental study. *Journal of Sound and Vibration*, *297*(3-5), 680–693.

Douat, L. R., Queinnec, I., Garcia, G., Michelin, M., Pierrot, F., & Tarbouriech, S. (2013). Identification and vibration attenuation for the parallel robot par2. *IEEE Transactions on Control Systems Technology*, *22*(1), 190–200.

Fang, Y., Hu, J., Liu, W., Shao, Q., Qi, J., & Peng, Y. (2019). Smooth and time-optimal s-curve trajectory planning for automated robots and machines. *Mechanism and Machine Theory*, *137*, 127–153.

Favoreel, W., De Moor, B., & Van Overschee, P. (2000a). Subspace state space system identification for industrial processes. *Journal of Process Control*, *10*(2-3), 149–155.

Favoreel, W., De Moor, B., & Van Overschee, P. (2000b). Subspace state space system identification for industrial processes. *Journal of process control*, *10*(2-3), 149–155.

Favoreel, W., Van Huffel, S., De Moor, B., Sima, V., & Verhaegen, M. (1999). Comparative study between three subspace identification algorithms. In *1999 European Control Conference (ECC)*, *IEEE*, 821–826.

Gagg F, L., Da Conceição, S., Vasques, C., De Abreu, G., Lopes, V., Brennan, M., et al.

(2014). Experimental identification and control of a cantilever beam using era/okid with a lqr controller. *Journal of Control, Automation and Electrical Systems*, *25*(2), 161–173.

Garnier, H., & Liuping, W. (2008). *Identification of Continuous-time Models from Sampled Data*. Springer London.

Garnier, H., Mensler, M., & Richard, A. (2003). Continuous-time model identification from sampled data: implementation issues and performance evaluation. *International journal of Control*, *76*(13), 1337–1357.

Gautier, G., Serra, R., & Mencik, J.-M. (2013). Vibratory diagnosis by finite element model updating and operational modal analysis. *Mechanics & Industry*, *14*(2), 145–149.

Guida, D., Nilvetti, F., & Pappalardo, C. M. (2009). Parameter identification of a two degrees of freedom mechanical system. *International Journal of Mechanics*, *3*(2), 23–30.

Gumussoy, S., Ozdemir, A. A., McKelvey, T., Ljung, L., Gibanica, M., & Singh, R. (2018). Improving linear state-space models with additional iterations. *IFAC-PapersOnLine*, *51*(15), 341–346.

Ha, C.-W., Rew, K.-H., & Kim, K.-S. (2012). Robust zero placement for motion control of lightly damped systems. *IEEE Transactions on Industrial Electronics*, *60*(9), 3857–3864.

Heredia, G., & Ollero, A. (2009). Sensor fault detection in small autonomous helicopters using observer/kalman filter identification. In *2009 IEEE International Conference on Mechatronics*, *IEEE*, 1–6.

Heredia, G., & Ollero, A. (2011). Detection of sensor faults in small helicopter uavs using observer/kalman filter identification. *Mathematical Problems in Engineering*, *2011*, 1–20.

Jaen-Cuellar, A. Y., de J. Romero-Troncoso, R., Morales-Velazquez, L., & Osornio-Rios, R. A. (2013). Pid-controller tuning optimization with genetic algorithms in servo systems. *International Journal of Advanced Robotic Systems*, *10*(9), 324.

Juang, J.-N., & Phan, M. Q. (2001). *Identification and control of mechanical systems*. Cambridge University Press.

Junior, A. C., Riul, J. A., & Montenegro, P. H. M. (2016). Application of the subspace identification method using the n4sid technique for a robotic manipulator. *IEEE Latin America Transactions*, *14*(4), 1588–1593.

Juricek, B. C., Seborg, D. E., & Larimore, W. E. (2001). Identification of the tennessee eastman challenge process with subspace methods. *Control Engineering Practice*, *9*(12), 1337–1351.

Kankashvar, M. R., Kharrati, H., Asl, R. M., & Sadeghiani, A. B. (2015). Designing pid controllers for a five-bar linkage robot manipulator using bbo algorithm. In *2015 6th international conference on modeling, simulation, and applied optimization (ICMSAO)*, *IEEE*, 1–6.

Keesman, K. J. (2011). *System identification: an introduction*. Springer.

Kim, Y.-M. (2013). Comparison of subspace-based system identification techniques. In *2013 13th International Conference on Control, Automation and Systems (ICCAS 2013)*, *IEEE*, 741–746.

Kramer, O. (2017). *Genetic Algorithm Essentials*. Springer Cham.

Li, H., Le, M., Gong, Z., & Lin, W. (2009). Motion profile design to reduce residual vibration of high-speed positioning stages. *IEEE/ASME Transactions On Mechatronics*, *14*(2), 264–269.

Little, J. A., & Mann, B. P. (2019). Optimizing logarithmic decrement damping estimation through uncertainty propagation. *Journal of Sound and Vibration*, *457*, 368–376.

Liu, C., & Chen, Y. (2018). Combined s-curve feedrate profiling and input shaping for glass substrate transfer robot vibration suppression. *Industrial Robot: An International Journal*, *45*(4), 549–560.

Ljung, L. (1999). *System identification theory for the user*. Prentice-Hall.

Ljung, L., Singh, R., & Chen, T. (2015). Regularization features in the system identification toolbox. *IFAC-PapersOnLine*, *48*(28), 745–750.

Łuczak, D., & Nowopolski, K. (2014). Identification of multi-mass mechanical systems in electrical drives. In *Proceedings of the 16th International Conference on Mechatronics-Mechatronika 2014*, *IEEE*, 275–282.

Malgaca, L., Lök, S., & Uyar, M. (2019). Suppression of pitch angle vibrations of a 5-dof half vehicle model by system identification method. *Internatıonal Journal of Natural and Engineering Sciences*, *13*(2), 49–52.

Malgaca, L., & Lök, Ş. İ. (2022). Measurement and modeling of a flexible manipulator for vibration control using five-segment s-curve motion. *Transactions of the Institute of Measurement and Control*, *44*(8), 1545–1556.

Malgaca, L., Lök, Ş. İ., & Uyar, M. (2020). Modeling and vibration reduction of a flexible planar manipulator with experimental system identification. *methods*, *5*, 6.

Malgaca, L., & Lök, S. I. (2017). L-çerçevenin sistem tanımlama yöntemi ile titreşimi analizi. In *18. Ulusal Makina Teorisi Sempozyumu*, vol. 1, 22–27.

Malgaca, L., Yavuz, Ş., Akdağ, M., & Karagülle, H. (2016). Residual vibration control of a single-link flexible curved manipulator. *Simulation Modelling Practice and Theory*, *67*, 155–170.

Meirovitch, L. (1986). Elements of vibration analysis((book)). *New York, McGraw-Hill Book Co., 1986, 574*.

Meirovitch, L. (2000). *Fundamentals of vibrations/meirovitch, l.*

Mimmi, G., & Pennacchi, P. (2001). Pre-shaping motion input for a rotating flexible link. *International Journal of Solids and Structures*, *38*(10-13), 2009–2023.

Nguyen, K. D., Ng, T.-C., & Chen, I.-M. (2008). On algorithms for planning s-curve motion profiles. *International Journal of Advanced Robotic Systems*, *5*(1), 11.

Nguyen, Q.-C., Vu, V.-H., & Thomas, M. (2022). A kalman filter based arx time series modeling for force identification on flexible manipulators. *Mechanical Systems and Signal Processing*, *169*, 108743.

Ni, Z., Wu, S., Zhang, Y., & Wu, Z. (2020). Payload parameter identification of a flexible space manipulator system via complex eigenvalue estimation. *International Journal of Aerospace Engineering*, *2020*, 1–17.

Ozdemir, A. A., & Gumussoy, S. (2017). Transfer function estimation in system identification toolbox via vector fitting. *IFAC-PapersOnLine*, *50*(1), 6232–6237.

Pappalardo, C. M., Califano, F., Lok, S. I., & Guida, D. (2023a). A systematic computational and experimental study of the principal data-driven identification procedures. part i:

Analytical methods and computational algorithms. *Journal of Applied and Computational Mechanics*, *9*(2), 529–549.

Pappalardo, C. M., Califano, F., Lok, S. I., & Guida, D. (2023b). A systematic computational and experimental study of the principal data-driven identification procedures. part ii: Numerical analysis and experimental testing. *Journal of Applied and Computational Mechanics*, *9*(2), 550–589.

Pappalardo, C. M., & Guida, D. (2018). System identification algorithm for computing the modal parameters of linear mechanical systems. *Machines*, *6*(2), 12.

Pappalardo, C. M., Lettieri, A., & Guida, D. (2021). Identification of a dynamical model of the latching mechanism of an aircraft hatch door using the numerical algorithms for subspace state-space system identification. *IAENG International Journal of Applied Mathematics*, *51*(2), 1–14.

Pereira, E., Trapero, J. R., Díaz, I. M., & Feliu, V. (2012). Adaptive input shaping for single-link flexible manipulators using an algebraic identification. *Control Engineering Practice*, *20*(2), 138–147.

Qidwai, U., & Bettayeb, M. (2003). Deconvolution of ultrasonic ndt signals using n4sid algorithm for defect identification. In *10th IEEE International Conference on Electronics, Circuits and Systems, 2003. ICECS 2003. Proceedings of the 2003*, vol. 1, *IEEE*, 60–63.

Qin, S. J. (2006). An overview of subspace identification. *Computers & Chemical Engineering*, *30*(10-12), 1502–1513.

Rew, K.-H., Ha, C.-W., & Kim, K.-S. (2009). A practically efficient method for motion control based on asymmetric velocity profile. *International Journal of Machine Tools and Manufacture*, *49*(7-8), 678–682.

Saad, M. S., Jamaluddin, H., & Darus, I. Z. M. (2015). Active vibration control of a flexible beam using system identification and controller tuning by evolutionary algorithm. *Journal of Vibration and Control*, *21*(10), 2027–2042.

Shan, J., Liu, H.-T., & Sun, D. (2005). Modified input shaping for a rotating single-link flexible manipulator. *Journal of Sound and Vibration*, *285*(1-2), 187–207.

Sivanandam, S. N., & N., D. S. (2007). *Introduction to Genetic Algorithms*. Springer Berlin, Heidelberg.

Skolnik, D., Lei, Y., Yu, E., & Wallace, J. W. (2006). Identification, model updating, and response prediction of an instrumented 15-story steel-frame building. *Earthquake Spectra*, *22*(3), 781–802.

Song, C., Yu, C., Xiao, Y., & Zhang, J. (2017). Fuzzy logic control based on genetic algorithm for a multi-source excitations floating raft active vibration isolation system. *Advances in Mechanical Engineering*, *9*(6), 1687814017705843.

Subramanian, S., Chidhambaram, G. B., & Dhandapani, S. (2021). Modeling and validation of a four-tank system for level control process using black box and white box model approaches. *IEEJ Transactions on Electrical and Electronic Engineering*, *16*(2), 282–294.

Takahashi, Y., Yashige, M., Nakamura, M., & Hirata, E. (2002). Human interface and vibration control of robotic manipulator suspended from ceiling. *Transactions of the Institute of Measurement and Control*, *24*(5), 387–401.

Tho, H. D., Kaneshige, A., & Terashima, K. (2020). Minimum-time s-curve commands for vibration-free transportation of an overhead crane with actuator limits. *Control Engineering Practice*, *98*, 104390.

Tiano, A., Sutton, R., Lozowicki, A., & Naeem, W. (2007). Observer kalman filter identification of an autonomous underwater vehicle. *Control Engineering Practice*, *15*(6), 727–739.

Tronci, E., Pietrosanti, D., Cordisco, G., & De Angelis, M. (2017). Vibration analysis of the civic tower in rieti. *Procedia Engineering*, *199*, 2268–2273.

Tuhta, S., & Günday, F. (2019). System identification of rc building using n4sid. *International Journal of Research and Scientific Innovation*, *6*(11), 100–106.

Tuhta, S., Günday, F., Aydin, H., & Alalou, M. (2019). Mimo system identification of machine foundation using n4sid. *International Journal of Interdisciplinary Innovative Research Development*, *4*(1), 27–36.

Tweten, D. J., Ballard, Z., & Mann, B. P. (2014). Minimizing error in the logarithmic decrement method through uncertainty propagation. *Journal of Sound and Vibration*, *333*(13), 2804–2811.

Uyar, M., & Malgaca, L. (2023). Implementation of active and passive vibration control of flexible smart composite manipulators with genetic algorithm. *Arabian Journal for Science and Engineering*, *48*(3), 3843–3862.

Valasek, J., & Chen, W. (2003). Observer/kalman filter identification for online system identification of aircraft. *Journal of Guidance, Control, and Dynamics*, *26*(2), 347–353.

Van Overschee, P., & De Moor, B. (2012). *Subspace identification for linear systems: Theory—Implementation—Applications*. Springer Science & Business Media.

Wang, J.-S., & Hsu, Y.-L. (2008). Dynamic nonlinear system identification using a wiener-type recurrent network with okid algorithm. *Journal of Information Science & Engineering*, *24*(3), 891–905.

Yang, J. N., Lin, S., Huang, H., & Zhou, L. (2006). An adaptive extended kalman filter for structural damage identification. *Structural Control and Health Monitoring: The Official Journal of the International Association for Structural Control and Monitoring and of the European Association for the Control of Structures*, *13*(4), 849–867.

Yavuz, Ş. (2019). An enhanced method to control the residual vibrations of a single-link flexible glass fabric reinforced epoxy-glass composite manipulator. *Composites Part B: Engineering*, *159*, 405–417.

Yavuz, Ş. (2021). An improved vibration control method of a flexible non-uniform shaped manipulator. *Simulation Modelling Practice and Theory*, *111*, 102348.

Yavuz, Ş., Malgaca, L., & Karagülle, H. (2016a). Analysis of active vibration control of multi-degree-of-freedom flexible systems by newmark method. *Simulation Modelling Practice and Theory*, *69*, 136–148.

Yavuz, Ş., Malgaca, L., & Karagülle, H. (2016b). Vibration control of a single-link flexible composite manipulator. *Composite Structures*, *140*, 684–691.

Zardian, M. G., Darus, I. Z. M., & Miveh, M. R. (2015). System identification and intelligent control of flexible manipulator system. *Journal of Soft Computing and Decision Support Systems*, *3*(1), 44–52.

Ziaei, K., & Wang, D. W. (2006). Application of orthonormal basis functions for identification of flexible-link manipulators. *Control Engineering Practice*, *14*(2), 99–106.

APPENDICES

Appendix A List of Publications

⋆ Pappalardo C. M., Lök, Ş. İ., Malgaca, L., & Guida, D. (2023). Experimental Modal Analysis of a Single-Link Flexible Robotic Manipulator with Curved Geometry using Applied System Identification Methods. *Mechanical Systems and Signal Processing* (SCI-Expendad).

⋆ Lök, Ş. İ., Malgaca, L., & Uyar, M. (2023). Analysis of an Actively Controlled Composite Box Manipulator without External Actuator. *Proceedings of the Institution of Mechanical Engineers Part I-Journal of Systems and Control Engineering* (SCI-Expendad).

⋆[1] Malgaca, L., & Lök, Ş. İ. (2022). Measurement and modeling of a flexible manipulator for vibration control using five-segment S-curve motion. *Transactions of the Institute of Measurement and Control*, 44(8), 1545-1556 (SCI-Expendad).

⋆ Malgaca, L., Lök, Ş. İ., & Uyar, M. (2020). Modeling and vibration reduction of a flexible planar manipulator with experimental system identification. *International Journal of Modeling and Optimization*, 10(4), 121-125 (Peer-Reviewed Journal).

⋆ Malgaca L., Lök Ş. İ., & Uyar M. (2019). Suppression of Pitch Angle Vibrations of a 5-DOF Half Vehicle Model by System Identification Method. *International Journal of Natural and Engineering Sciences*, 13 (2), 49-52 (Peer-Reviewed Journal).

⋆ Malgaca, L. Uyar, M. Lök, Ş. İ. & Vatan Can, S. (2021). Experimental active vibration control of a highly flexible composite manipulator with acceleration feedback. *In 16th Acoustics and Vibration of Mechanical Structures (AVMS)*, 225–233.

⋆ Malgaca, L., Lök, Ş. İ. & Uyar, M. (2020). Modeling of a flexible planar manipulator with system identification method. *In 8th International Conference on System Modeling and Optimization*.

⋆ Malgaca, L., Güneş, E. G. & Lök, Ş. İ. (2019). Experimental vibration analysis of a flexible l frame carrying a payload with system identification method. *In 5th International Conference on Natural and Engineering Sciences*.

⋆ Malgaca, L., Uyar, M. & Lök, Ş. İ. (2019). Modelling and vibration control of a flexible cantilever beam. *In 5th International Conference on Natural and Engineering Sciences*.

⋆ Malgaca, L., Lök, Ş. İ. & Uyar, M. (2018). Active control of pitch angle of a 5 dof half vehicle with a driver. *In 4th International Conference on Natural and Engineering Sciences*.

⋆ Malgaca, L., Uyar, M. & Lök, Ş. İ. (2018). Applying pid tuning algorithms to a half vehicle model. *In 4th International Conference on Natural and Engineering Sciences*.

⋆ Malgaca, L., Uyar, M. & Lök, Ş. İ. (2018). Vibration control of a 2-dof quarter car with an actuator by state space and system identification methods. *In 2nd International Students Science Congress*.

⋆[2] Malgaca, L. & Lök, Ş. İ. (2017). L-çerçevenin sistem tanımlama yöntemi ile titreşim analizi. *In 18. Ulusal Makina Teorisi Sempozyumu (UMTS)*.

⋆[1] and ⋆[2] provide the publication condition of the Ph.D. thesis.

Appendix B LabVIEW Codes for Experimental System

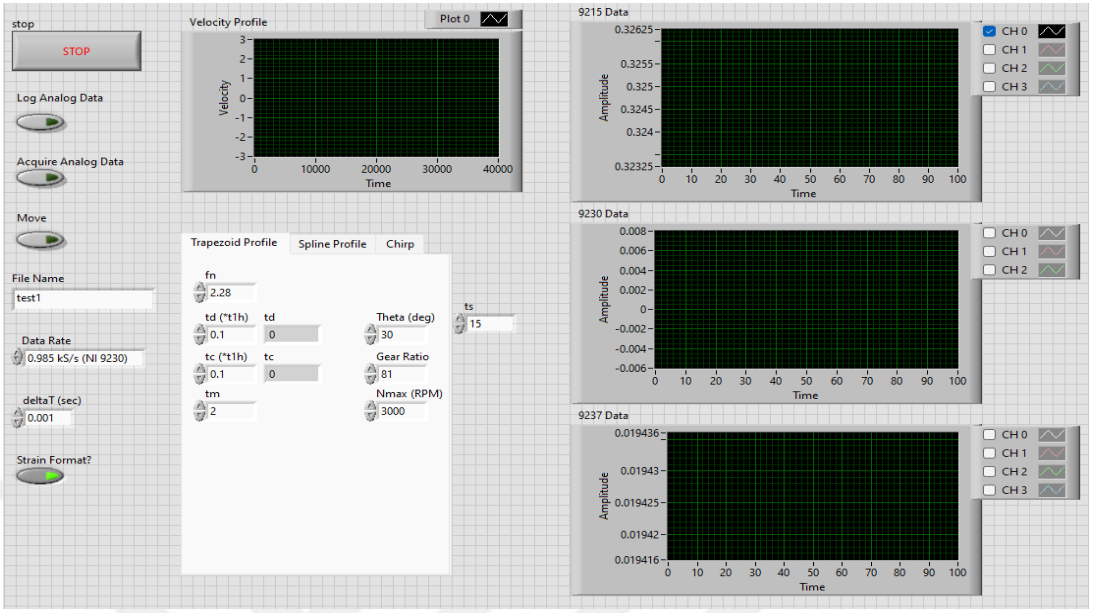


Figure B.1 Front panel for Trapezoidal motion input

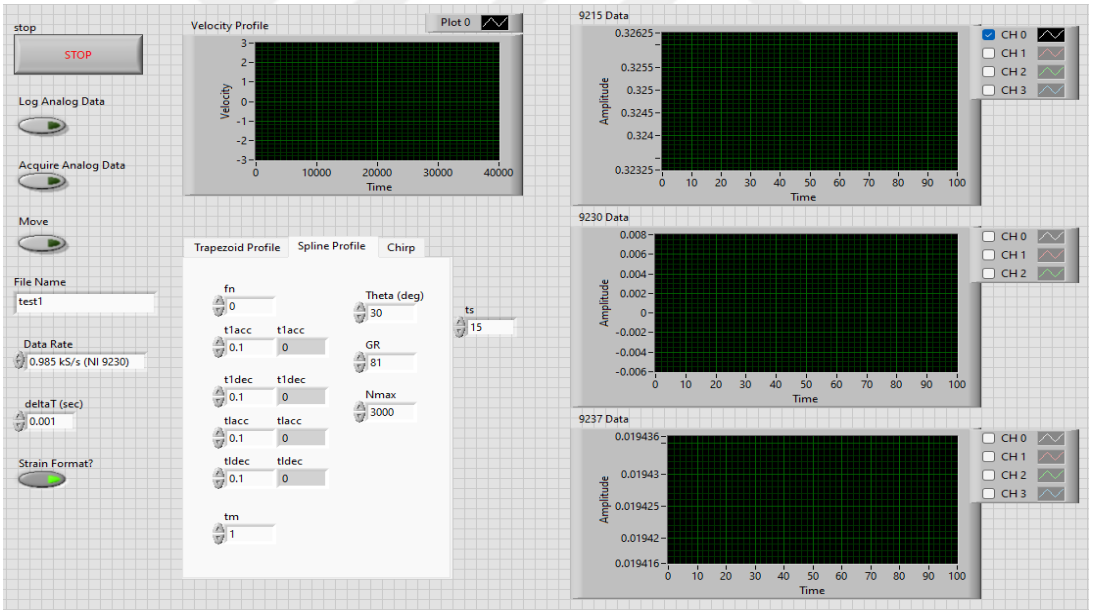


Figure B.2 Front panel for S-curve motion input

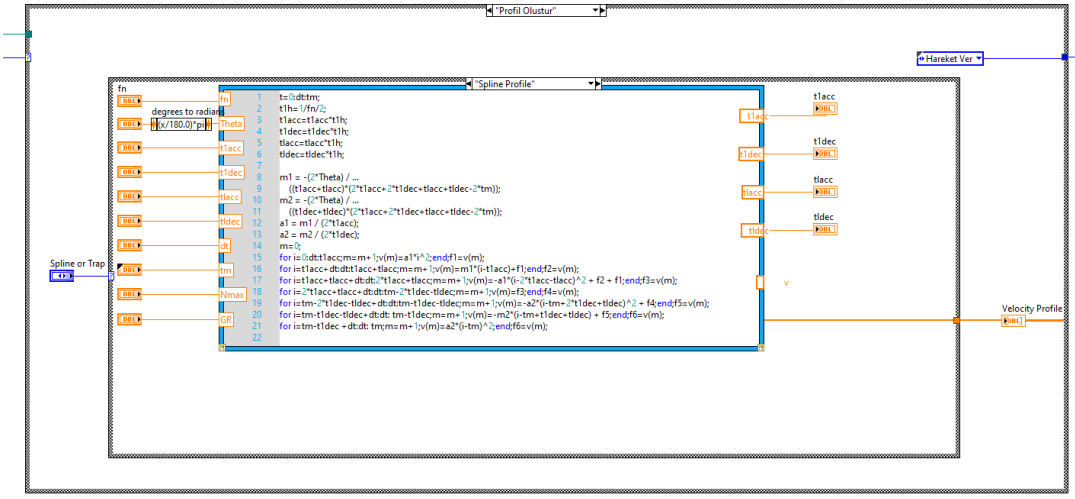


Figure B.3 Generating Trapezoidal motion input

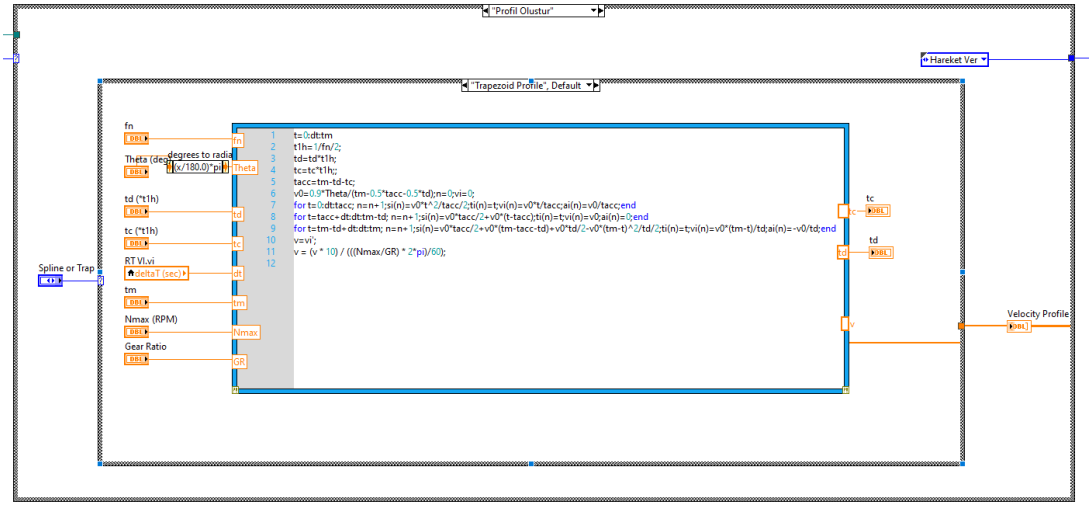


Figure B.4 Generating S-curve motion input

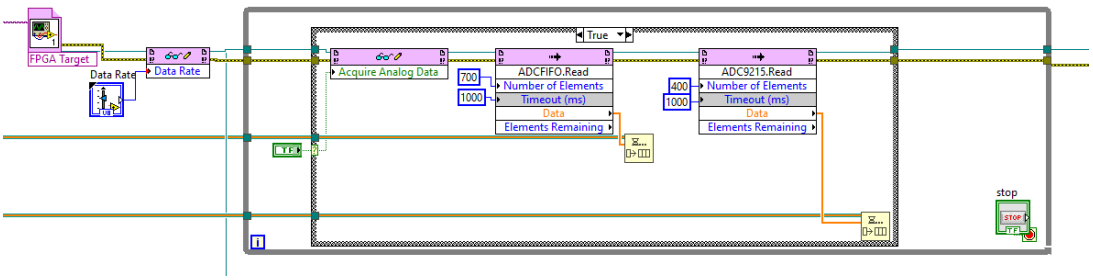


Figure B.5 Servo driving part of block diagram

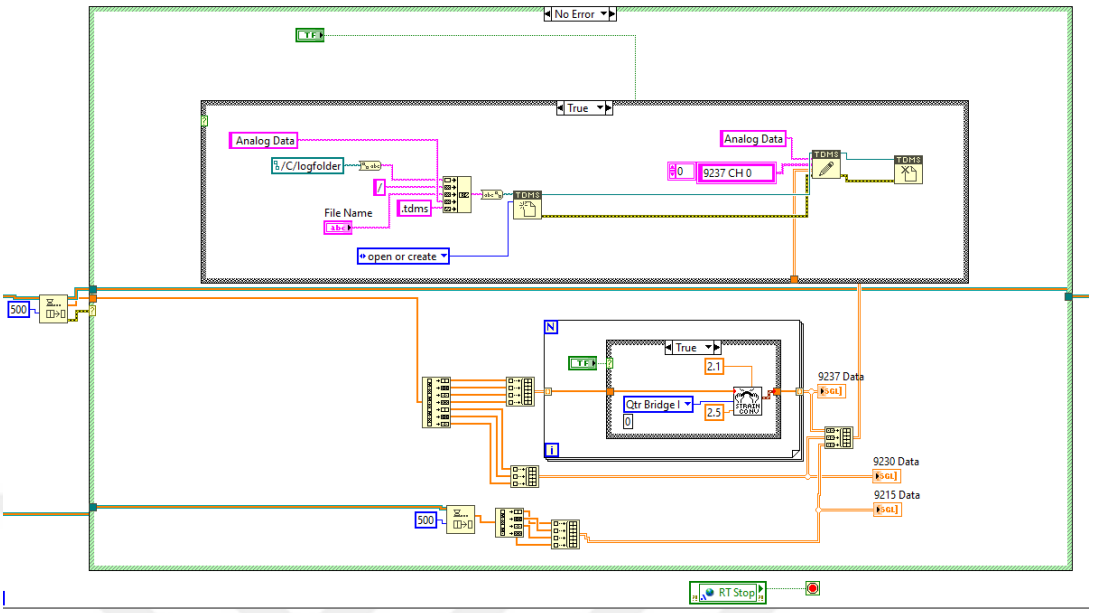


Figure B.6 Data saving of block diagram in LABVIEW code

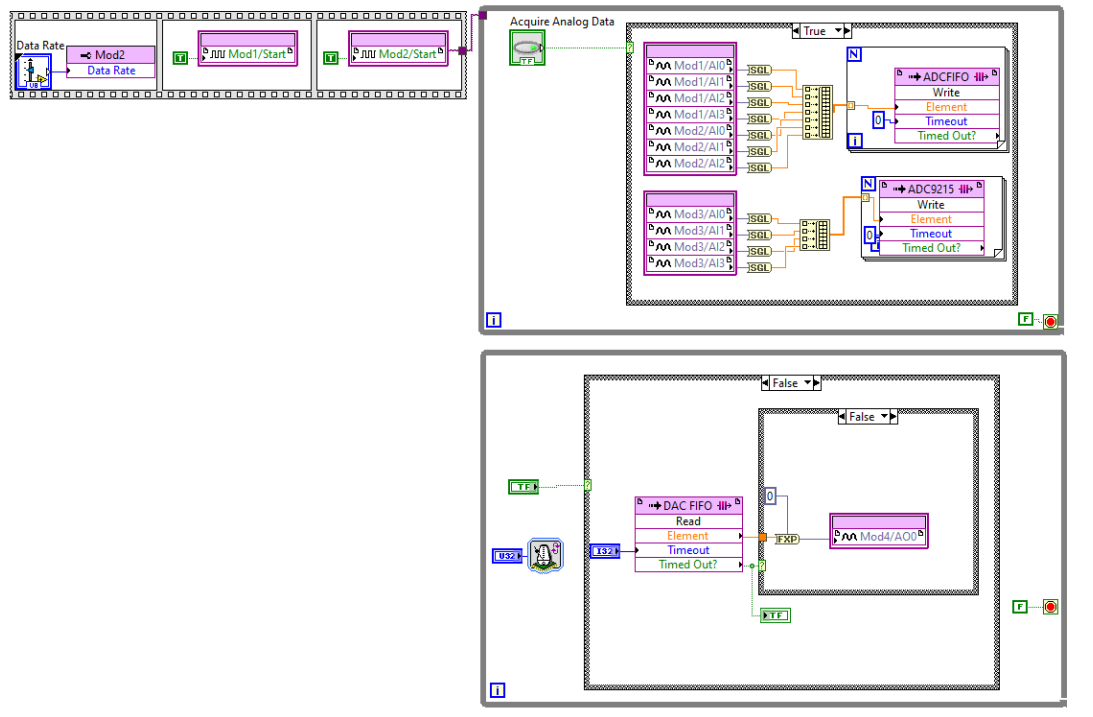


Figure B.7 FPGA block diagram

Appendix C Numerical Results of all the System Identification Methods

In this appendix, the complete set of continuous-time state-space matrices identified in the numerical analysis carried out by using the ARX, CTSI, SSEST, and N4SID identification methods is reported. Some values of the matrices are not given for the confidentiality of the thesis.

Appendix C.1 ARX Method Numerical Results

$$\mathbf{A} = \begin{bmatrix} 11.2283 & 45.6197 \\ \dots & \dots \end{bmatrix}, \quad \mathbf{B} = \begin{bmatrix} -1.4535 \\ 1.4270 \end{bmatrix} \tag{7.1}$$

$$\mathbf{C} = \begin{bmatrix} \dots & 2.6629 \end{bmatrix}, \quad \mathbf{D} = -0.01495 \tag{7.2}$$

Appendix C.2 CTSI Method Numerical Results

$$\mathbf{A} = \begin{bmatrix} -0.1635 & -1630.0352 \\ \dots & \dots \end{bmatrix}, \quad \mathbf{B} = \begin{bmatrix} 1 \\ 0 \end{bmatrix} \tag{7.3}$$

$$\mathbf{C} = \begin{bmatrix} \dots & 22.5139 \end{bmatrix}, \quad \mathbf{D} = -0.0138 \tag{7.4}$$

Appendix C.3 SSEST Method Numerical Results

$$\mathbf{A} = \begin{bmatrix} 12.3479 & -1206.0907 \\ \cdots & \cdots \end{bmatrix}, \quad \mathbf{B} = \begin{bmatrix} 5.8956 \\ 0.0491 \end{bmatrix} \tag{7.5}$$

$$\mathbf{C} = \begin{bmatrix} \cdots & -0.7002 \end{bmatrix}, \quad \mathbf{D} = 0 \tag{7.6}$$

Appendix C.4 N4SID Method Numerical Results

$$\mathbf{A} = \begin{bmatrix} 1.0567 & -0.0520 \\ \cdots & \cdots \end{bmatrix}, \quad \mathbf{B} = \begin{bmatrix} 0.0206 \\ -1.4448 \end{bmatrix} \tag{7.7}$$

$$\mathbf{C} = \begin{bmatrix} \cdots & -0.0284 \end{bmatrix}, \quad \mathbf{D} = -0.0081 \tag{7.8}$$

Appendix D Experimental Results of all the System Identification Methods

In this appendix, the complete set of continuous-time state-space matrices identified in the experimental analysis carried out by using the ARX, CTSI, SSEST, and N4SID identification methods is reported. Some values of the matrices are not given for the confidentiality of the thesis.

Appendix D.1 ARX Method Experimental Results

$$\mathbf{A} = \begin{bmatrix} 10.7129 & 47.9335 \\ \dots & \dots \end{bmatrix}, \quad \mathbf{B} = \begin{bmatrix} -3.1189 \\ 2.6095 \end{bmatrix} \tag{7.9}$$

$$\mathbf{C} = \begin{bmatrix} \dots & 1.5390 \end{bmatrix}, \quad \mathbf{D} = -0.0203 \tag{7.10}$$

Appendix D.2 CTSI Method Experimental Results

$$\mathbf{A} = \begin{bmatrix} -0.1701 & -1630.9629 \\ \dots & \dots \end{bmatrix}, \quad \mathbf{B} = \begin{bmatrix} 1 \\ 0 \end{bmatrix} \tag{7.11}$$

$$\mathbf{C} = \begin{bmatrix} \dots & 33.4098 \end{bmatrix}, \quad \mathbf{D} = -0.0195 \tag{7.12}$$

Appendix D.3 SSEST Method Experimental Results

$$\mathbf{A} = \begin{bmatrix} 13.7708 & -1206.0487 \\ \cdots & \cdots \end{bmatrix}, \quad \mathbf{B} = \begin{bmatrix} 6.4151 \\ 0.0587 \end{bmatrix} \tag{7.13}$$

$$\mathbf{C} = \begin{bmatrix} \cdots & -0.6948 \end{bmatrix}, \quad \mathbf{D} = 0 \tag{7.14}$$

Appendix D.4 N4SID Method Experimental Results

$$\mathbf{A} = \begin{bmatrix} -0.5631 & -0.4799 \\ \cdots & \cdots \end{bmatrix}, \quad \mathbf{B} = \begin{bmatrix} -0.0206 \\ 0.225 \end{bmatrix} \tag{7.15}$$

$$\mathbf{C} = \begin{bmatrix} \cdots & 0.1879 \end{bmatrix}, \quad \mathbf{D} = -0.0131 \tag{7.16}$$